

The SINFONI survey of powerful radio galaxies at $z \sim 2$: Jet-driven AGN feedback during the Quasar Era ^{*}

N. P. H. Nesvadba^{1,2}, C. De Breuck³, M. D. Lehnert⁴, P. N. Best⁵, and C. Collet¹

¹ Institut d'Astrophysique Spatiale, Centre Universitaire d'Orsay, Bat. 121, 91405 Orsay, France

² email: nicole.nesvadba@ias.u-psud.fr

³ European Southern Observatory, Karl-Schwarzschild Strasse, Garching bei München, Germany

⁴ Institut d'Astrophysique de Paris, CNRS & Université Pierre et Marie Curie, 98bis, bd Arago, 75014 Paris, France

⁵ SUPA, Institute for Astronomy, Royal Observatory of Edinburgh, Blackford Hill, Edinburgh EH9 3HJ, UK

Received / Accepted

ABSTRACT

We present VLT/SINFONI imaging spectroscopy of the rest-frame optical emission lines of warm ionized gas in 33 powerful radio galaxies at redshifts $z \gtrsim 2$, which are excellent sites to study the interplay of rapidly accreting active galactic nuclei and the interstellar medium of the host galaxy in the very late formation stages of massive galaxies. Our targets span two orders of magnitude in radio size (2–400 kpc) and kinetic jet energy (a few 10^{46} – almost 10^{48} erg s⁻¹). All sources have complex gas kinematics with broad line widths up to ~ 1300 km s⁻¹. About half have bipolar velocity fields with offsets up to 1500 km s⁻¹ and are consistent with global back-to-back outflows. The others have complex velocity distributions, often with multiple abrupt velocity jumps far from the nucleus of the galaxy, and are not associated with a major merger in any obvious way. We present several empirical constraints that show why gas kinematics and radio jets seem to be physically related in all galaxies of the sample. The kinetic energy in the gas from large scale bulk and local outflow or turbulent motion corresponds to a few 10^{-3} to 10^{-2} of the kinetic energy output of the radio jet. In galaxies with radio jet power $\gtrsim 10^{47}$ erg s⁻¹, the kinetic energy in global back-to-back outflows dominates the total energy budget of the gas, suggesting that bulk motion of outflowing gas encompasses the global interstellar medium. This might be facilitated by the strong gas turbulence, as suggested by recent analytical work. We compare our findings with recent hydrodynamic simulations, and discuss the potential consequences for the subsequent evolution of massive galaxies at high redshift. Compared with recent models of metal enrichment in high- z AGN hosts, we find that the gas-phase metallicities in our galaxies are lower than in most low- z AGN, but nonetheless solar or even super-solar, suggesting that the ISM we see in these galaxies is very similar to the gas from which massive low-redshift galaxies formed most of their gas. This further highlights that we are seeing these galaxies near the end of their active formation phase.

Key words. galaxies: high-redshift, galaxies radio galaxies

1. Introduction

Substantial observational and theoretical progress in the last decade has left little doubt that the supermassive black holes that seem to be nearly ubiquitous in the nuclei of galaxies play a significant role in shaping the properties of their host galaxies. Silk & Rees (1998) recognized that the energy output of active galactic nuclei, in spite of their short lifetimes of only a few 10^7 yrs, is sufficient to unbind most of the interstellar gas even in very massive, gas-rich host galaxies, if this energy can be efficiently injected into the interstellar medium. The details of this mechanism are still relatively poorly understood. Observations have provided evidence that outflows can be seen in galaxies with bolometrically luminous AGN as well as AGN that are dominated by the radio jets produced by narrow beams of relativistic, synchrotron emitting particles.

Of particular interest is the role of powerful AGN in the early evolution of massive galaxies at high redshift. Observational properties of massive low-redshift galaxies as well as cosmological simulations suggest that star formation in high- z galaxies was prematurely truncated before star formation could exhaust

the available gas supply. Immense winds driven by the energy released from AGN are now the truncation mechanism which is preferred by most cosmological models of galaxy evolution. Detailed models of how radio jets drive such winds have made impressive progress in the last years. For example, they predict that prior to forming well collimated jets upon breakout from the ISM, the jet will very effectively deposit its momentum and energy during a “flood and channel” phase, as it permeates the ISM along low-density channels, in agreement with observations (Sutherland & Bicknell 2007; Wagner & Bicknell 2011; Wagner et al. 2012).

Powerful radio galaxies (HzRGs) at high redshift ($z \gtrsim 2$) are ideal sites to study the late formation stages of massive galaxies in the early Universe. They have high stellar (e.g., De Breuck et al. 2003; Seymour et al. 2007; De Breuck et al. 2010) and dynamical masses (Villar-Martín et al. 2003; Nesvadba et al. 2007), and high star formation rates of up to $1000 M_{\odot} \text{ yr}^{-1}$ (Archibald et al. 2001; Reuland et al. 2004; Drouart et al. 2014), with implied formation times of few 100 Myr. They host luminous, obscured quasars with bolometric luminosities of few $\times 10^{45-46}$ erg s⁻¹ (e.g., Carilli et al. 2002; Overzier et al. 2005; Drouart et al. 2014), and have powerful radio jets (e.g., Carilli et al. 1997; Pentericci et al. 2000), indicating that they are the host galaxies of some of the most powerful active galactic nuclei. Their black

^{*} Based on observations collected at the Very Large Telescope of ESO. Program IDs 070.A-0545, 070.A-0229, 076.A-0684, 079.A-0617, 081.A-0468, 381.A-0541, 082.A-0825, 083.A-0445.

hole masses fall near the upper end of the mass function of supermassive black holes in nearby galaxies (Nesvadba et al. 2011b), and scale with the mass of their host galaxies in a fairly similar way as nearby galaxies which fall onto the local black-hole bulge mass relationship, suggesting they must be near the end of their active formation period. Drouart et al. (2014) argued that the black holes of HzRGs will outgrow the plausible mass range for supermassive black holes even in very massive galaxies, if their growth continues for more than a few 10^7 yrs, further highlighting that we are observing these sources at an outstanding moment of their evolution. The same is suggested by their high stellar masses, which exceed the amounts of remaining molecular gas by factors of 10 or more (Emonts et al. 2014), limiting their potential future growth in stellar mass.

HzRGs are often surrounded by extended nebulosities of warm ionized gas (e.g., Villar-Martín et al. 2003; Nesvadba et al. 2008a) with sizes of up to about 60 kpc, and irregular gas kinematics, with velocity offsets and line FWHMs of up to 1000 km s^{-1} , respectively. These velocities are above the escape velocity from the gravitational potential of massive galaxies, suggesting this gas is outflowing (Villar-Martín et al. 2003; Nesvadba et al. 2006b, 2008a). These structures are in most cases elongated along an axis that is approximately aligned with the axis of the radio jet, and have sizes that are smaller than the jet size, and dynamical times comparable to the radio-jet lifetime. This has previously been considered evidence that these are outflows of warm ionized gas that has been entrained by the expanding cocoon of hot, shocked gas inflated by the radio jet (Nesvadba et al. 2006b, 2008a).

Here we present an analysis of 33 powerful radio galaxies at redshifts $z \geq 2$ with new SINFONI observations, revisiting the kinematic and energetic signatures of AGN feedback as previously described for individual sources by Nesvadba et al. (2006b, 2007, 2008a) and for a small sample of lower-power radio galaxies by Collet et al. (2015b). We confirm the basic previous results, and significantly expand them, in particular by studying the trends between radio power and various gas properties. We find a good overall qualitative agreement with hydrodynamic jet models, but significant differences when compared with more detailed predictions.

The paper is organized as follows: In §2 we describe our sample and observations before outlining our analysis methods in §3. These include in particular how we constructed the kinematic maps and subtracted the broad-line emission from the nucleus in the subset of sources which show signatures of direct AGN light. In §4 we discuss the integrated spectral properties of our sample (the detailed properties of individual sources are listed in the appendix A), like emission-line diagnostics, electron densities, gas masses and extinction, before describing the results from spatially resolved maps in §5. This includes continuum maps, $[\text{OIII}]\lambda 5007$ morphologies, maps of $\text{H}\alpha/[\text{OIII}]$ line ratios, and basic morphological properties of the emission-line regions. In §6 we discuss the maps of relative velocities and line widths, the radial dependence of the gas kinematics and surface brightness, and search for signatures of rotationally or pressure-supported gravitational motion. In §5 and 6 we study the relationship between the gas and radio jet properties, like position angles, sizes, axis ratios, and the gas kinematics. We also discuss the implications of these relationships in the context of AGN feedback, study the energetics of the jets and gas flows, the efficiency of the energy transfer from the jet to the gas, and compare with predictions from hydrodynamic models. In §7 we interpret our results in the context of feedback, and turn to the implica-

tions for galaxy evolution in §8, before summarizing our results in §9.

Throughout the paper we adopt a flat $H_0 = 70 \text{ km s}^{-1} \text{ Mpc}^{-1}$ concordance cosmology with $\Omega_M = 0.3$ and $\Omega_\Lambda = 0.7$.

2. Observations and sample selection

2.1. Sample selection

In total, we observed 49 radio galaxies at $z \geq 2$ in a suite of observing programs with SINFONI between 2009 and 2012. This corresponds to 32% of the known radio galaxies at $z \gtrsim 2$ in the compilation of Miley & De Breuck (2008). The redshift distribution of our sample is shown in Fig. 1. All sources are between redshifts $z = 1.4 - 4.8$, and most between $z = 2.0$ and 3.6 . We note a small redshift gap between $z \sim 2.6$ and $z \sim 3.0$, where no bright line emission falls into the near-infrared atmospheric windows. Sixteen of these sources have already been discussed in our previous publications (Nesvadba et al. 2006b, 2007, 2008a; Collet et al. 2015a,b).

Since these targets were selected in a similar way and observed with very similar setups, they form a homogeneous sample with the 33 new targets presented here. For six targets where nuclear broad-line emission was observed in $\text{H}\alpha$, Nesvadba et al. (2011b) presented an analysis of their black-hole properties, but not their extended line emission. They are therefore included in our present study.

The targets are taken from a number of different catalogs, including the Molonglo Reference Catalog (Large et al. 1981), the 3rd, 4th, and 5th Cambridge Catalogs (Laing et al. 1983; Pilkington & Scott 1965; Pearson 1975), the Parkes (Wright & Otrupcek 1990), Parkes-MIT-NRAO (PMN Griffith & Wright 1993) and Texas (TXS, Douglas et al. 1996) surveys, the catalog of Ultra-Steep-Spectrum radio sources (USS; De Breuck et al. 2000), and the Sydney University Molonglo Sky Survey (SUMSS Mauch et al. 2003). Our sample is therefore not complete in a statistical sense, however, given the rarity of powerful high-redshift radio galaxies, it would not be practical to collect a significant number of sources from a statistically complete sample. Moreover, we wish to study trends in gas properties as a function of the radio size and radio power, so that a uniform sampling of radio properties is more important than matching the radio luminosity function. For a population study this would of course be different. In a general sense, these galaxies were selected for their steep spectral indices from low-frequency radio surveys. All had known spectroscopic redshifts, typically from rest-frame UV observations (most redshifts were taken from De Breuck et al. 2000), which implies that our sample is biased towards galaxies with bright UV or optical line emission. With the exception of TXS 2355–003 (already discussed in Collet et al. 2015a), we confirmed the previous redshifts of all galaxies. TXS 2355–003 lies at $z = 1.49$, not at $z = 2.49$, as previously estimated by De Breuck et al. (2000).

Our choice of targets was guided by our aim to investigate how the radio properties of the AGN in our sample affect the warm ionized gas in their host galaxies. This makes it necessary to sample a range in radio properties as uniformly as possible rather than to match the radio luminosity function, as would be the case for a population study. In Fig. 1 we compare the distribution of radio power of our galaxies with the radio luminosity function of Willott et al. (2001) of very powerful high- z radio sources. Our sample is very naturally biased towards galaxies with bright emission lines, corresponding to the “high-excitation line” mode of radio galaxies, or the “Quasar mode” of AGN

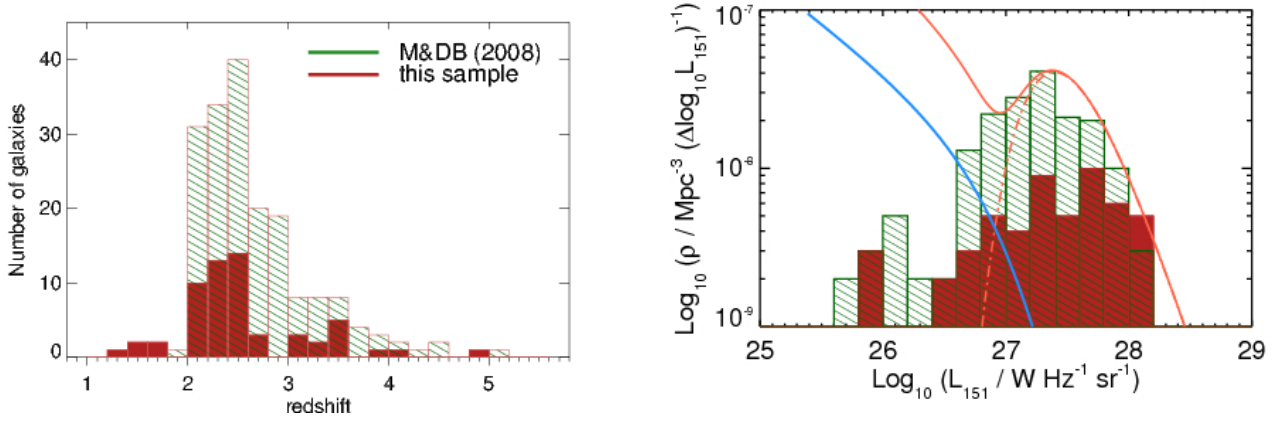


Fig. 1. Distribution of our targets in redshift (*left*) and radio power (*right*). In both panels, the red solid and dark green hatched histograms show our sample and the parent sample of all known powerful radio galaxies at $z \geq 2$ from Miley & De Breuck (2008), respectively. The gap between $z=2.6$ and $z=2.9$ in the left panel is because no bright optical emission lines fall into the near-infrared atmospheric windows at these redshifts. The light blue and light red lines in the right panel show the luminosity function of powerful radio galaxies at redshifts $z=0$ and $z=2$ from Willott et al. (2001), respectively. The dot-dashed light red line highlights their high-power ‘high- z ’ population (for details see Willott et al. 2001).

feedback models, which in turn correspond to the high-power population of Willott et al. (2001). The figure illustrates that we sample a range in radio power from $10^{26.3}$ to $10^{29.3}$ W Hz^{-1} , covering the entire range of about three orders of magnitude that is characteristic for this population, which, according to Willott et al. (2001), fades quickly towards lower redshift. Our faintest radio sources are only factors of a few stronger than implied by the radio flux in the most intense starbursts (Collet et al. 2015b), which is likely dominated by star formation ($\text{few} \times 10^{25}$ W Hz^{-1} , e.g., Barger et al. 2014), whereas our most luminous sources are amongst the most powerful radio sources known in the Universe. For comparison, typical powerful radio galaxies at low redshift have $\text{few} \times 10^{25-26}$ W Hz^{-1} (e.g., Wall & Peacock 1985; Tadhunter et al. 1993).

2.2. VLT/SINFONI observations and data reduction

Observations were carried out with the near-infrared imaging spectrograph SINFONI on UT4 of the Very Large Telescope of ESO between September 2009 and September 2012 under program IDs 079.A-0617, 081.A-0468, 381.A-0541, 082.A-0825, and 083.A-0445. SINFONI is an image slicer which operates in the J, H, and K-band in a contiguous $8'' \times 8''$ field of view at a pixel scale of $125 \text{ mas} \times 250 \text{ mas}$. The spatial resolution of most of our data is set by the size of the seeing disk, between $0.6''$ and $1.5''$. The size of the seeing disk for individual galaxies is shown as a black ellipse in the lower left corner of each line map in Figs. A.4 to A.8. At $z \sim 2$, $1.2''$ corresponds to 10 kpc. This is comparable to a typical galaxy scale, so that our data allow us to infer for all targets whether the gas is confined to within the AGN host galaxy or extends beyond. MRC 2104–242, MG 2037–0011, and NVSS J2135–3337 fortuitously have nearby bright stars that served as natural guide stars for adaptive-optics assisted observations. For those galaxies, we obtained high-resolution observations with a spatial resolution of about $0.4''$ (~ 3 kpc). The spatial resolution for these sources is limited by the pixel size. We used the largest pixel size also for the adaptive-optics data, because we wanted to reach the highest possible sensitivity to the lowest surface-brightness gas in our sources.

On-source observing times were between 30 and 375 minutes. The range in observing times is large because data obtained in service mode (most of the sample) were not always completed. As a consequence of this and varying spectral bands and observing conditions, the depth of our observations ranges between $\text{rms}=0.8$ and 2×10^{-17} $\text{erg s}^{-1} \text{ cm}^{-2} \text{ \AA}^{-1} \text{ arcsec}^{-2}$, for a circular aperture with $1''$ diameter and after smoothing spatially by 3×3 pixels, akin to our data cubes prior to analysis. In spite of this, we detected line emission from all galaxies at least in one band, including those with the shortest exposure times. With very short exposures we may however have missed faint, extended line emission in some cases. Observing parameters and exposure times of individual sources are listed in Table 1. We also point out in our descriptions of individual sources in Appendix A which sources might be affected.

Most data were obtained with the H+K grating which covers the H and K band simultaneously at $R \sim 1500$ (corresponding to $\text{FWHM} \approx 200 \text{ km s}^{-1}$) and is sufficient to resolve all emission lines spectrally in our targets. Some galaxies, in particular those observed during the visitor run 079.A-617, were observed in the H and K-band individually. Where appropriate, for example owing to the redshift of the source, we also observed in the J band. The spectral resolving power in the J, H, and K band is $R \sim 2000$, $R \sim 3000$, and $R \sim 4000$, respectively. Table 1 lists all bands in which each target was observed. The bands covered for each source can also be found in the detailed descriptions of individual sources in Appendix A.

2.3. New and archival VLA observations

We also collected a set of new VLA continuum imaging for parts of our sample through program AN 0129, to increase the number of targets with arcsecond resolution radio morphologies. C. Carilli kindly shared his radio imaging of 17 sources with us, which had previously been discussed by Carilli et al. (1997) and Pentericci et al. (2000), and we obtained the cm imaging of another eight sources from the VLA archive. Tab. 2 lists the sets of the new and archival radio images used for this study.

Observations of our proprietary program AN 0129 were carried out in one observing session with 25 antennae on 2007 July

Source	RA(J2000)	Dec (J2000)	redshift	DL [Gpc]	DA [Gpc]	Band	ToT. [s]
MRC 0114–211	01:16:51.4	–20:52:07	1.41	10.1	8.4	HK	4800
BRL 0128–264	01:30:27.9	–26:09:58	2.35	18.9	8.2	HK	7500
MRC 0156–252	01:58:33.6	–24:59:31	2.02	15.7	8.4	HK	13800
USS0211–122	02:14:17.4	–11:58:47	2.34	18.8	8.2	HK	10500
MRC 0251–273	02:53:16.7	–27:09:13	3.16	27.1	7.6	HK	11400
RC J0311+0507	03:11:47.9	+05:08:01	4.80	44.5	6.4	HK	5400
MP J0340–6507	03:40:44.6	–65:07:12	2.29	18.3	8.2	HK	12600
PKS 0529–549	05:30:25.4	–54:54:22	2.58	21.2	8.0	HK	21600
5C 7.269	08:28:38.8	+25:28:27	2.22	17.6	8.3	HK	7200
MRC 1017–220	10:19:49.0	–22:19:58	1.77	13.4	8.5	HK	11100
TN J1112–2948	11:12:23.9	–29:48:07	3.09	26.3	7.6	HK	22500
TXS 1113–178	11:16:14.7	–18:06:23	2.24	17.8	8.2	HK	1800
3C 257	11:23:09.4	+05:30:18	2.46	20.0	8.1	HK	8100
USS 1243+036	12:45:38.4	+03:23:21	3.57	31.3	7.3	HK	12000
MG 1251+1104	12:51:00.0	+11:04:22	2.32	18.6	8.2	HK	2400
MRC 1324–262	13:26:54.7	–26:31:42	2.28	18.2	8.2	HK	2400
TN J1338–1942	13:38:26.0	–19:42:31	4.11	37.0	6.9	J,HK	14100, 10500
USS 1410–001	14:13:15.1	–00:23:00	2.36	19.0	8.2	HK	10500
MRC 1558–003	16:01:17.3	–00:28:48	2.53	20.7	8.1	HK	21300
USS 1707+105	17:01:06.5	+10:31:06	2.35	18.9	8.2	HK	10500
3C 362	17:47:07.0	+18:21:10	2.28	18.2	8.2	HK	7200
MP 1758–6738	17:58:51.3	–67:37:28	2.03	15.8	8.4	HK	7200
TN J2007–1316	20:07:53.2	–13:16:44	3.84	34.1	7.1	HK	9600
MRC 2025–218	20:27:59.5	–21:40:57	2.63	21.7	8.0	HK	18600
MG 2037–0011	20:37:13.4	–00:10:59	1.51	11.0	8.5	J,H	5400, 4050
MRC 2048–272	20:51:03.6	–27:03:03	2.06	16.1	8.3	HK	13200
MRC 2104–242	21:06:58.2	–24:05:11	2.49	20.3	8.1	H,K	8100, 10800
4C 23.56	21:07:14.8	+23:31:45	2.48	20.2	8.1	HK	1500
NVSS J2135–3337	21:35:10.5	–33:37:04	2.52	20.6	8.1	K	18600
MG 2144+1928	21:44:07.5	+19:29:15	3.59	31.5	7.3	HK	16500
MRC 2224–273	22:27:43.2	–27:05:02	1.68	17.0	8.3	HK	2700
TN J2254+1857	22:54:53.7	+18:57:04	2.15	17.0	8.3	H,K	3600, 10800
MG 2308+0336	23:08:25.2	+03:37:03	2.46	20.0	8.1	HK	1800
TXS 2353–003	23:55:35.9	–00:02:48	2.59	21.3	8.0	HK	8700

Table 1. Our sample. Column (1) – Source ID. Column (2) – Right ascension. Column (3) – Declination. Column (4) – Luminosity distance in Gpc. Column (5) – kpc per arcsec.. Column (6) – Observing band. Column (7) – On-source observing time in seconds.

5, during the upgrade to the EVLA, and under rather unstable conditions. This made it unfortunately impossible to measure polarizations robustly in two bands and obtain rotation measures, as we had initially planned. However, the total power measurements were not affected.

New data were obtained with the A-array (BnA for targets at $\text{Dec} < -20^\circ$) at one or both of the frequencies 4.885 GHz and 8.485 GHz, limited by the constraints of observing time. We observed each source several times at different hour angles, covering typically about 4–5 hrs per source. On-source integration times were between 1260 and 1310 s per source in the 8.4 GHz band, and between 5100 and 5480 s per source in the 4.8 GHz band, respectively. The resulting rms is between 17 and 86 μJy in the final maps.

3C 48 was used as a primary calibrator to set the flux scale, and secondary calibrators located within $\approx 10^\circ$ of the target source were observed every 20–30 min for phase calibration. These data were all reduced using standard techniques within AIPS. Sources were self-calibrated first in phase, and then in amplitude and phase, to improve the final image quality. Final images were made using a ROBUST=0 antenna weighting as a compromise between angular resolution and sensitivity.

Already existing, non-proprietary VLA observations of our sources were obtained from the VLA archive and reduced in a similar manner. The archival data of MG 2308+0336 did not have a primary flux calibrator, so we were forced to bootstrap

the flux density from the secondary calibrator. As a result, the uncertainty in radio flux is likely high compared to the other sources, about 50%. Given that our primary use of these data is to constrain the radio morphology and the kinetic power, which introduces astrophysical uncertainties of factors of a few, we do not consider this an important limitation of our analysis.

3. Methodology

3.1. Integrated spectra

We show integrated spectra for each source in Figs. A.1. These spectra were obtained by summing over all spatial pixels where the signal-to-noise ratio of the $[\text{OIII}]\lambda 5007$ line exceeded 3σ . We extracted other line fluxes from the same area. Except for $\text{H}\alpha$ in some cases, $[\text{OIII}]\lambda 5007$ was typically more extended than other emission lines. Before adding the spectrum in a given spatial pixel, we corrected for the velocity shift in this pixel relative to the nucleus. Our integrated line profiles therefore give a luminosity-weighted measure of the intrinsic line widths of the extended emission-line gas, which is not affected by the resolved velocity offsets. This also helps to maximize the signal-to-noise ratios of the fainter lines.

Source	RA(J2000)	Dec(J2000)	freq. [GHz]	rms [μ Jy/bm]	Beam [arcsec,arcsec]	PA [deg.]	Program	Reference
MRC0114–211	01:16:51.40	20:52:06.8	23.3	362	0.1, 0.1	-11	AJ206	
BRL 0128–264	01:30:27.82	-26:09:57.0	4.8	28	1.0, 0.8	-75	AN129	^a
MRC 0156–252	01:59:04.40	-25:28:38.9	8.2	33	0.9, 0.4	-5	AC374	Carilli et al. (1997)
USS 0211–122	02:14:17.40	-11:58:46.0	8.2	28	0.4, 0.3	-5	AC374	Carilli et al. (1997)
MRC 0251–273	02:53:16.74	-27:09:13.0	8.5	13	0.9, 0.3	13.	AD520	
RC 0311+0507	03:09:09.86	04:56:48.3	4.9	287	0.7, 0.6	1.0	AH167	Parijskij et al. (2014)
MRC 0406–244	04:08:51.50	-24:18:16.0	4.9	22	1.1, 0.7	89	AN129	^a
PKS 0529–549	05:30:25.40	-54:54:23.1	18.5	54	1.0, 0.8	43	ATCA	Broderick et al. (2007b)
5C 07.269	08:28:38.97	25:28:27.2	8.4	146	0.2, 0.2	35	AB808	De Breuck
TXS 0828+193	08:30:53.40	19:13:16.0	4.9	21	0.6, 0.4	-69	AN129	^a
3C 257	11:17:69.32	06:03:14.0	8.4	13	0.4, 0.2	43	AV165	
TN J1112–2948	11:12:23.94	-29:48:07.0	4.8	130	4.0, 1.3	-36	ADA000	DeBreuck
TXS 1113–178	11:16:14.68	-18:06:23.6	4.7	57	0.8, 0.4	-2	AC374	Carilli et al. (1997)
USS1243+036	12:45:38.39	03:23:21.0	8.4	25	0.3, 0.2	48	AM336	
MRC 1324–262	13:26:54.66	-26:31:41.4	8.2	32	0.5, 0.3	12	AC374	Carilli et al. (1997)
TN J1338–1942	13:38:26.06	-19:42:30.1	8.2	12	0.4, 0.2	1	AP360	Carilli et al. (1997)
USS 1410–001	14:13:15.15	-00:23:00.8	4.7	43	0.6, 0.5	17	AC374	Carilli et al. (1997)
MRC 1558–003	16:01:17.43	-00:28:46.4	8.5	14	0.3, 0.3	22	AP360	Carilli et al. (1997)
USS 1707+105	17:10:06.85	10:31:09.0	4.8	38	0.5, 0.4	-24	AD520	
MP 1747+182	17:47:07.00	18:21:10.8	4.7	13	0.5, 0.5	13	AP360	Carilli et al. (1997)
TN J2007–1316	20:07:53.26	-13:16:43.6	8.5	37	0.4, 0.2	16	AD520	DeBreuck
MRC 2025–218	20:27:59.49	-21:40:56.9	4.8	56	2.9, 1.2	-30	AN129	^a
MG 2037–0011	20:37:13.40	-00:10:58.0	8.4	22	0.3, 0.2	36	AN129	^a
MRC 2104–242	21:06:58.10	-24:05:11.0	4.8	28	1.6, 0.6	56	AN129	^a
4C 23.56	21:07:14.28	23:31:41.2	8.4	25	0.2, 0.2	-34	AC379	
NVSSJ2135–3337	21:35:10.48	-33:37:04.4	4.8	28	1.3, 1.0	30	AN129	^a
MG 2144+1928	21:44:07.52	19:29:14.8	8.4	66	0.2, 0.2	-8	AS446	
TN J2254+1857	22:54:53.71	18:57:04.6	4.9	17	0.4, 0.4	-73	AN129	^a
MRC 2308+0336	23:03:19.62	03:04:25.1	5.0	36	0.5, 0.4	40	AB375	
TXS 2353–003	23:55:35.90	-00:02:48.0	4.8	19	0.4, 0.4	-21	AN129	^a
TXS 2353–003	23:55:35.90	-00:02:48.0	8.4	17	0.3, 0.3	40	AN129	^a

Table 2. List of new and archival VLA observations complementing this study.^(a) This study.

3.2. Removal of nuclear broad line emission

Six of the galaxies presented here have bright broad H α line emission from the AGN (Nesvadba et al. 2011b), a seventh with lower radio power was found by Collet et al. (2015b). To analyze the extended emission-line regions of these galaxies, it was necessary to remove the nuclear component first. This is not an easy task, because the broad and narrow-line profiles are often not very well approximated by Gaussian line profiles, and therefore, fitting the spectra of a galaxy with multiple Gaussians corresponding to the broad and narrow lines often leads to significant residuals. Several approaches have been proposed in the literature (e.g., Christensen et al. 2006; Cano-Díaz et al. 2012), but all leave large residuals, which is why we developed another method.

Rather than simply approximating the full BLR profile with a Gaussian, we only use a Gaussian fit to interpolate the observed spectrum at the wavelengths covered by the narrow emission lines, and construct a hybrid BLR profile in which the intrinsic line profile along the wings is not changed. We subtract this hybrid BLR line profile from all spatial pixels contaminated by BLR emission, after scaling the flux of the nuclear component by the flux expected from the point spread function as measured from the AGN continuum. Through this scaling, the size of the seeing disk as measured during the observation itself is automatically taken into account. For a more detailed description and the performance of these fits see Collet (2014) and Nesvadba et al. (2017, in prep.).

3.3. Map construction

We constructed emission-line maps of these galaxies in very similar ways to the SINFONI samples previously analyzed by Nesvadba et al. (2006b, 2008a, 2011b), Collet et al. (2015a,b), and Nesvadba et al. (2016, in prep.). Namely, we obtained integrated spectra from box apertures in each galaxy, covering 3×3 pixels ($0.4'' \times 0.4''$). This is less than the size of the seeing disk, and corresponds to the spatial resolution that can be obtained with adaptive-optics assisted observations and a pixel scale of $125 \text{ mas} \times 250 \text{ mas}$ (§2.2). This therefore minimizes pixel-to-pixel noise without introducing artificial beam-smearing effects. For galaxies where [OIII] $\lambda\lambda 4959,5007$ is observed, we fitted the [OIII] $\lambda\lambda 4959,5007$ lines first, which probe the same gas, and have a fixed flux ratio $R_{4959,5007} = 1/3$. For most galaxies we use the [OIII] $\lambda 5007$ maps to measure the morphology and kinematics of the warm ionized gas. In §5.5 we will present our arguments why this gives representative results for the warm ionized gas overall. H α is bright enough to allow for independent fits, but is too broad and heavily blended with [NII] $\lambda\lambda 6548,6583$ in most galaxies to provide good kinematic constraints. Other lines, including H β , are too faint to be well mapped over large radii. Generally speaking, single-component Gaussians were sufficient to obtain good fits. Exceptions are mentioned in the individual target descriptions in Appendix A.

To monitor the goodness-of-fit and evaluate the need for multiple emission-line components, we also constructed maps of the reduced χ^2 , as well as cubes of the fit residuals. Fit residuals are usually below a few percent of the fitted line flux, and median

reduced χ^2 are between 0.7 and 5, depending on the degree of contamination with night-sky lines to the emission lines. A notable exception is USS 0211–122, which we will further discuss below in §A.4.

Our galaxies are too faint in the continuum to study their spectral energy distribution, however, we were able to localize the peak of the continuum emission in 23 targets. We constructed line-free continuum images by averaging along the spectral direction of our data cubes after masking the brightest night-sky lines and the line emission from our targets. Continuum morphologies, where detected, are shown as contours in Figs. A.4 to A.8. Imperfections in the night-sky subtraction and flat fielding, and night-sky line residuals make it unfortunately very difficult to obtain a good sky subtraction from SINFONI cubes, which makes continuum flux measurements very challenging. Typical uncertainties are about 0.3–0.5 mag, so that measurements through broad-band filters are more reliable.

4. Integrated spectral properties of the sample

4.1. Integrated spectra

In Fig. A.1 we show the integrated spectra of our targets. Wavelengths between 1.8 μm and 2.0 μm , i.e., between the H and K bands, and where the atmospheric transmission is very low, are clipped. For galaxies at redshifts $z \sim 2.0 - 2.6$, the $[\text{OIII}]\lambda\lambda 4959, 5007$ doublet and $\text{H}\beta$ fall into the H, and $[\text{OI}]\lambda 6300$, $\text{H}\alpha$, $[\text{NII}]\lambda\lambda 6548, 6583$, and $[\text{SII}]\lambda\lambda 6716, 6731$ fall into the K-band. For galaxies at $z \sim 3.0 - 3.8$, $[\text{OII}]\lambda 3727$ falls into the H-band and $\text{H}\beta$ and $[\text{OIII}]\lambda\lambda 4959, 5007$ fall into the K-band. $[\text{OI}]\lambda 6300$ has been detected in six sources. The $[\text{SII}]\lambda\lambda 6716, 6731$ doublet has been detected in 13 sources, and the doublets have been spectrally resolved into individual components in two galaxies. In eleven sources, the two lines of the doublet are blended due to large intrinsic widths and the relatively low spectral resolving power of $R=1500$. $\text{H}\alpha$ and $[\text{NII}]\lambda\lambda 6548, 6583$ are also blended in most sources. Nonetheless, visual inspection of integrated spectra already shows that the $[\text{NII}]\lambda 6583/\text{H}\alpha$ ratios are generally below unity, and often below 0.5, unlike in AGN host galaxies at low redshift. We will come back to this point in §4.2 and §8.2.

4.2. Diagnostic diagrams and gas-phase metallicities

The bright, rest-frame optical emission lines contain a multitude of constraints on the gas properties, including electron temperatures and densities, ionization parameter, extinction, and gas-phase metal abundance. Taken together, combinations of these lines provide observationally very convenient diagnostics of the gas heating mechanism by young stellar populations or active galactic nuclei (e.g., Veilleux & Osterbrock 1987; Kewley et al. 2001; Kauffmann et al. 2003; Kewley et al. 2006).

Identifying HII regions and AGN narrow-line regions in galaxies by means of their bright optical line ratios is a very successful tool for galaxy evolution studies at low redshift, where the relative uniformness of most HII and AGN narrow-line regions results in fairly narrow sequences in diagnostic diagrams of, e.g., the $[\text{NII}]/\text{H}\alpha$ and $[\text{OIII}]/\text{H}\beta$ line ratios (“BPT-diagrams” Veilleux & Osterbrock 1987; Kewley et al. 2001, 2006).

In Fig. 2 we show where our galaxies fall relative to the $[\text{NII}]/\text{H}\alpha$ vs. $[\text{OIII}]/\text{H}\beta$ diagram. Given that our sources host very luminous obscured quasars (e.g., Overzier et al. 2005; Drouart et al. 2014), it may not be surprising that our galaxies fall outside the sequence of HII regions, and into the part of the

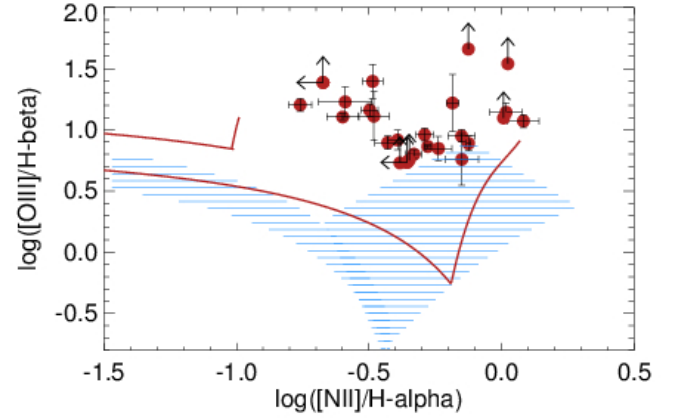


Fig. 2. BPT diagram of our sources with two of the models of Kewley et al. (2013a) shown for $z=2.5$. Red circles show the 25 radio galaxies from the present analysis and those of Collet et al. (2015b), which have measurements of all four lines or sensitive upper limits (on $\text{H}\beta$ or $[\text{NII}]\lambda 6583$). We also mark the range of line ratios expected for low-redshift galaxies with ordinary star formation properties and high-metallicity AGN narrow-line regions (light blue hatched region). The red lines show the ‘high-redshift’ starburst region of Kewley et al. (2013a) and the AGN branch with low-metallicity narrow-line regions (their scenario 4)

diagram that is characteristic of AGN photoionization (see also Villar-Martín et al. 1997; Villar-Martín et al. 2003; Humphrey et al. 2009). However, our galaxies do not fall onto the classical AGN branch from low-redshift studies either, but towards higher $[\text{OIII}]\lambda 5007$ fluxes for a given $\text{H}\beta$ flux and $[\text{NII}]/\text{H}\alpha$ ratio.

Kewley et al. (2013a) and Kewley et al. (2013b) predicted such a shift for gas photoionized by powerful AGN, when imposing a redshift evolution of narrow-line metallicity as modeled by Davé et al. (2010), which scales with the cosmic history of star formation. They distinguish between two models of metal-poor narrow-line regions, either in combination with a low-redshift star-forming branch, or with a star-forming branch shifted towards lower $[\text{NII}]/\text{H}\alpha$ values for a given $[\text{OIII}]/\text{H}\beta$ ratio, as found in many actively star-forming galaxies at $z \sim 2$ (Erb et al. 2006; Lehnert et al. 2009; Förster Schreiber et al. 2009a; Steidel et al. 2014).

The $[\text{NII}]/\text{H}\alpha$ ratios of our galaxies fall into the range predicted by the low-metallicity models of Kewley et al. (2013a), however, the $[\text{OIII}]/\text{H}\beta$ ratios exceed this range by few 0.1 dex. Our data are not sensitive to distinguishing whether the star-forming ISM in our galaxies may be more akin to low-redshift conditions, or the more extreme environs in high- z starburst galaxies. But given the high star formation rates implied by the far-infrared continuum in at least some of our sources (Drouart et al. 2014), and because the offset of the star formation branch in these galaxies appears to be most likely due to a higher ionization parameter in these galaxies, we suspect that the latter will likely be the case. We will discuss this point further in §8.2

4.3. Electron densities

Amongst the bright rest-frame optical lines, the $[\text{OI}]\lambda\lambda 3726, 3729$ and $[\text{SII}]\lambda\lambda 6716, 6731$ doublets are particularly interesting, because they provide constraints on the

electron density of the warm ionized gas for densities between about 100 and 10^5 cm^{-3} (e.g., Osterbrock 1989). Unfortunately, both components of these doublets are very near in wavelength to each other, which makes it challenging to isolate the two lines in most of our targets, given their broad intrinsic widths of typically $\sim 800 \text{ km s}^{-1}$ (Appendix A gives the FWHM for individual targets), moderate spectral resolution of $R=1500$ provided by the H+K grating, presence of night-sky line residuals, and relatively faint line fluxes.

In spite of this, we were able to identify and resolve the $[\text{OII}]\lambda\lambda 3726, 3729$ doublet in RC J0311+0507 (§A.6) with a line ratio of $F(3727)/F(3729)=0.96$, which suggests an electron density of 350 cm^{-3} for the best-fit value of the line ratio of $F(3727)/F(3729)=0.96$ (see also Table A.5 Osterbrock 1989). To our knowledge, this is the first estimate of the electron density in an AGN host galaxy at $z \geq 4$. In USS 0211-122 at $z=2.34$, we find a $[\text{SII}]\lambda\lambda 6716, 6731$ ratio of 1.3, corresponding to an electron density of 370 cm^{-3} (Table A.5). In MRC 0114-211 at $z=1.4$, we find a line ratio of 1.25 between the two $[\text{SII}]$ doublet lines, which corresponds to a best-fit value of $n_e = 310 \text{ cm}^{-3}$. Nesvadba et al. (2006b) and Nesvadba et al. (2008a) previously found electron densities of 390 cm^{-3} and 500 cm^{-3} , in MRC 1138-262 and MRC 0406-242, respectively, and Collet et al. (2015b) found $n_e = 500 \text{ cm}^{-3}$ and 750 cm^{-3} for two radio galaxies with somewhat lower radio power at similar redshifts, NVSS J210626-314003, and NVSS J012932-385433. As a fiducial value for the whole sample, we will adopt $n_e = 500 \text{ cm}^{-3}$ in the present analysis.

4.4. Extinction and ionized gas masses

H^+ is the most abundant species of warm ionized gas and can therefore be used to estimate the total mass of warm ionized gas, if extinction and electron density (§4.3) are known. We have observed both lines, $\text{H}\alpha$ and $\text{H}\beta$, in 15 galaxies, and follow Osterbrock (1989) and Dopita & Sutherland (2003) in estimating the extinction from the observed line ratios and Balmer decrements. We assume a Galactic extinction law and a Balmer decrement of $\text{H}\alpha/\text{H}\beta = 2.88$. We find a large range of (nominally) $A_V = 0.0$ mag to 4.7 mag. Results for individual galaxies are found in Table 6. For $\text{H}\alpha$, this corresponds to correction factors between 1 and 13. We note that we do not correct the $\text{H}\beta$ line for potential underlying stellar absorption. As previously discussed by Nesvadba et al. (2008a), the expected absorption line equivalent widths of few Å are very small compared to the large emission-line equivalent widths of $\text{H}\beta$, which makes such a correction unnecessary.

We can derive a mass of warm ionized gas mass from the $\text{H}\alpha$ line flux by setting

$$M_{\text{WIM}, \text{H}\alpha} = \frac{L_{\text{H}\alpha}}{h \nu_{\text{H}\alpha} \alpha_{\text{eff}}^{\text{H}\alpha}} = 3.3 \times 10^8 L_{\text{H}\alpha, 43} n_{e, 100}^{-1} M_{\odot}, \quad (1)$$

where $L_{\text{H}\alpha}$ is the $\text{H}\alpha$ luminosity, h the Planck constant, $\nu_{\text{H}\alpha}$ the rest-frame frequency of the $\text{H}\alpha$ line, $\alpha_{\text{eff}}^{\text{H}\alpha}$ the effective $\text{H}\alpha$ recombination coefficient, and $n_{e, 100}$ the electron density in units of 100 cm^{-3} .

For the galaxies at $z \sim 3.0-3.6$, where $\text{H}\beta$ falls into the K-band, and $\text{H}\alpha$ outside the atmospheric windows, we can use an analogous estimate for the warm ionized gas mass based on the $\text{H}\beta$ luminosity:

$$M_{\text{WIM}, \text{H}\beta} = \frac{L_{\text{H}\beta}}{h \nu_{\text{H}\beta} \alpha_{\text{eff}}^{\text{H}\beta}} = 9.5 \times 10^8 L_{\text{H}\beta, 43} n_{e, 100}^{-1} M_{\odot}. \quad (2)$$

However, we will treat the warm ionized gas mass estimates from $\text{H}\beta$ as lower limits. The reason is the higher dust attenuation in the rest-frame V compared to the R-band, and the small number of galaxies with good detections of Balmer lines higher than $\text{H}\beta$. We only have a good detection of $\text{H}\gamma$ for PKS 0529-549, for which we also have $\text{H}\alpha$ and $\text{H}\beta$ measured. For redshifts $z \sim 3.1-3.6$, $\text{H}\gamma$ falls inbetween the H and the K band, which makes it unobservable for most of the galaxies where we have only $\text{H}\beta$ measured.

The estimates provided here are a factor 3 lower than those previously given by Nesvadba et al. (2006b, 2008a), due to a missing factor 3 in the previous estimates. Given the high masses of warm ionized gas found in that study, and large systematic uncertainties of factors of a few, this difference has however no impact on the scientific arguments presented previously. We list the new estimates of the warm ionized gas masses in these galaxies in Table 6.

With a fiducial electron density $n_e = 500 \text{ cm}^{-3}$ and the extinctions given in Table 6 we find warm ionized gas masses of $2 \times 10^8 - 5 \times 10^9 M_{\odot}$. These masses are much greater than the masses of warm ionized gas typically found in star-forming galaxies or radio-quiet quasar host galaxies at similar redshifts. For example, using the $\text{H}\alpha$ luminosities measured by Förster Schreiber et al. (2009b) and Lehnert et al. (2009), we find warm ionized gas masses of few times $10^7 M_{\odot}$ or less in typical UV/optical and sub-mm selected high- z star-forming galaxies.

For eight of our HzRGs we can compare the warm ionized and the molecular gas masses directly. Emonts et al. (2014) measured masses between 3.6 and $7 \times 10^{10} M_{\odot}$ of molecular gas from CO(1-0) observations at ATCA in five of our sources, and placed upper limits between 2 and $3 \times 10^{10} M_{\odot}$ for another three (Table 6). In TXS 0828+193, Nesvadba et al. (2009) found an upper limit of $2 \times 10^{10} M_{\odot}$ in warm molecular gas, which has $1.7 \times 10^{10} M_{\odot}$ of warm ionized gas (Nesvadba et al. 2008b, but using equation 1). Overall, we find fractions of warm ionized to molecular gas masses between 2 and 14% when considering galaxies with CO detections, and between $\geq 20\%$ and 80% when using upper limits on the molecular gas mass in galaxies without CO detections. In comparison, the galaxies of Tacconi et al. (2010), which have CO observations from PdBI and are also included in the sample of Förster Schreiber et al. (2009a) with SINFONI imaging spectroscopy, have ionized-to-molecular mass ratios of few $\times 10^{-4}$. Hopkins & Elvis (2010) showed analytically that blastwaves as driven, e.g., by jets, can deform, ablate, or even destruct clouds, which also lowers their self-shielding capabilities significantly. They suggest that between about 20% and 100% of the gas can become photoionized by the AGN within few times 10^7 yrs, broadly consistent with our results.

5. Spatially resolved properties

5.1. Continuum morphologies

The rest-frame optical continuum morphologies, where detected, are shown as contours in Fig. A.4 to A.8. These morphologies are not contaminated by line emission. They were obtained by collapsing over line-free wavelength ranges over the full available spectral bandwidth, i.e., the H and K-band in case of data taken with the HK grating. We detect the continuum in 23 sources. Most sources have only a single, unresolved continuum source. Exceptions include MRC 0114-211, which has another nearby continuum emitter seen in projection just outside the emission-line region (see §A.1 for details). 3C 257 and

MP 0340–6507 have both an extended continuum. This could either indicate the presence of two partially blended, and presumably interacting sources, as expected in the merger scenario, or extended dust in a single extended source, perhaps dust illuminated by the AGN or extended star-forming regions (e.g., Cimatti et al. 1997; Vernet et al. 2001; Hatch et al. 2008). De Breuck et al. (2010) suggest that extended dust emission could also indicate binary AGN. In MRC 2048–272, we find a second continuum source at a projected distance of $3''$, which is however at a very different redshift, $z=1.52$ (the radio galaxy is at $z=2.06$). This intervening galaxy is also the source of the far-infrared emission reported by Drouart et al. (2014).

Overall, we have therefore little evidence for on-going merging activity in our galaxies. Of course, with a field-of-view of $8'' \times 8''$, corresponding to $64 \text{ kpc} \times 64 \text{ kpc}$ at $z \sim 2$, we are not able to probe the more extended environment where companion galaxies have been found for several of our sources in previous studies (e.g., Chambers et al. 1996; Le Fevre et al. 1996; Kurk et al. 2004; Venemans et al. 2007; Hatch et al. 2011; Koyama et al. 2013; Hayashi et al. 2012; Wylezalek et al. 2013; Cooke et al. 2014; Collet et al. 2015a). With a seeing of typically $1''$, corresponding to 8 kpc at $z \sim 2$, we are not sensitive to advanced major mergers that are approaching coalescence, and we might also miss low-mass or strongly obscured sources (Ivison et al. 2008). However, even relatively distant, early-stage major mergers have been proposed to trigger phases of rapid star formation and galaxy growth in massive high- z galaxies (Hopkins et al. 2007), which does not seem to be the case for most of our sources.

5.2. [OIII] morphologies and surface luminosities

The morphologies of the warm ionized gas in our sources are shown in Figs. A.4 to A.8. Most are very irregular. Isophotal sizes of the bright [OIII] $\lambda 5007$ line emission down to the 3σ depths of our data sets are given in Table 4 along the minor and major axis, respectively. Error bars were derived from the positional accuracy of the point spread function at a signal-to-noise ratio of $S/N=3$, corresponding to the surface-brightness cutoff in our maps, $\text{FWHM} [2 S/N]^{-1}$. We multiply by a factor $\sqrt{2}$ to take into account that we need to measure two positions to obtain the size of a major or minor axis, respectively. Sizes range from the resolution limit ($5\text{--}10 \text{ kpc}$, depending on the seeing at the time of observation of each source, see Table 1) to $69 \text{ kpc} \times 23 \text{ kpc}$ for our largest source, MRC 0156–252.

In Fig. 3 we show the ratios of the major and minor axis in the 27 galaxies with well extended line emission (Table 4) as a function of the size of the major axis. The red dashed and solid lines show the axis ratios that can be measured as a function of the size of the major axis during seeing of $0.5''$, $0.8''$, and $1.0''$, respectively. We find a total range between 2–4, with most ratios between 2 and 3. This range is consistent with the ratios predicted by hydrodynamic “cocoon” models of radio jets, which predict values between 2 and 4 (e.g., Gaibler et al. 2007; Krause 2003; Wagner et al. 2012).

Most galaxies have a single extended emission line region, which is centered on the continuum peak. The peak in [OIII] surface brightness is however not always found at the geometric center of the emission line region. Examples of slightly off-center peaks include BLR 0128–264, or MP 1758–6738, where we find offsets of 4.4 kpc and 6.3 kpc , respectively, seen in projection on the sky. Likewise, the emission-line and continuum peak do not always coincide. For example, in USS 1410–001 or

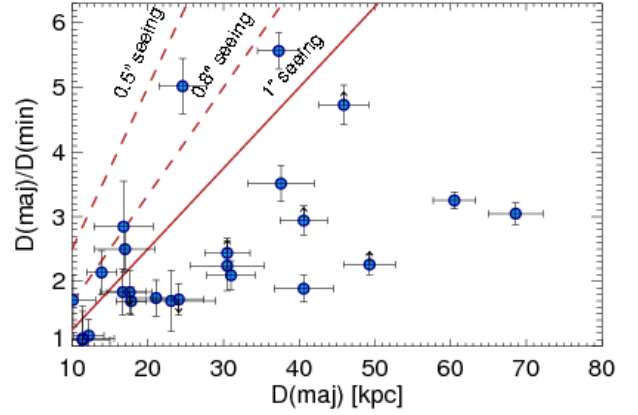


Fig. 3. The ratio between major and minor axis of the extended emission-line regions in our 27 galaxies with well resolved line emission (Table 4), as a function of major axis length. Typical ratios are between 2 and 4. More extended regions are also more elongated.

3C 257, continuum and emission-line surface brightness peaks are offset from each other by about 10 kpc . Three galaxies (TN J1112–2948, MG 2144+1928, and USS1243+036) have multiple bright emission-line regions, which are not connected to each other, at least at the surface brightness levels of about $1\text{--}3 \times 10^{-17} \text{ erg s}^{-1} \text{ cm}^{-2} \text{ arcsec}^{-2}$ that we reach with our data. All three are roughly aligned with the radio jet axis (§5.3).

5.3. Alignment with the radio axis

Alignments between radio jet and extended continuum or emission-line regions are very characteristic of high-redshift radio galaxies (e.g., McCarthy et al. 1991; Cimatti et al. 1997), whereas galaxies with emission-line regions that are perpendicular to the radio jet axis are commonly found in the more nearby Universe. Baum et al. (1992) found that the radio galaxies they classify as ‘rotators’ have disks that are orthogonal to the radio jet axis within about 20° (see also de Ruiter et al. 2002). In Fig. 4 we show a histogram with the offsets in position angle between the extended emission line regions and the radio jets. Because the emission-line morphologies in many galaxies are irregular (and in some cases also the radio morphologies and jet directions), we estimated position angles for each side of the nebulae from the nucleus, and also for each individual radio jet. We include all 23 galaxies with well extended emission-line regions and radio jets from the present work, as well as the previously published sources MRC 0406–244, TXS 0828+193, TN J0205+2242 and MRC 0316–257 from Nesvadba et al. (2008a) and Nesvadba et al. (2007). We also include MG 0340–65, for which McConnell et al. (2012) list a position angle $\text{PA} = 59^\circ$, and USS 1707+105, using the radio morphology shown by Hatch et al. (2011) and the position of the outer cloud as reference for the gas in the northern part of the galaxy.

Fig. 4 shows that jet and emission-line gas are well aligned in the great majority of cases. Offsets are $< 30^\circ$, consistent with the measurement uncertainties (in particular in the lowest-surface brightness areas which are often decisive to determine the major axis of the line-emitting gas, see Fig. A.4 to A.7), jittering of the jet or perhaps jet precession (e.g., Nawaz et al. 2014),

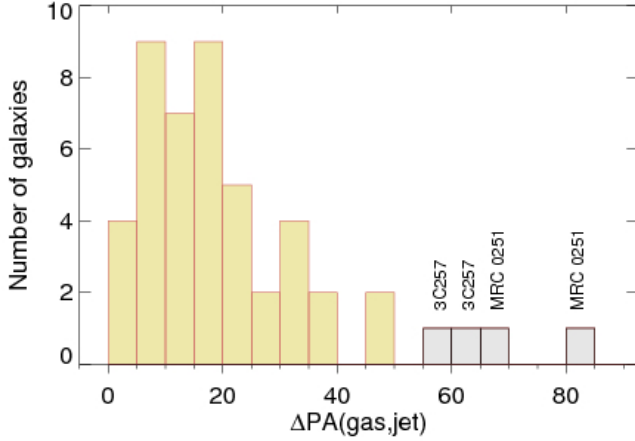


Fig. 4. Offsets in position angle between the major axis of the extended emission-line gas on each side of the nucleus and the associated radio jet for galaxies where jet and gas are well spatially resolved. See §5.3 for details.

and the broad lateral sizes of many emission-line regions in our galaxies perpendicular to the jet direction. Each of these effects can produce offsets in position angle of a few degrees. The axis ratios of typical jet cocoons in hydrodynamic simulations of radio galaxies (e.g., Gaibler et al. 2009; Wagner et al. 2012) suggest maximal misalignments of $20 - 30^\circ$ as we find in our data. More pronounced offsets can be produced by jet deflection on dense clouds (as is not uncommon in HzRGs van Breugel et al. 1998). In all these cases, however, we can safely say that the radio source intercepts a significant part of the emission-line region.

A few sources, however, have offsets that are $> 30^\circ$, and deserve a more detailed discussion. The largest offsets, $> 50^\circ$, are found for MRC 0251–273 and 3C 257, which have both small double radio sources embedded within the ISM of their host galaxy (§7). Another eight jets show offsets between 30° and 50° , namely, the two jets in 4C 23.56, the south-western jet in MRC 1558–003, and the northern jet in USS 1410–001, whereas the second jet is better aligned with the gas. The radio source is much larger than the size of the emission-line region in all these cases, and the axis towards the radio hotspots intercepts at least parts of the gas. In two of these cases, the gas kinematics are perturbed along the jet direction: In MRC 1558–003, faint extended radio emission extends from the radio core towards the south-western jet through a narrow funnel-like structure with high gas velocities ($+500 \text{ km s}^{-1}$). In USS 1410–001, the highest velocities in the northern emission-line cloud are also found along the direction towards the radio hotspot. The jets in both galaxies therefore seem to have been deflected through jet-cloud interactions. In USS 1410–001, this interaction must have occurred under a grazing angle.

We discuss two more outliers with very large radio sources and large offsets in position angle, $\geq 60^\circ$, NVSS J210626–314003 and TXS 2353–003 in detail in Collet et al. (2015a). Unlike MRC 0251–273 and 3C 257, which have equally large offsets, but radio jets that are still embedded within the ISM of their host galaxy, these galaxies have very extended radio sources $> 100 \text{ kpc}$. We also do not see any gas associated with the direction of the radio jets in the two Collet et al. sources, suggesting that the jet and gas are not interacting in a direct way.

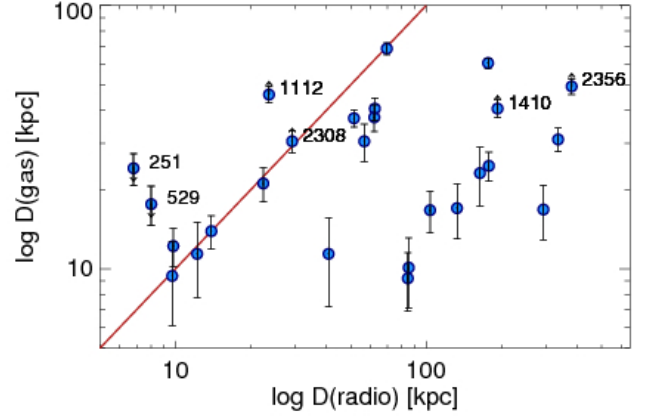


Fig. 5. Size of the bright emission-line regions as a function of the largest angular scale of the radio jet in the 27 sources with well extended emission-line regions. We label sources with upper and lower limits, respectively. In MRC 0251–273 and PKS 0529–549, the jet has not yet broken out of the ISM, see §7

5.4. Jet and emission-line region sizes and axis ratios

In Fig. 5 we compare the sizes of the emission-line regions with those of the radio jets. The red line shows the one-to-one relationship between the two. The two sizes are not correlated, however, in most sources, the emission-line gas extends over radii that are smaller than the radio jet size. Eight galaxies have line emission that extends over similar radii as the radio jets. Three galaxies have line emission that is significantly more extended than the jet size. This includes two galaxies where we do not spatially resolve the line emission in our SINFONI data, and which are shown as upper limits in Fig. 5. Line emission in these galaxies extends over sizes $< 10 \text{ kpc}$, typical sizes of high- z galaxies without radio jets and similarly deep or even deeper SINFONI observations (e.g., Förster Schreiber et al. 2009b). In galaxies with compact radio sources, the onset of the jet activity could be too recent for the jet cocoon to have encompassed the large-scale interstellar medium of the host galaxy (e.g., Owsianik & Conway 1998; Murgia et al. 1999).

In another 18 galaxies with radio sizes between 15 kpc and 200 kpc , and gas sizes between 10 kpc and 70 kpc , the radio jets have already broken out of their host galaxy, with radio sizes that exceed the size of the emission-line regions by up to about an order of magnitude. Although we find galaxies that have much larger radio sources than emission-line regions for all gas sizes, we do not find any galaxy with emission-line regions greater than 70 kpc .

The SINFONI field-of-view of nominally $8'' \times 8''$ covers very similar ranges at $z \sim 2$, $64 \text{ kpc} \times 64 \text{ kpc}$, but this is not the reason for this cut-off. Our dither strategy (§2) required us to obtain small mosaics, which cover about twice as large a size along the radio jet axis, and are significantly larger than the sizes of the emission-line regions in most cases.

In four galaxies, however, the line emission does extend to near the edge of the data cubes. These galaxies are 4C 23.56, TN J1112–2948, USS 1410–001, and MG 2308+0336. These galaxies are formally shown as lower limits in Fig. 5, but we do not expect that their emission-line sizes exceed the SINFONI field-of-view. In USS 1410–001, Villar-Martín et al. (2003) find from optical longslit spectroscopy that bright $\text{Ly}\alpha$ emission ex-

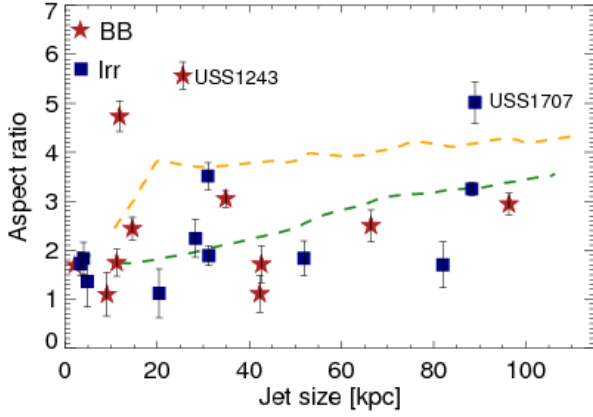


Fig. 6. Aspect ratio (size along the major/minor axis) of the emission-line region as a function of the jet size. Red stars and blue boxes show sources with bipolar velocity fields and more complex kinematics, respectively. The orange and green lines are for density parameters of 0.1 and 10^{-3} between jet and ambient medium, respectively, and are taken from Gaibler et al. (2009). We only show the 22 sources from Table 4 with well resolved emission-line regions, which also have jet sizes $\text{LAS}/2 \leq 120$ kpc, the size range modeled by Gaibler et al. (2009).

tends out to about $10''$ along the radio jet axis, comparable to the size we measure in $[\text{OIII}]\lambda 5007$. Tanaka et al. (2011) obtained $\text{H}\alpha$ narrow-band imaging of 4C 23.56 down to a flux limit of $7.5 \times 10^{-17} \text{ erg s}^{-1} \text{ cm}^{-2}$, finding a size of about $7''$ for the radio galaxy along the radio jet axis (Tanaka, private communication). MG 2308+0336 has a radio size that is comparable to the SINFONI field-of-view (right panel of Fig. A.8). For TN J1112–2948, we obtained a second pointing around the northern bubble, but did not find any bright nearby line emission.

The elongation of the line emission is another interesting quantity, that can also be compared with expectations from jet cocoon models. In Fig. 6 we show the ratios of major to minor axis of the emission-line regions as a function of the size of the radio jets, finding a mild trend towards more elongated emission-line regions with increasing radio jet size. Correlation probabilities implied by the Spearman’s rank test and Kendall’s tau are 0.02 and 0.03, respectively, i.e., a random distribution is excluded at confidence levels of 0.98 and 0.97, respectively. An increasing elongation as observed here is expected in cocoon models of light jets, because the bow shock should expand faster than the blastwave as the cocoon grows larger (Krause 2003). These models also predict a range of factors 2–4 between the major and minor axis of the emission-line gas, in agreement with our data (§5.2 and Fig. 3).

In Fig. 6 we also make a more specific comparison with the model predictions of Gaibler et al. (2009). The yellow and green lines show density parameters (i.e., the density ratio between jet and ambient gas) of 0.1 and 10^{-3} , respectively. Values for both densities are in good correspondence to the overall data set, in particular when taking into account that the density parameter in high-redshift galaxies is likely to be smaller (e.g., Krause 2003, suggest 10^{-4} for Cyg A and high- z radio galaxies). We do not find significant differences between galaxies with regular back-to-back and irregular kinematics.

5.5. Comparison of $[\text{OIII}]\lambda 5007$ and $\text{H}\alpha$ morphologies

The $[\text{OIII}]\lambda\lambda 4959, 5007$ lines are observationally very convenient to study the morphology and kinematics of the warm ionized gas in HzRGs. They are the brightest emission lines in the rest-frame optical spectra of most powerful HzRGs, and they do not suffer blending with other nearby lines, except in the few galaxies with broad nuclear emission lines. However, the broad component of $\text{H}\beta$ is spectrally well offset from the $[\text{OIII}]\lambda\lambda 4959, 5007$ lines, faint, and are a few times broader than $[\text{OIII}]$, which allows us to clearly distinguish it from the $[\text{OIII}]\lambda\lambda 4959, 5007$ doublet (Nesvadba et al. 2011b). Having two lines probing the same gas is also convenient to keep track of uncertainties due to telluric features.

However, O^{++} is a minor constituent of the gas, and the lines are more sensitive to temperature, metallicity, and ionization parameter than the mass of warm ionized gas (e.g., Ferland 2003). We should therefore verify that the $[\text{OIII}]\lambda 5007$ morphology and kinematics is indeed an adequate representative of the overall distribution and kinematics of the warm ionized gas.

Several of our galaxies are bright and extended enough to allow for a detailed comparison between the morphologies of $[\text{OIII}]\lambda 5007$ and $\text{H}\alpha$. In Fig. 7 we show maps of the $\text{H}\alpha$ -to- $[\text{OIII}]\lambda 5007$ ratios in the nine galaxies where such a comparison is possible. In a 10^{th} galaxy, TN J1112–2948, $\text{H}\beta$ is bright enough for a similar analysis (Fig. 9). Line ratios change within factors of typically 2–4 in individual galaxies, but the overall morphologies of the emission-line regions traced in either line are very similar in all galaxies. Both lines are emitted from similar environments, although the detailed local gas conditions (or extinction) may change.

To isolate $\text{H}\alpha$ and $[\text{NII}]\lambda\lambda 6548, 6583$, we had to impose the same kinematic properties for $\text{H}\alpha$ and the $[\text{NII}]\lambda\lambda 6548, 6583$ lines which we had previously measured for $[\text{OIII}]\lambda 5007$. The height of each Gaussian was however a free parameter in our fits, and so these maps would have shown less extended $\text{H}\alpha$ or $\text{H}\beta$ emission-line regions if such a difference to $[\text{OIII}]$ was present. Visual inspection of the data cubes ensured that we are not missing any $\text{H}\alpha$ emission (blended with $[\text{NII}]$) that is more extended than $[\text{OIII}]$.

Performing a similar analysis for the velocity offsets and line widths is more difficult because the blending of the $\text{H}\alpha$ and $[\text{NII}]$ lines makes it more challenging to probe the line wings and to account for spectral shifts. However, the small residuals in the integrated spectra of $\text{H}\alpha$ and $[\text{NII}]$ after our constrained line fits are small (of-order a few percent), which gives us confidence that the overall kinematic properties measured in both lines are generally comparable. Unfortunately, the extended $\text{H}\beta$ emission is too faint in these galaxies to produce resolved extinction maps (but see Nesvadba et al. 2008a, for extinction maps of two other HzRGs with comparable properties to our sources.)

5.6. Emission-line surface brightnesses

We also investigated whether trends exist between the emission-line surface luminosity of $[\text{OIII}]\lambda 5007$ and $\text{H}\alpha$ and various other parameters. We prefer to investigate surface luminosities instead of surface brightness to minimize the impact of cosmological surface-brightness dimming for our results, which scales as $(1+z)^4$ for spectrally integrated line fluxes, corresponding to factors 33 to 1132 for our sources.

We used the line maps extracted from our SINFONI data cubes and extracted the highest emission-line surface luminosities, the average surface luminosity, and the most common

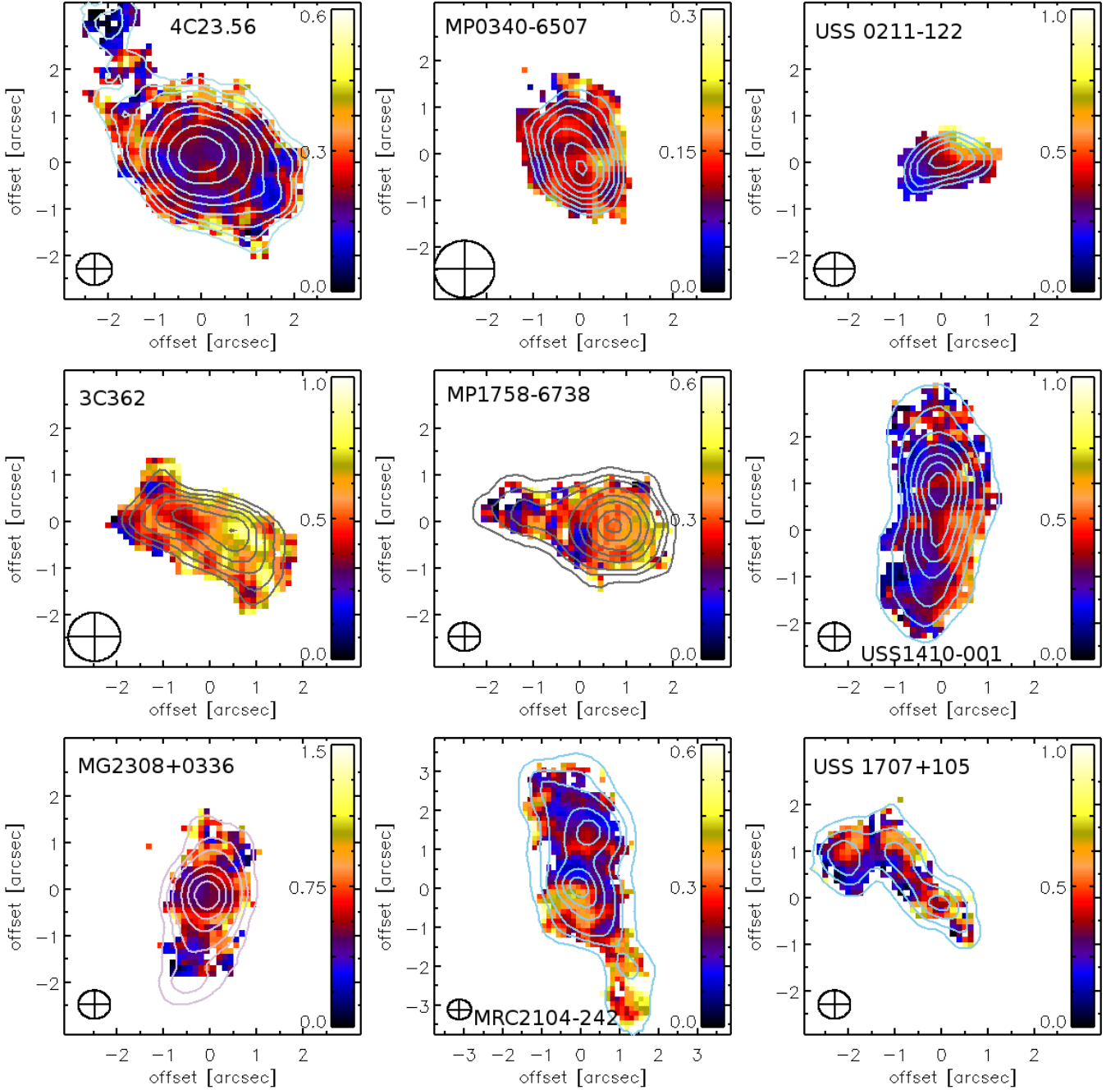


Fig. 7. Ratios of $H\alpha$ to $[OIII]\lambda 5007$ for nine galaxies with extended emission-line regions and at redshifts where we cover both lines with our SINFONI data cubes. Contours show the $[OIII]\lambda 5007$ morphology. The ellipse in the lower left corner illustrates the size of the seeing disk.

surface luminosities, i.e., the peak of the histograms of the $[OIII]\lambda 5007$ surface luminosities extracted from each individual pixel. We also calculated the sum of the line emission in all spatial pixels to derive the total line flux. We did not find any obvious trends between surface luminosity and the size or axis ratio of the emission line regions.

6. Gas kinematics

6.1. Velocity patterns and total velocity offsets

The central panels of Fig. A.4 to A.8 show the maps of relative velocities in the extended emission-line regions of our sources.

Total velocity offsets range from 100 km s^{-1} to 2000 km s^{-1} . The lowest value is measured in TN J2007–1316, which is only marginally resolved and where the observed velocity offset is probably significantly lowered by beam smearing effects. The median velocity offset in all targets is 680 km s^{-1} .

To obtain robust results in spite of occasional velocity spikes in low signal-to-noise pixels towards the periphery of our sources, we did not consider isolated pixels with very high velocity offsets near the edge of our targets for our velocity estimates. Finding such values in isolated pixels is inconsistent with the smoothing expected from oversampling the seeing disk like we do in our data sets (a typical seeing disk with $\text{FWHM} \sim 0.8 - 1''$ is sampled with pixels of $0.125'' \times 0.125''$). Typical uncertainties

Source	LAS [arcsec]	LAS [kpc]	$\log P_{500}$ [W Hz ⁻¹]	$\log P_{1.4}$ [W Hz ⁻¹]	$\log P_{151}$ [W Hz ⁻¹]	$\log E_{\text{mech,W}}$ [erg s ⁻¹]	$\log E_{\text{mech,C}}$ [erg s ⁻¹]
MRC 0114-211	0.7	5.9	28.8±0.1	28.6±0.1	29.1±0.1	47.0±0.3	47.4±0.3
TN J0121+1320	0.3	2.2	28.5±0.1	28.0±0.1	29.1±0.1	47.0±0.3	47.0±0.3
BRL 0128-264	35.8	293.6	29.1±0.1	28.8±0.1	29.7±0.1	47.5±0.3	46.6±0.3
MRC 0156-252	8.3	69.7	28.5±0.1	28.0±0.1	28.9±0.1	46.8±0.3	47.0±0.3
TN J0205+2242	2.7	19.7	28.5±0.1	28.0±0.1	29.1±0.1	47.0±0.3	47.0±0.3
USS 0211-122	16.2	132.8	28.5±0.1	28.0±0.1	29.0±0.1	46.9±0.3	47.0±0.3
MRC 0251-273	0.9	6.8	28.5±0.1	28.3±0.1	29.0±0.1	46.9±0.3	47.2±0.3
RC J0311+0507	2.8	18.5	29.5±0.1	29.1±0.1	30.0±0.1	47.7±0.3	47.8±0.3
MRC 0316-257	7.6	57.8	29.0±0.1	28.5±0.1	29.5±0.1	47.3±0.3	47.4±0.3
MP J0340-6507	20.0	164.0	28.8±0.1	28.3±0.1	29.5±0.1	47.3±0.3	47.2±0.3
MRC 0406-244	7.3	59.1	29.0±0.1	28.6±0.1	29.7±0.1	47.5±0.3	47.5±0.3
PKS 0529-549	1.0	8.0	29.2±0.1	28.6±0.1	29.8±0.1	47.6±0.3	47.5±0.3
TXS 0828+193	20.0	160.	28.4±0.1	27.9±0.1	29.0±0.1	46.9±0.3	46.9±0.3
5C 7.269	0.5	4.2	27.8±0.1	27.4±0.1	28.3±0.1	46.3±0.3	46.6±0.3
MRC 1017-220	8.3	70.6	28.1±0.1	27.9±0.1	28.2±0.1	46.2±0.3	46.9±0.3
TN J1112-2948	3.1	23.6	28.8±0.1	28.2±0.1	29.5±0.1	47.3±0.3	47.2±0.3
TXS 1113-178	10.3	84.5	28.5±0.1	28.1±0.1	29.0±0.1	46.9±0.3	47.1±0.3
3C 257	12.8	103.7	29.2±0.1	29.1±0.1	29.4±0.1	47.2±0.3	47.8±0.3
MRC 1138-262	11.4	94.6	29.1±0.1	28.6±0.1	29.7±0.1	47.5±0.3	47.5±0.3
USS 1243+036	7.0	51.1	29.2±0.1	28.7±0.1	29.9±0.1	47.7±0.3	47.5±0.3
MG 1251+1104	1.2	9.8	28.4±0.1	28.0±0.1	28.9±0.1	46.8±0.3	47.0±0.3
MRC 1324-262	1.7	13.9	28.5±0.1	28.1±0.1	28.9±0.1	46.8±0.3	47.1±0.3
TN J1338-1942	1.4	9.7	28.7±0.1	28.3±0.1	29.3±0.1	47.1±0.3	47.2±0.3
USS 1410-001	23.5	192.7	28.4±0.1	28.0±0.1	29.0±0.1	46.9±0.3	47.0±0.3
MRC 1558-003	7.7	62.4	28.8±0.1	28.4±0.1	29.5±0.1	47.3±0.3	47.3±0.3
USS 1707+105	21.7	177.9	28.6±0.1	28.2±0.1	29.1±0.1	47.0±0.3	47.2±0.3
3C 362	6.9	56.6	28.9±0.1	28.6±0.1	29.4±0.1	47.2±0.3	47.5±0.3
MP 1758-6738	40	336.	29.0±0.1	28.0±0.1	28.5±0.1	47.3±0.3	47.0±0.3
TN J2007-1316	12	85.2	29.1±0.1	28.5±0.1	29.9±0.1	47.7±0.3	47.4±0.3
MRC 2025-218	5.1	40.8	28.7±0.1	28.3±0.1	29.3±0.1	47.1±0.3	47.2±0.3
MG 2037-0011	0.2	1.7	27.9±0.1	27.6±0.1	28.2±0.1	46.7±0.3	46.2±0.3
MRC 2048-272	6.7	55.6	28.7±0.1	28.2±0.1	29.4±0.1	47.2±0.3	47.2±0.3
MRC 2104-242	21.8	176.6	28.8±0.1	28.4±0.1	29.5±0.1	47.3±0.3	47.3±0.3
4C 23.56	47.0	380.7	28.9±0.1	28.4±0.1	29.5±0.1	47.3±0.3	47.3±0.3
NVSS J2135-3337	0.5	4.1	27.0±0.1	27.2±0.1	28.5±0.1	46.5±0.3	46.4±0.3
MG 2144+1928	8.5	62.0	29.1±0.1	28.6±0.1	29.6±0.1	47.4±0.3	47.5±0.3
MRC 2224-273	0.4	3.3	27.8±0.1	27.6±0.1	27.9±0.1	45.9±0.3	46.7±0.3
TN J2254+1857	2.7	22.4	27.8±0.1	27.2±0.1	28.5±0.1	46.5±0.3	46.4±0.3
MG 2308+0336	3.6	29.2	28.5±0.1	28.3±0.1	28.9±0.1	46.8±0.3	47.2±0.3
TXS 2353-003	38.8	310.4	28.8±0.1	28.3±0.1	29.3±0.1	47.1±0.3	47.2±0.3

Table 3. Radio size, radio power and kinetic jet energy estimates. Errors are the measurement uncertainties, except for the kinetic power where we use the scatter in the relationships we used to derive our estimates. We do not provide uncertainties for the Largest Angular Scale, because these are strongly dominated by the dynamic range, resolution, and frequency of the data set used, which in our case is rather heterogeneous. For all but the very compact sources, these uncertainties are in the range of few percent.

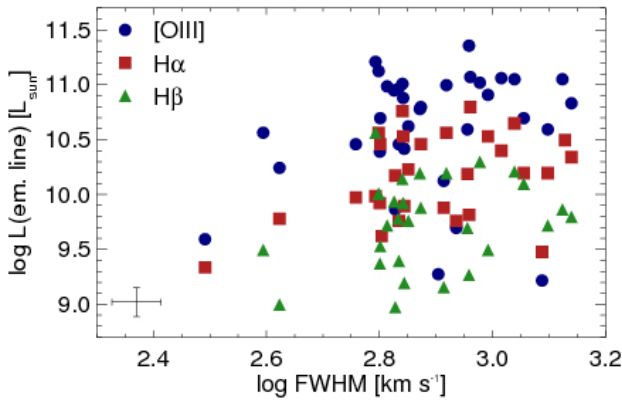


Fig. 8. Emission-line luminosity as a function of FWHM line width for [OIII] λ 5007, H α , and H β . All three lines show trends of increased luminosity with increasing line width.

of the velocity offsets are between 30 and 50 km s⁻¹. Velocity offsets for individual sources are listed in Table 4.

Inspection of Figs. A.4 to A.8 shows the immense variety of velocity patterns in our galaxies. We broadly distinguish between sources with regular velocity fields, where monotonic, large-scale velocity gradients dominate, that are approximately aligned along the major axis of the emission-line region. Galaxies with irregular velocity fields show multiple velocity minima and maxima. Good examples for regular velocity fields are, e.g., MRC 0156–252 or 4C 23.56. Irregular fields are found, e.g., in USS 1707+105, or MRC 2025–218.

Table 4 lists our classification as either bipolar, i.e., ‘back-to-back’, monotonically rising or falling gradients (‘BB’) or irregular velocity fields (‘Irr’). We label compact sources with ‘C’, where we cannot exclude that the compactness of the line emission is smearing out any putative velocity offset. In total, we find 17 sources that are dominated by monotonic large-scale gradients. Fifteen have more obvious irregular velocity components (see Figs. A.4 to A.8). In three galaxies with compact line emis-

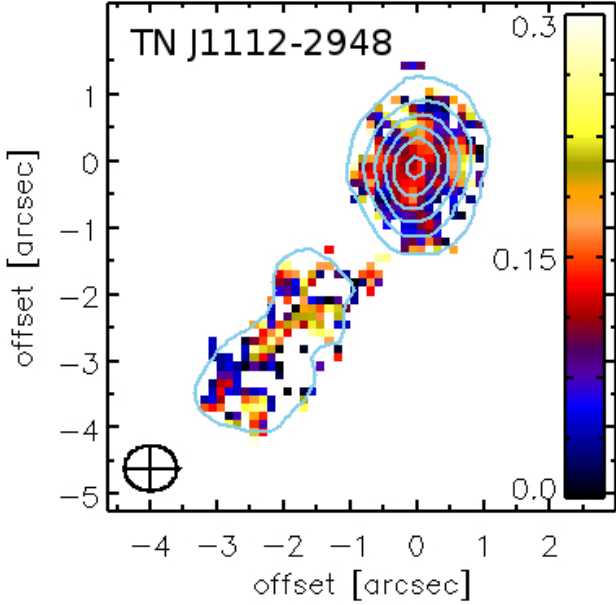


Fig. 9. Ratios of $H\beta$ and $[OIII]\lambda 5007$ fluxes in TN J1112–2948 at $z=3.09$.

sion we do not see any velocity offsets, and attribute this to the compactness of the source.

The right panels of Figs. A.4 to A.8 also show the gas morphology and kinematics with the radio morphology overlaid as contours. Most radio maps were obtained at observed frequencies between 1.4 GHz and 8.5 GHz, with typical resolutions of $1''$ or better. Observation parameters for individual sources can be found in Table 2.

Several sources have extended radio morphologies associated with the emission-line regions, which enable a more detailed comparison. Two radio galaxies, MRC 0251–271 and 3C 257 have small double radio sources which have either not yet broken out of the surrounding interstellar gas, or which are seen under particularly small angles to the line of sight. In MG 2308+0336, the radio source is just adjacent to the emission line region, suggesting that the jet has apparently just broken out of the cocoon of hot gas. The velocity offsets and line widths are greatest in the periphery of the emission-line region and adjacent to the radio lobes. In USS1243+036, both bubbles, although not directly connected to the central region of the galaxy, are associated with radio emission. In the southern bubble, the jet escapes from the gas cloud at an intermediate radius, and is associated with a region where the gas shows a velocity jump and increase in line width. In PKS 0529–549, we see two knots of radio emission well within the extended emission line region. Both radio knots are associated with regions of high velocity offsets and broad line widths.

6.2. Line widths

FWHM (full-width-at-half-maximum) line widths are shown in the right panel of Figs. A.4 to A.8, and are between 450 km s^{-1} and 3200 km s^{-1} . This is significantly higher than the line widths found by Buitrago et al. (2014) in a sample of mass-selected galaxies at $z \sim 1.5$ with stellar masses of few $10^{11} M_{\odot}$, comparable to the stellar masses in our sources (Seymour et al. 2007; De Breuck et al. 2010), suggesting that another mechanism than gravity maintains the FWHM in our sources as high

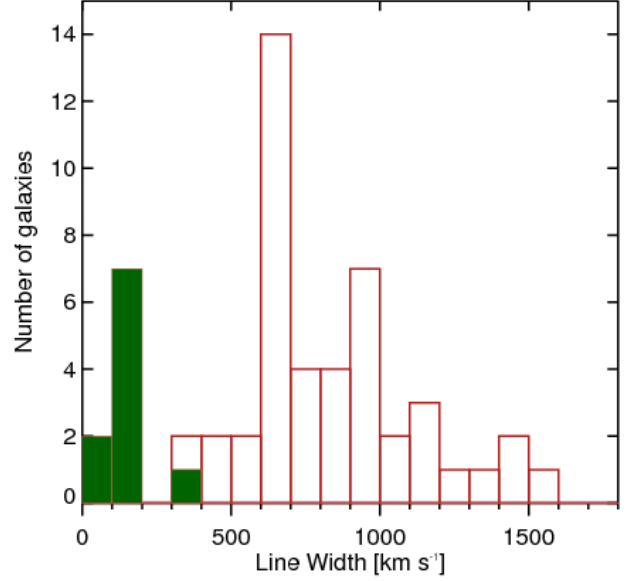


Fig. 10. Comparison of the FWHM line widths in our targets (empty red histogram) and the galaxies of Buitrago et al. (2014) at $z \sim 1.5$, which have comparably high stellar masses, but not prominent AGN (green filled histogram).

as observed. In Fig. 10 we show a comparison of the line widths in the Buitrago et al. (2014) sample and for our galaxies.

All sources have irregular FWHM maps. Some of the galaxies with well extended emission-line gas, e.g., MRC 2025–218, show large jumps in FWHM within about the size of a seeing disk of up to $\sim 800 \text{ km s}^{-1}$. FWHMs in galaxies with two rather symmetric bubbles can have very different FWHMs on either side. Examples are USS 1410–001, where gas in the northern lobe reaches $\text{FWHM} \sim 900 \text{ km s}^{-1}$, compared to only 450 km s^{-1} in the southern lobe. In 3C 257, we find a FWHM gradient that runs nearly perpendicular to the major axis of the gas, with FWHMs increasing from 500 km s^{-1} to 1300 km s^{-1} from the north-east to the south-west. Not always are regions of broad FWHMs and high velocity offsets associated with each other. For example in TN J1338–192, the gas with the lowest line widths ($\text{FWHM} \sim 500 \text{ km s}^{-1}$) is also at the highest redshift ($+500 \text{ km s}^{-1}$ relative to the average). Some galaxies, e.g., MRC 2025–218, have multiple regions of very broad line emission, however, 4C 23.56 has uniformly broad lines ($\text{FWHM} \sim 800 \text{ km s}^{-1}$) that only become more narrow in the very periphery of the emission-line region.

The maximal FWHM is generally not associated with the central regions of the host galaxies, as probed by the position of the continuum peak. This is only the case for BLR 0128–264, TXS 1113–178, MG 1251+1104, MRC 2025–218, NVSS J2135–3337, and MRC 2224–273. In, e.g., MG 2308+0336, the gas near the nucleus is in fact the gas with the lowest FWHM: FWHMs are $\sim 1200 \text{ km s}^{-1}$ in the southern periphery adjacent to the radio lobe, and only $\text{FWHM} \sim 500 \text{ km s}^{-1}$ near the center.

Even galaxies with regular, clearly bipolar velocity fields have irregular FWHM distributions. The broadest FWHMs are not generally associated with the largest velocity gradients in these galaxies, which rules out beam smearing as primary cause. Moreover, the FWHMs are generally comparable to, if not larger

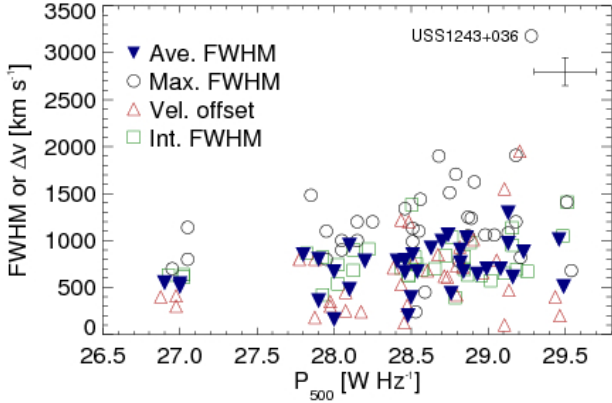


Fig. 11. FWHM and velocity offsets as a function of the jet power at 500 MHz in the 25 galaxies with extended emission-line regions from our sample. We also add 9 targets from Collet et al. (2015b) to enhance the number of galaxies with radio power below $10^{28.5}$ erg s $^{-1}$.

than, the large-scale velocity gradients in our sources, further limiting the potential effects of beam-smearing (a notable exception is however BLR 0128–264). This of course applies only to the large-scale velocity gradients that we spatially resolve. Local FWHM maxima could trace gas flows on scales unresolved in our data, which can encompass regions of several kpc.

Given this great complexity, it is obviously not straightforward to define one characteristic FWHM for each galaxy, which can then be compared with other sources. We have therefore considered several quantities:

Firstly, probably the easiest way to obtain a luminosity-weighted global estimate is by integrating the data cube over all pixels where line emission is detected after removing the local offsets measured from the velocity maps. Since most of our FWHM maps are derived from [OIII] λ 5007, which has a line flux that is more strongly determined by the ionization parameter than gas mass (e.g., Ferland 2003), this is in essence an ionization-weighted FWHM. FWHMs obtained in this way are listed for each galaxy and line in Table A.5. Secondly, we also list the median FWHM in each source in Table 4 to give an estimate of the ‘typical’ FWHM in each galaxy that is measured in most pixels. This may serve as an approximation to the projected, geometrically weighted FWHM. Thirdly, in the same table we also list the maximal FWHMs found in smaller regions of each galaxy, but still over apertures of several pixels to avoid bias by noisy pixels.

The FWHM line widths are not correlated with the emission-line luminosities. In Fig. 8 we show this on the example of the luminosity-weighted integrated widths (the first method). The figure includes all 35, 29, and 28 galaxies with [OIII] λ 5007, H α , and H β where these lines have been measured in our sample. Spearman rank test and Kendall’s τ rule out non-significant correlations only at probabilities 0.27, 0.14, and 0.27 for [OIII] λ 5007, H α , and H β , respectively.

In Fig. 11 we show the velocity offsets, average, maximum, and integrated line widths as a function of the jet power at 500 MHz in the rest frame (the kinematic properties and the jet power of individual galaxies are listed in Tab. 4 and 3, respectively). All quantities increase with increasing radio power, although the scatter is large. Spearman rank tests and Kendall’s τ exclude non-significant correlations at confidence levels of 0.1

and better. The tightest relationship is between radio power and average FWHM, with confidence levels of 0.02 and 0.015 for Kendall’s τ and the Spearman rank test, respectively.

We also investigated whether the properties of the gas and radio emission in the two main classes ‘BB’ and ‘Irr’ depended on whether a given galaxy falls into one class or another. We did not find significant trends with radio size, radio power, or jet kinetic energy. A Kolmogorov-Smirnov test suggests probabilities of between 0.2 and 0.9 that the two classes are drawn from the same overall distribution of these parameters amongst our full sample. Likewise, we did not find significant differences in the sizes of emission-line regions and kinematic parameters (velocity offsets, average and maximal Gaussian line widths, i.e., FWHM/2.355). Probabilities that both subsets are distinguishable in other parameters, including FWHM and velocity offsets alone, are between 0.1 (for velocity offsets) and 0.9 (for radio power), which is not significant. The only quantity where we do see a significant difference between the two classes is the ratio between bulk and unordered velocities, which we will discuss in the next subsection.

6.3. Ratio of velocity gradients and line widths

The ratios between velocity gradient and line widths provide interesting constraints on the importance of ordered bulk motion and unordered, possibly turbulent motion of the gas. In galaxies considered to be dominated by large-scale rotation, such estimates are usually derived by using the large-scale velocity gradient and the central velocity dispersion (Förster Schreiber et al. 2009b). However, given the more complex velocity fields of our sources, the situation is less straight-forward in this case. We therefore list two values in Table 4. Firstly, we state the $v/2\sigma_{\text{ave}}$, using the Gaussian line width derived from the average FWHM (i.e., $\sigma_{\text{ave}} = \text{FWHM}_{\text{ave}}/2.355$) in the maps, and secondly, the $\Delta v/2\sigma_{\text{max}}$ using the Gaussian width corresponding to the broadest FWHM in each source. Δv is the total velocity gradient, and we divide by an additional factor 2 to obtain values that are comparable to those found for other samples of high- z galaxies, where v approximates the circular velocity. We consider these two quantities representations of the typical and maximal kinematic perturbations of the gas, respectively. Generally, we find that the maximal FWHM is a factor 2–3 higher than the average FWHM, with little dependence on the average or maximal FWHM (upper panel of Fig. 12). An exception is USS 1243+036, which has unusually broad line widths of FWHM=2500 km s $^{-1}$ in the central regions (§A.14).

We find however higher ratios of $\Delta v/2\sigma$ in the sources with the most extended emission-line gas (lower panel of Fig. 12). The reason for this difference is two-fold. Firstly, the largest nebulae have also particularly large velocity offsets: all galaxies with v/σ ratios >1.1 have regular velocity fields, and are those which also have $\Delta v \geq 1000$ km s $^{-1}$. Secondly, they have lower line widths than the more compact sources. The upper panel of Fig. 12 shows that this holds for the average as well as the maximal FWHM. Spearman’s rank test and Kendall’s τ , respectively, rule out with probabilities of 1.1×10^{-4} and 2.6×10^{-4} , respectively, that the average v/σ are uncorrelated with the major axis. For the maximum widths, v/σ_{max} , this can be ruled out with probabilities of 2.3×10^{-3} and 1.1×10^{-3} . We did not find a correlation between v/σ and radio size (Fig. 13).

Source	[OIII] size [kpc×kpc]	FWHM _{avg} [km s ⁻¹]	FWHM _{max} [km s ⁻¹]	Δv [km s ⁻¹]	v/σ _{avg}	v/σ _{max}	Kin. class
BRL 0128–264	16.8 ± 3.9 × 5.9 ± 2.7	1300 ± 124	1910 ± 182	1550 ± 148	1.4 ± 0.2	1.0 ± 0.2	BB
MRC 0156–252	68.6 ± 3.6 × 22.5 ± 3.6	660 ± 21	990 ± 31	1220 ± 38	2.3 ± 0.1	1.5 ± 0.1	BB
USS 0211–122 ¹	17.0 ± 4.0 × 6.8 ± 1.5	200 ± 32	240 ± 39	124 ± 20	0.6 ± 0.2	0.4 ± 0.2	BB
MRC 0251–273	24.1 ± 3.3 × 14.0 ± 2.9	670 ± 54	450 ± 36	780 ± 64	0.7 ± 0.4	0.6 ± 0.2	Irr
RC J0311+0507	11.4 ± 3.6 × 10.4 ± 3.2 ²	510 ± 20	680 ± 27	200 ± 8	0.5 ± 0.1	0.3 ± 0.1	BB
MP J0340–6507	23.1 ± 5.8 × 13.6 ± 5.4	900 ± 137	1250 ± 190	420 ± 64	0.5 ± 0.1	0.4 ± 0.1	Irr
PKS 0529–549	17.6 ± 3.0 × 9.6 ± 2.7	610 ± 36	820 ± 48	470 ± 28	0.9 ± 0.1	0.7 ± 0.1	Irr
sTN J1112–2948	45.9 ± 3.3 × 9.7 ± 2.9	437 ± 23	780 ± 35	610 ± 27	1.6 ± 0.2	0.9 ± 0.2	BB
TXS 1113–178	9.2 ± 2.3 × 8.3 ± 2.3	790 ± 70	1130 ± 100	530 ± 47	0.8 ± 0.3	0.6 ± 0.1	BB
3C 257	16.7 ± 3.0 × 9.1 ± 2.8	1010 ± 88	1410 ± 123	400 ± 35	0.5 ± 0.1	0.3 ± 0.1	Irr
USS 1243+036	37.3 ± 2.8 × 6.7 ± 1.8	880 ± 22	3180 ± 57	1950 ± 35	2.6 ± 0.2	0.7 ± 0.1	BB
TN J1338–1942	9.4 ± 3.3 × 6.9 ± 2.7	994 ± 47	1510 ± 71	850 ± 40	1.0 ± 0.3	0.7 ± 0.1	Irr
USS 1410–001	40.6 ± 3.1 × 13.8 ± 2.9	780 ± 52	1340 ± 89	710 ± 47	1.1 ± 0.1	0.6 ± 0.1	BB
MRC 1558–003	40.6 ± 3.9 × 21.5 ± 3.9	763 ± 82	1050 ± 112	730 ± 78	1.1 ± 0.1	0.8 ± 0.1	Irr
USS 1707+105	24.6 ± 3.1 × 4.9 ± 2.0	920 ± 87	1900 ± 179	680 ± 64	0.8 ± 0.1	0.4 ± 0.2	Irr
3C 362	30.5 ± 4.9 × 13.6 ± 4.7	1030 ± 122	1625 ± 192	720 ± 85	0.8 ± 0.1	0.5 ± 0.2	Irr
MP 1758–6738	31.0 ± 3.2 × 14.8 ± 2.9	700 ± 75	1060 ± 114	660 ± 71	1.1 ± 0.2	0.7 ± 0.1	BB
TN J2007–1316	10.1 ± 3.0 × 5.9 ± 1.4	970 ± 140	1200 ± 173	100 ± 73 ³	0.1 ± 0.1	0.1 ± 0.1	BB
MRC 2025–218	27.0 ± 4.2 × 8.9 ± 3.4	1060 ± 97	1707 ± 157	620 ± 57	0.7 ± 0.2	0.4 ± 0.1	Irr
MRC 2104–242	60.5 ± 2.8 × 18.6 ± 2.3	670 ± 27	1237 ± 52	930 ± 39	1.6 ± 0.2	0.9 ± 0.2	Irr
4C 23.56	49.3 ± 3.4 × 21.8 ± 3.1	640 ± 21	1060 ± 36	1010 ± 40	1.8 ± 0.2	1.2 ± 0.1	BB
NVSS J2135–3337	17.8 ± 1.8 × 10.5 ± 1.8	510 ± 25	1140 ± 43	410 ± 59	1.0 ± 0.2	0.4 ± 0.2	BB
MG 2144+1928	37.6 ± 4.4 × 10.7 ± 2.7	700 ± 73	1930 ± 164	790 ± 28	1.3 ± 0.1	0.5 ± 0.2	Irr
TN J2254+1857	21.1 ± 3.2 × 12.1 ± 2.8	850 ± 63	1483 ± 109	800 ± 59	0.5 ± 0.1	0.3 ± 0.2	BB
MG 2308+0336	30.5 ± 3.0 × 12.5 ± 2.7	850 ± 53	1440 ± 90	1200 ± 75	1.7 ± 0.2	1.0 ± 0.2	BB

Table 4. Properties of extended emission-line regions. The [OIII] size is the full projected length of the emission-line region along the major and minor axis, respectively, and deconvolved with the size of the seeing disk. We only list galaxies of type “BB” (bipolar velocity fields akin to back-to-back outflows) or “Irr” (irregular kinematics).

7. Feedback

There is little doubt today that the bright, extended emission-line regions in HzRGs are photoionized by powerful obscured quasars in their nuclei (e.g., Villar-Martin et al. 1997; Humphrey et al. 2008). Based on a small number of HzRGs with imaging spectroscopy (four with extended, two with compact radio sources), we have previously argued that the energy injection from the AGN into the gas of the host galaxy is also at the origin of the irregular gas kinematics with high velocities and line widths in HzRGs (Nesvadba et al. 2006b, 2008a).

The results of our present study enable us to expand our previous analyses in several ways, and to investigate whether the arguments we put forward in these studies also hold for HzRGs generally. Our SINFONI maps show a much larger diversity in gas morphologies and kinematics than in the previously analyzed sources. The three galaxies of Nesvadba et al. (2008a) showed large bubbles with regular velocity fields, whereas only about half (17/32) in our present sample with resolved kinematics are dominated by such monotonic large-scale velocity fields, and have ratios of bulk to turbulent velocity that are higher than in the more compact galaxies.

Fifteen galaxies have irregular gas kinematics, which are not very reminiscent of back-to-back outflows. Finding so many sources with large velocity jumps over small areas near our resolution limit of few kpc requires the presence of an energy injection mechanism that is powering the gas kinematics locally and at kpc distance from the AGN itself.

We see little evidence of multiple stellar components associated with regions that are kinematically distinct from each other, as we might expect if these jumps were caused by pre-coalescent major mergers. Sudden localized jumps in velocity and line width are however also fully consistent with the jet

scenario. Off-nucleus gas acceleration associated with radio jets has previously been observed in a number of low-redshift radio galaxies, e.g., IC 5063 (Morganti et al. 2005), 3C 293 (Emonts et al. 2005), and 3C 326 N (Nesvadba et al. 2011a), suggesting that the global complexity we see in our sources could be a general signature of interactions between radio jet and the global interstellar gas of their host galaxy, where the individual properties of each source might lead to a somewhat different phenomenology in each individual galaxy.

Both types of morphologies have also been found in hydrodynamic models of radio jet cocoons expanding through ambient gas. Sutherland & Bicknell (2007), Wagner & Bicknell (2011), and Wagner et al. (2012) modeled the jet expansion through turbulent, inhomogeneous media, finding that the jet experiences a first phase of very efficient momentum and energy deposition as it expands along low-density channels through the ambient gas disk. Only after breaking out of this disk and into the more uniform, lower-density intergalactic or intracluster medium at the end of this flood and channel phase do well collimated radio jets form. Irregular gas morphologies with multiple small bubbles, and sudden jumps in velocity or line widths can be expected during this phase, and would at least qualitatively correspond to the irregular morphologies that we see in many sources. This includes not only irregular velocity fields, but also irregular distributions of line widths, because it is not a priori clear if these jumps are due to enhanced random motion or turbulence in small regions of our galaxies, or bulk (out-)flows. Prime examples for this phase might in particular be 3C 257 and MRC 0251–273, where the jets are not only embedded within the bright emission-line region, but also misaligned with the major axis of the gas.

After breaking out of the disk (or when disrupting it), the cocoon inflated by the radio jet may entrain and accelerate clouds of ambient gas, which are lifted off the disk, fragment under the

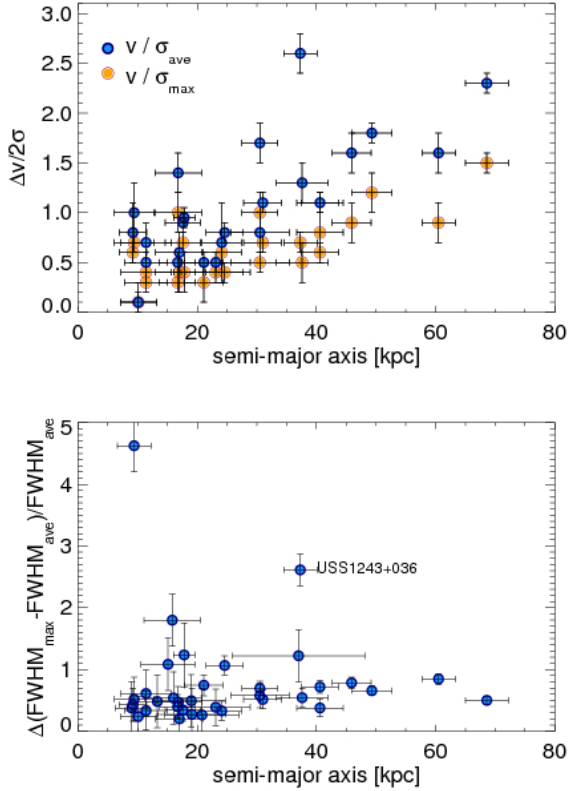


Fig. 12. The ratio of bulk to turbulent velocity (parametrized as $\Delta v / 2\sigma$, see §7.5) in the 25 sources with extended gas in Table 4 scales with the size of the emission-line region (top panel). We plot $\Delta v / 2$ instead of Δv , because this gives an approximation to the circular velocity in case of rotationally dominated motion. The offset between maximal and average FWHM does however not depend on the source size (bottom panel).

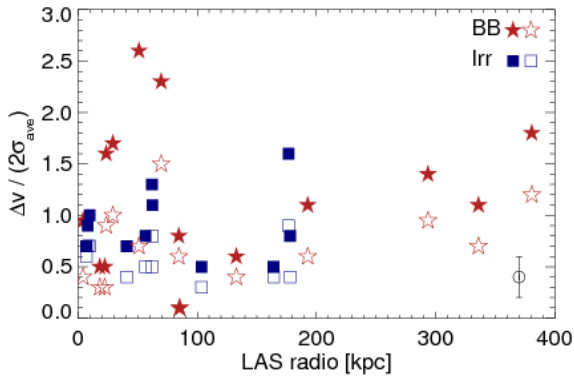


Fig. 13. Ratio of ordered to unordered motion, $\Delta v / \sigma$, as a function of radio size. We show all 25 sources from Fig. 4 with measurements of $\Delta v / \sigma$. Filled and empty symbols show the maximal and average line widths, respectively.

influence of Kelvin-Helmholtz instabilities due to the velocity offset between the cloud and hot wind medium, and form extended filaments of warm ionized gas over several tens of kpc from the central galaxies (Cooper et al. 2008; Scannapieco & Brüggén 2015). An example where sudden jumps in velocity and line width are directly associated with radio hot spots, suggest-

ing that gas is being dragged out of the galaxy as the radio jet is breaking out of the ISM, is MG 2308+0336 (§A.33). These simulations also suggest that the global appearance of this gas preserves the signatures of the initial gas distribution, i.e., small clumps and filaments of material from a massive gas disk may be distributed over the entire volume of the hot wind bubble as suggested by several of our sources (e.g., MRC 0156–252 or USS 1243+036). Alternatively, it may accumulate along the edges of the bubble, e.g., if backflow from the working surface of the jet determines the gas kinematics. This would broadly correspond to the hourglass-shaped morphology of sources like MRC 0156–252 (Gaibler et al. 2009), or may produce a radio morphology that is very asymmetric (Gaibler et al. 2011).

In the following subsections we will more closely examine the kinematic properties of the gas and the radio jets, to infer whether we can find more quantitative evidence for this scenario from the global properties of the gas, and regardless of the detailed properties of each individual galaxy. We start by demonstrating that disk rotation does not match the kinematic properties of the gas in our sources overall. A complete analysis would also require to compare with the star formation and bolometric AGN properties of our sources. For about 20 sources, which are also part of the Hergé sample of HzRGs with Herschel/SPIRE and PACS far-infrared photometry, we are able to do such a comparison, finding that the radio jet is the most important source of the energy and momentum in the gas. We discuss this further in a companion paper (Nesvadba et al. 2016, in prep.).

7.1. Kinematic signatures of rotation?

The ratios of bulk to random motion, v / σ , provide information about whether the gas kinematics in our sources might be dominated by rotation. The light profiles of many HzRGs can be fitted with de Vaucouleur’s profiles (van Breugel et al. 1998; Pentericci et al. 2001; Targett et al. 2011), so that the comparison with early-type galaxies seems to be warranted. Martig et al. (2009) argued that the gas kinematics in gas-rich early-type galaxies should reflect the stellar kinematics of the host galaxy, which is why we compare the gas kinematics in our galaxies with that of the stars in nearby ‘fast rotating’ early-type galaxies from the ATLAS^{3D} survey (Emsellem et al. 2011).

In Fig. 14 we show the ratio of bulk velocity to velocity dispersion as a function of the ellipticity ϵ of the emission-line region, i.e., $\epsilon = 1 - D_{\text{min}} / D_{\text{max}}$, where D_{min} and D_{max} are the size of the emission line gas along the minor and major axis, respectively. The figure shows all 25 galaxies with emission-line regions that are spatially resolved along the major and minor axis. The dotted region shows the upper and lower envelope of fast rotators by Emsellem et al. (2011) in the ATLAS^{3D} survey, the red line the upper limit of the region occupied by slow rotators. Galaxies falling into this dotted region are within a characteristic range of inclination, intrinsic ellipticity, velocity dispersion and rotational velocity which are typical for fast rotators. Most of our galaxies fall above the region of this diagram spanned by the low-redshift galaxies. The bulk velocities of our sources are therefore higher than what would be expected from gravitational motion within an early-type galaxy, in spite of the unusually broad line widths. This holds generally for a given combination of line width, ellipticity, and inclination, although we cannot reliably determine each of these parameters individually from our data. Finding ratios of bulk velocities to line widths that are greater than expected for gravitational motion is also at odds with a scenario of disk rotation with additional line broadening caused by local interactions between jet and gas. We note that

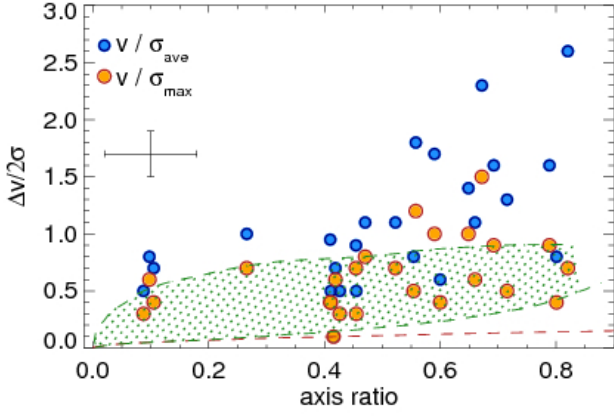


Fig. 14. Ratio of bulk velocity to dispersion as a function of the ellipticity, i.e., $1 - D_{\min}/D_{\max}$, where D_{\min} and D_{\max} are the size of the emission line gas along the minor and major axis, respectively. We show all 25 galaxies with emission line regions that are resolved along the major and minor axis, and have well defined ratios of v/σ . The green dotted area shows the region occupied by the fast rotators in the ATLAS^{3D} survey (Emsellem et al. 2011). The red line delimits the range in parameter space for slow rotators. See Emsellem et al. (2011) for details of the physical properties of these two regions.

this conclusion depends on two assumptions: Firstly, that our sources have similar structural properties to those of van Breugel et al. (1998); Pentericci et al. (2001), and Targett et al. (2011), with which we have 15 sources in common. Secondly: That the structural properties of our HzRGs are not different by more than a factor 2-4 from those of low-redshift galaxies. We consider this a reasonable assumption, because, e.g., observations of the fundamental plane out to $z=1-2$ seem to imply much smaller offsets, once passive luminosity evolution has been taken into account (e.g., van de Sande et al. 2014; Zahid et al. 2015)

We do obtain a better match when using the maximal line widths instead. These widths, however, are only found in small areas of the emission-line gas, and are significantly higher than those expected for galaxies with masses of few $10^{11} M_{\odot}$ of $\sigma = 200 - 300 \text{ km s}^{-1}$ and observed in equally massive galaxies at $z \sim 1.5$ (Buitrago et al. 2014).

7.2. Time scales

Alexander & Leahy (1987) and Best et al. (1995) estimated typical jet advance speeds of powerful FR II radio galaxies from the 3 CR of $v_{\text{jet}} = 0.01 - 0.1c$, where c is the speed of light. Assuming that the jets in our sources have expanded at uniform speed throughout their lifetime, we can use the radio sizes to infer typical age ranges for our sources. This suggests typical ages of few 10^{6-7} yrs and 10^{5-6} yrs for $v_{\text{jet}} = 0.01 c$ and $v_{\text{jet}} = 0.1 c$, respectively. Given that the breakout of the radio jet from extended reservoirs of relatively dense gas is likely to last already about 10^6 yrs (Wagner et al. 2012), it is likely that in particular the lowest ages are underestimates. In the following we will adopt a typical age range of 10^{6-7} yrs. If the jet is the origin of the gas kinematics, then jet expansion speeds much lower than $0.01 c$ (and thus ages much longer than few 10^{6-7} yrs) are ruled out by the high gas velocities of few 1000 km s^{-1} we find in some of our sources.

7.3. Kinetic jet power

Only a small fraction of the kinetic energy of the relativistic particle content of radio jets is emitted in form of synchrotron radiation in the centimeter radio regime (e.g., Heckman & Best 2014, and references therein). The ratio of integrated radio luminosity to jet kinetic power is about 0.1%, however the detailed outcome for each source depends on the local magnetic field and the density of the surrounding medium. This makes it relatively challenging to estimate the kinetic power of a radio jet from the observed radio luminosity. Several empirical methods have been proposed in the literature to measure this relationship between observed jet power in the centimeter regime and the intrinsic kinetic power of the synchrotron electrons. For the purpose of this work, we use the estimates of Cavagnolo et al. (2010) and Willott et al. (1999).

Cavagnolo et al. (2010) use the mechanical energy required to inflate cavities in the X-ray halos of massive low-redshift galaxy clusters to infer the kinetic power of the radio source. They give a calibration to estimate the kinetic power, $dE/dt_{\text{kin,jet,C10}}$ based on the measured monochromatic radio power at 1.4 GHz in the rest-frame,

$$dE/dt_{\text{kin,jet,C10}} = 0.75 \times (L_{1400} - 23.8539) + 1.91, \quad (3)$$

where $dE/dt_{\text{kin,jet,C10}}$ is given in units of $10^{42} \text{ erg s}^{-1}$, and L_{1400} , the observed luminosity of the radio jet at 1400 MHz, in W Hz^{-1} .

Willott et al. (1999) calibrate their observations against the rest-frame 151 MHz radio luminosity, L_{151} , by setting

$$dE/dt_{\text{kin,jet,W00}} = 3 \times 10^{38} f_c^{3/2} L_{151}^{6/7}, \quad (4)$$

where f_c is a proportionality factor, which is most likely around $f_c = 10$ (Cattaneo et al. 2009).

For both estimates we need to estimate the radio power at the required rest-frame frequency. We do this by interpolating along the best linear fit of multifrequency observations of our sources as given in NED. The 1.4 GHz measurements correspond to 300-400 MHz of observed frequency for most of our sources, and are approximately matched by the frequency range of surveys like the Texas survey at 365 MHz or the Molonglo survey at 408 MHz (Large et al. 1981). The 151 MHz flux required for the Willott et al. (1999) estimate would correspond to observed radio fluxes at 32-50 MHz, which is lower than the lowest-frequency measurements that are readily available for large samples in the south (80 MHz; Slee 1995).

In Table 3 we list the radio luminosities at both rest-frame frequencies, and the mechanical energy output rates derived with the Willott et al. (1999) and Cavagnolo et al. (2010) approach, respectively. Fig. 15 shows the scatter plot of both estimates. It is reassuring that both lead to similar estimates within a factor 2 for most sources (0.3 dex, dashed lines in Fig. 15). Sources with larger discrepancies have relatively shallow spectral indices compared to the generally steep radio spectral indices of high-redshift galaxies of $\alpha \leq -0.8$ to -1.0 . Since we have no direct observational constraints about a possible steepening of these indices towards lower radio frequencies, we favor the Cavagnolo et al. (2010) estimates for these sources. Fig. 16 demonstrates that our sources sample the overall range in jet kinetic energy fairly evenly at all radio sizes.

A common worry in estimating kinetic jet powers is that we have to extrapolate from the observed GHz regime well into the observed or even rest-frame MHz regime. For example, recent LOFAR observations of two nearby FR II radio galaxies show a

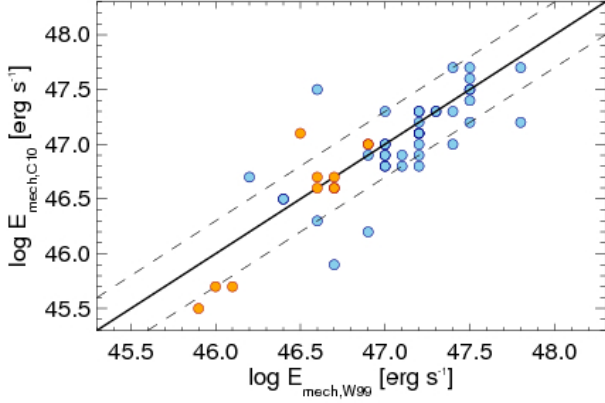


Fig. 15. Mechanical energy estimates obtained with the formalism of Willott et al. (1999) and Cavagnolo et al. (2010) are shown along the abscissa and ordinate, respectively. The solid line shows the line of equality between both estimates, dashed lines offsets by 0.3 dex (a factor of 2). The light blue and orange symbols show the sources of the present sample and that of Collet et al. (2015b), respectively.

steepening of the spectral index at frequencies between about 10 and 1000 MHz, which translates into underestimates of about a factor 5 in kinetic jet power (Harwood et al. 2016). On the bright side, these measurements give us also the opportunity to investigate the systematic uncertainties of our estimates of kinetic jet power directly.

We use the energy density estimates of Harwood et al. (2016) of $1.2 \times 10^{-12} \text{ J m}^3$ in 3C 452, and of $0.28 \times 10^{-12} \text{ J m}^3$ and $0.32 \times 10^{-12} \text{ J m}^3$ in the northern and southern lobe of 3C 223, respectively, and their measured radio sizes, $289.2'' \times 89''$, and $157.5'' \times 21.5''$, and $152'' \times 25.8''$ for 3C 452 and 3C 223, respectively, to estimate a total energy content of $2.3 \times 10^{60} \text{ erg}$ and $1.8 \times 10^{60} \text{ erg}$ in 3C 452 and 3C 223, respectively. We then use their projected sizes to estimate a jet age for a fiducial expansion velocity of $0.1 c$, finding 14 Myrs and 12 Myrs for 3C 452 and 3C 223, respectively. This corresponds to kinetic energy injection rates of 5.0 and $4.6 \times 10^{45} \text{ erg s}^{-1}$, respectively. We then use integrated radio flux measurements from NED between 1.4 GHz and 10 GHz for the two galaxies to estimate a rest-frame 1.4 GHz jet power in the same way and for a similar frequency range to our targets, which have measurements down to observed frequencies of about 70 MHz. We find 26.3 W Hz^{-1} and 26.1 W Hz^{-1} for 3C 452 and 3C 223, respectively, and spectral indices of -1.3 and -0.8 , respectively, not very different from our less powerful sources. With the Cavagnolo et al. (2010) approach, this corresponds to 4 and $5 \times 10^{45} \text{ erg s}^{-1}$ for 3C 452 and 3C 223, respectively, comparable to the rates implied by the results of Harwood et al. (2016). This shows that, although our method is still very approximate, systematic uncertainties in our estimates of jet power are of comparable amplitude as other uncertainties.

7.4. Velocity range and estimates from feedback models

The expansion velocity of the cocoon is one of the prime quantities predicted by hydrodynamic models of jets expanding through the ambient gas, and it is therefore very interesting to compare the range of velocities we observe with expectations from models. A similar velocity range of warm ionized gas clouds can also be expected from the models of Gaibler et al.

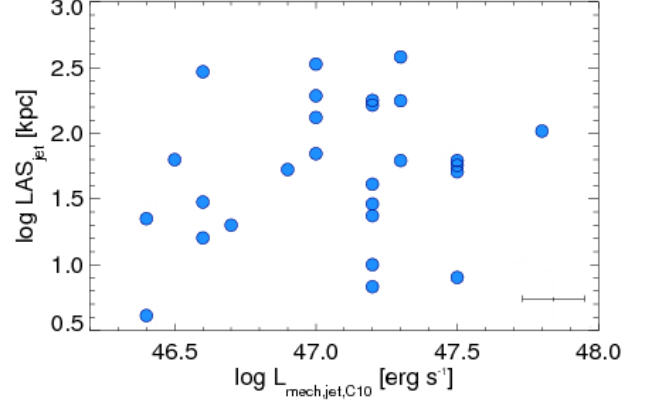


Fig. 16. Largest angular size of the radio source as a function of the jet mechanical energy estimated with the formalism of Cavagnolo et al. (2010). We show all 49 sources with SINFONI data.

(2009), who find an expansion velocity $\sim 5000 \text{ km s}^{-1}$ of the cocoon. We follow Cooper et al. (2008) in parametrizing the acceleration that a dense cloud experiences through the drag by a hot wind medium as, $f_{\text{th}} = 3/9C_D(\rho_w/\rho_c)v_w^2/R_C$, where f_{th} is the acceleration, C_D the drag coefficient, $n_c = 500 \text{ cm}^{-3}$ the gas density in the filaments, R_C the size of a cloud, ρ_w and ρ_c the density in the wind and cloud, respectively, and v_w the wind velocity. We find accelerations of about $1 \times 10^{-12} \text{ km s}^{-2}$, and velocities of $300\text{--}700 \text{ km s}^{-1}$ for cloud sizes between 5 and 10 pc.

In Fig. 17 we compare the velocity range observed in our targets with the predictions of Wagner et al. (2012) for jet interactions with clumpy, turbulent gas. We plot two samples, the one presented here, and the one of Collet et al. (2015b) of radio galaxies with somewhat lower radio power. The FWHMs of our sources fall into the velocity range predicted by the model for galaxies with similar radio power, and Eddington ratios of 10^{-1} to 10^{-2} (left panel of Fig. 17), whereas the velocity offsets correspond to lower velocities and higher Eddington ratios, and fall off more quickly with increasing radio power than the line widths. We caution that these Eddington ratios are between the kinetic jet power in this case (and not the radiative AGN luminosity, as is more frequently the case) and the Eddington luminosity of the central supermassive black hole. For six galaxies (marked as red stars in Fig. 17) we have Eddington luminosities measured in Nesvadba et al. (2011b, their Table 2) and Collet et al. (2015b). Using the jet kinetic energies listed in Table 3 and line FWHMs, we find Eddington ratios between 0.4 and 0.1 for all targets, factors of a few higher than expected from the models. For bulk velocities, we find Eddington ratios around 1 or even higher. This suggests that discrepancies between observations and model expectations do persist, although the good correspondence in the predicted velocity range is very encouraging, even more so as observational effects like blurring of localized outflows with surrounding material and projection effects might in part be the cause. Another potential source of such discrepancies could however also be the longer-term evolution of the gas. As Wagner et al. (2012) point out, studying the evolution of clumpy, turbulent, and multiphase gas over time scales longer than few 10^5 yrs at high resolution is still computationally very demanding, and most of our nebulae have dynamical times that are about $10 \times$ longer (Table 5).

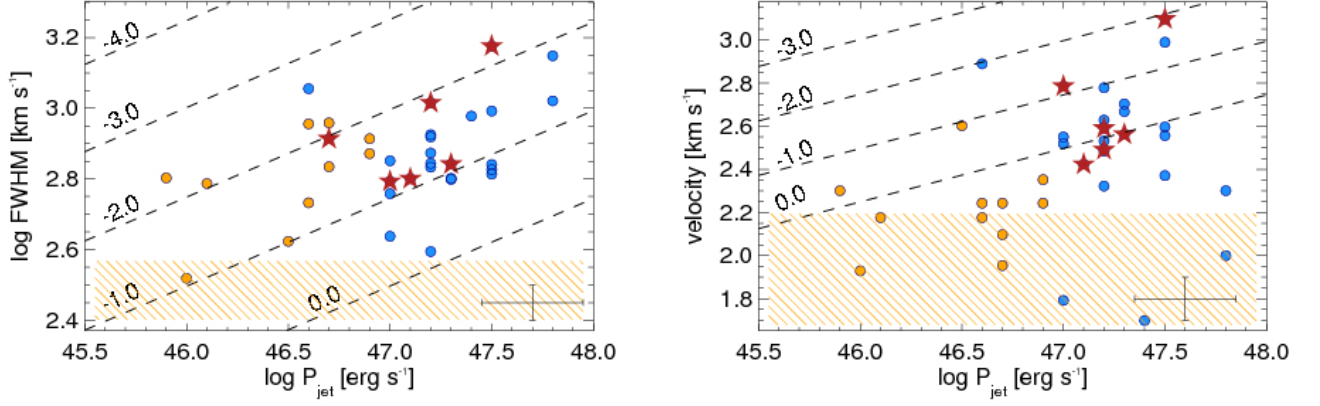


Fig. 17. Gas velocity as a function of the jet power following Wagner et al. (2012). The left panel shows FWHM line widths, the right panel approximates a putative radial outflow velocity by showing one half of the measured velocity offsets. Blue and orange symbols show the radio galaxies of the present analysis, and those of Collet et al. (2015b), respectively. Red stars show galaxies with measured Eddington ratios from Nesvadba et al. (2011b). The black dashed lines show jet powers corresponding to Eddington ratios between 10^{-4} and unity. The yellow hatched area shows the range spanned by the mass selected sample of galaxies without prominent radio source of Buitrago et al. (2014).

7.5. Gas kinetic energy and momentum and transfer efficiencies from the jet to the gas

Characterizing the kinematics of the gas in the complex emission-line regions of HzRGs, with their wide ranges of line width and velocity jumps, with a single (or a small set of) numbers is very challenging. In addition to the complex intrinsic kinematics, blurring by the seeing disk and projection effects are likely to play a role. In spite of these difficulties, we have seen in §6.2 that it is possible to identify global trends between radio power and gas kinematics, even when characterizing the complex kinematic properties of these galaxies only with a single number.

This encourages us to derive global estimates of the kinetic energy and momentum in our sources using simple analytical expressions previously established within the spherical blastwave scenario of supersonic shocks in the context of supernova explosions. Models of radio jet cocoons have shown that the global energetics of the extended gas in HzRGs are not too different from those obtained with a spherical blastwave model, where the hot cocoon entrains ambient gas as it expands through the ISM of the galaxy at highly supersonic speed (e.g., Krause 2003; Wagner et al. 2012). The blastwave approximation seems to be justified in these models irrespective of the detailed gas properties or the evolutionary state of the jet. This is perhaps most surprising for very irregular, clumpy environments, where the jet does not simply expand near-adiabatically through the ambient gas (Wagner & Bicknell 2011; Wagner et al. 2012).

We adopt the same simple approach as in our previous analyses (in particular Nesvadba et al. 2006a) to estimate the kinetic energy injection rate into the gas with the following equations appropriate for blastwaves (e.g., Dyson & Williams 1980). Firstly, we set

$$dE/dt = (\Delta v/435)^5 n_0^{-1} \times 10^{44} \text{ erg s}^{-1}, \quad (5)$$

where Δv is the expansion velocity of the bubble, and n_0 the density of the ambient gas (i.e., outside the expanding bubble).

Secondly, we can derive an energy injection rate by considering that the hot gas bubble expands adiabatically, and assuming

that the highest observed gas velocities approximate the expansion velocity of the bubble:

$$dE/dt = 1.5 \times 10^{46} \times r^2 \times \Delta v^3 \times n_0 \text{ erg s}^{-1}, \quad (6)$$

where r is the radius of the bubble in units of 10 kpc. In both equations, Δv is given in units of 1000 km s⁻¹.

In Fig. 18 we compare the kinetic energy distribution of our sources estimated by the two approaches (and using observed quantities further discussed below), finding a good correspondence between the two. The slope of the best linear fit, 0.78, is slightly below unity, but mostly driven by the source with the highest and lowest energy estimate, which have offsets from the one-to-one relationship that are consistent with the overall scatter within the sample, and we therefore consider this result consistent with a one-to-one relationship. Finding a good correspondence between both estimates implies that the gas velocities and sizes are consistent with each assumption, and therefore further demonstrates that the blastwave scenario is a reasonable approximation.

In addition to the energy, the radio jet also injects momentum into the gas. We estimate the momentum injection rates associated with each estimate, dP/dt , by setting $dP/dt = 1/v \, dE/dt$.

The next question to address is, which quantity we should use as velocity estimate. Velocity offsets are perhaps the most obvious quantity, but also interpretationally difficult: Firstly, in galaxies with relatively small total velocity offsets (≤ 400 – 500 km s⁻¹) and gas sizes less than about 10–20 kpc, the kinematics may reflect the radial motion of an outflow, perhaps in combination with disk rotation, whereas our results in §7.1 disfavor rotation alone. In back-to-back outflows, gas in either bubble is driven out at 1/2 the total velocity offset. In winds lifted off a disk, the observed velocity offset corresponds to the relative velocity between disk and wind. In both cases, intrinsic velocities may be factors 2–3 larger than those observed because of beam-smearing and projection effects. We have previously discussed these interpretational complications in more detail in Nesvadba et al. (2008a) and Collet et al. (2015b), and use 1/2 of the total velocity offset in our calculations here, which gives the more conservative energy estimates. With all these caveats, and using Equations 5 and 6, we find kinetic energy injection rates from

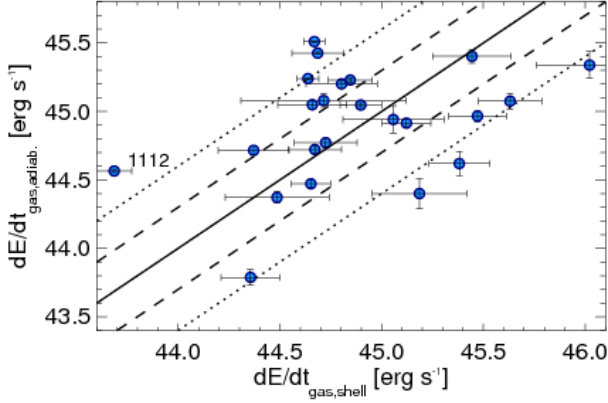


Fig. 18. Comparison of the results of our two kinetic energy estimates in §7.5 for the 23 galaxies with extended emission line regions, which have been observed in [OIII] λ 5007. The dashed and dotted lines show offsets by factors 2 and 4, respectively, from the one-to-one relationship (solid line).

bulk motion that are between few 10^{43} and 1×10^{47} erg s $^{-1}$. Corresponding momentum injection rates are between 10^{34} and 10^{39} dyn.

Fig. 11 showed that amongst our different measures of FWHM (average and maximal velocity dispersion and integrated line widths, see also Table 4), the average velocity dispersions are most tightly related to the jet power. We therefore consider the average widths the most reliable tracers of gas motion related to the radio jet, on which we base our estimates of kinetic energy from random motion. With the two equations presented above, we estimate kinetic energy injection rates between 0.6×10^{44} erg s $^{-1}$ and 1×10^{46} erg s $^{-1}$ in our sample, most galaxies have between 5 and 10×10^{44} erg s $^{-1}$. Results for individual galaxies are listed in Table 5.

Another interesting quantity to characterize feedback from radio jets onto the surrounding gas is the efficiency with which the jet kinetic energy is being deposited into the gas, i.e., the ratio $E_{\text{kin,gas}}/E_{\text{kin,jet}}$. In Fig. 19 we show how the kinetic energy injection rates estimated from resolved bulk motion, from the line widths, and the sum of both, respectively, scale with kinetic jet power. Efficiencies are between 10^{-3} and almost unity in all cases, with most galaxies falling around 10^{-2} . No galaxy has an efficiency greater unity, implying that we do not require a contribution from another mechanism driving the gas based on these observations and analysis. The scatter is very large, as can be expected given the considerable uncertainties in the estimates of this relationship, and may therefore not preclude a much tighter intrinsic relationship between jet and gas energy. Considering the combined sample of the sources from the present study and those of Collet et al. (2015b), uncorrelated distributions are ruled out at significances of few times 10^{-4} and better for energy injection rates derived from bulk kinetic motion, line widths, and the sum of both. The hydrodynamic models of Wagner et al. (2012) predict efficiencies of up to 40%, about an order of magnitude greater than what we observe. It is well possible that parts of these discrepancies come from heating and entrainment of gas in other phases of cold gas (e.g., Nesvadba et al. 2010; Emonts et al. 2015).

We did not find a relationship between efficiency and jet size. Gas kinetic energies estimated with the two methods are uncorrelated with radio size at significances between 0.16 and >0.5

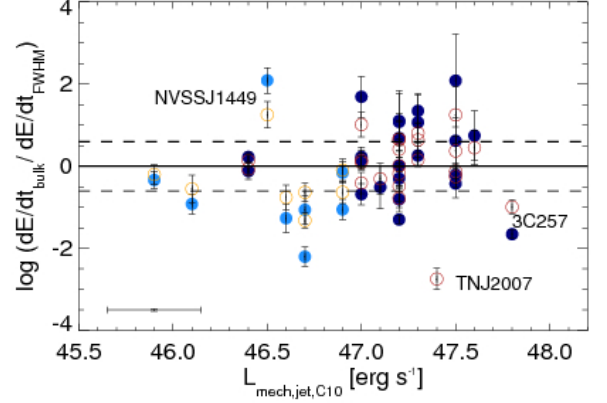


Fig. 20. Ratio of kinetic energy estimated from the velocity offsets and line widths, respectively, as a function of kinetic jet power. Filled dark blue and empty red circles show ratios derived with Eqn 5 and 6 for 23 galaxies with extended emission-line regions in the present sample, respectively. We excluded RC 0311+0507 for which we only have [OII] $\lambda\lambda$ 3727,3729 with a composite line profile, unlike the other sources in our sample. Filled light blue dots and yellow open circles show the same estimates for nine galaxies with extended emission-line regions discussed in Collet et al. (2015b), which have significantly lower radio power. The solid line shows the one-to-one relationship, dashed lines factors 4 above or below, which corresponds to twice the typical uncertainty expected from inclination and resolution effects.

with the Spearman rank test and Kendall's τ . This result is interesting, but it would be very naive to conclude that the jet deposits its mechanical energy at uniform rates throughout its expansion history. Quite to the contrary, it is reasonable to expect that the efficiency of this energy deposition drops markedly once the jet has broken out of the ambient gas. An alternative interpretation is that the gas dissipates the kinetic energy only relatively slowly compared to the lifetime of the radio jet. We will further discuss this in §8.

8. Role for galaxy evolution

8.1. Outflows and turbulence

The 'standard' scenario of AGN feedback adopted by most observers and cosmological models focuses on the gas removal through winds driven by the AGN through its radiation or the radio jets. In these models, star formation in galaxies is truncated by starvation as the gas reservoirs that would otherwise fuel subsequent star formation are being depleted by the wind. In contrast, several observations of radio galaxies in the more nearby Universe have shown in recent years that the kinetic energy injection of radio jets feeds a complex interplay between turbulence within the gas of the disk and outflows that are lifting gas above the disk, and which may or may not escape (e.g., Nesvadba et al. 2010, 2011a; Alatalo et al. 2011). These galaxies are characterized by small ratios of v/σ , akin to those in our galaxies, large gas masses (mostly in diffuse, filamentary, warm molecular gas at low- z), and shock-like line ratios in large gas fractions. The energy carried by the wind appears roughly as large in these galaxies as that which is driving the turbulence. A central characteristic of these galaxies are their strongly enhanced luminosities of warm ($T > 100$ K) H $_2$ emission lines

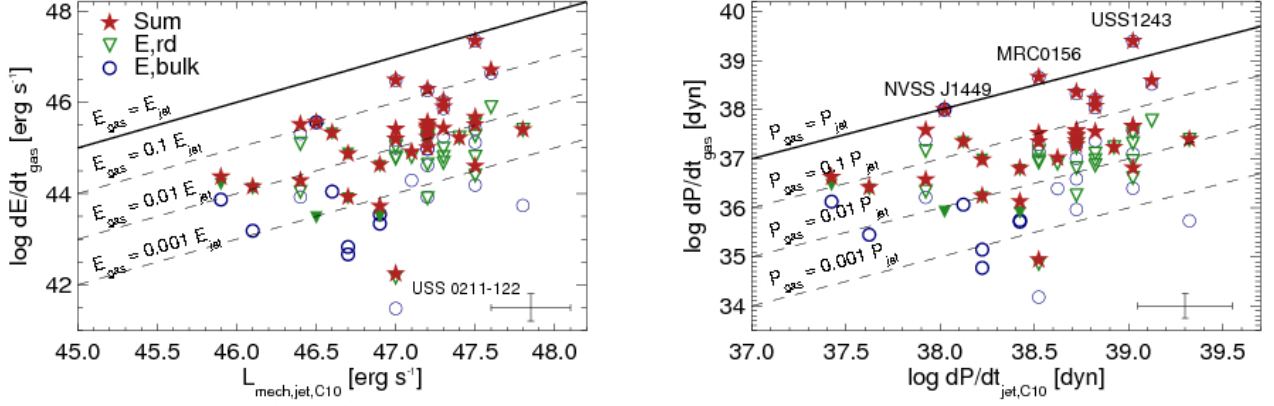


Fig. 19. (*left*) Kinetic energy injection rates from resolved bulk motion (dark blue open circles) and unordered motion (upside-down green triangles), and the sum of both (red stars), as a function of radio power. The solid line shows the kinetic power of the radio jet, and dashed lines show ratios of 10^{-1} , 10^{-2} , and 10^{-3} . (*right*) The same plot showing the momentum injection rates of the radio source and the gas.

in the mid-infrared, exceeding expected luminosities from UV heating by factors of at least a few (Ogle et al. 2010; Nesvadba et al. 2010). The only HzRG with an observation of warm mid-IR H_2 emission in the literature is currently MRC 1138–262 (Ogle et al. 2012), the first galaxy we also observed as part of our SINFONI survey. Turbulence and winds could be closely related in these galaxies. Scannapieco (2013) point out that turbulence in the clumpy ISM of starburst galaxies could strongly heat small parcels of gas, thereby enhancing the efficiency of mass loading of the hot wind medium with ambient gas, and playing an important role in launching collimated winds.

The most direct observable of turbulence in high-redshift galaxies before more mid-IR spectroscopy of HzRGs will become available with the James-Webb Space Telescope are their broad line widths. It is therefore very interesting that the emission lines in HzRGs, including MRC 1138–262, reach very large, and almost constant, values of about $500 - 800 \text{ km s}^{-1}$ over several orders of magnitude in radio power (see also Collet et al. 2015b). The ratios of bulk to random motion, $v/2\sigma$, are as low as $v/2\sigma = 0.3 - 0.4$ in several of our sources (Table 4). This implies that these are not self-gravitating disks, although at least some of the gas may still be bound within the gravitational potential of the galaxy. The large line widths imply that at least parts of this gas along the line wings also exceed the escape velocity of their host galaxy (about $500 - 700 \text{ km s}^{-1}$, e.g., Nesvadba et al. 2006b).

To further investigate the role of turbulence and bulk velocity, we can investigate how each depends on other properties of our sources. In §6.3 we showed that the ratios of $v/2\sigma$ do scale with increasing size of the emission-line regions (or elongation, Fig. 14), but not with the size of the radio source (Fig. 13). It is also very interesting to compare how the kinetic energy in bulk and random motion scale with radio power. In Fig. 20 we plot the ratio of the kinetic energy injection rates into the gas estimated from the Gaussian line widths ($\sigma = \text{FWHM}/2.355$) and those derived from $\Delta v/2$ as a function of radio power. At all values along the abscissa we note a subset of sources which have much lower energy injection rates from ordered than unordered motion, although both forms of energy injection increase roughly at the same rate with radio power. Galaxies with large ratios of ordered to unordered motion seem to be generally associated with radio sources with kinetic power greater than about

$10^{47} \text{ erg s}^{-1}$. This corresponds to gas kinetic energy injection rates greater than about $10^{44-45} \text{ erg s}^{-1}$. The only exception is NVSS J144932–385657, which is the largest source in the sample of Collet et al. (2015b), which has a radio power of $2.5 \times 10^{46} \text{ erg s}^{-1}$ with the estimate of Cavagnolo et al. (2010), but 1.3×10^{47} with the estimate of Willott et al. 1999). This discontinuity is a new effect which could only be discovered observationally with a large sample such as ours, and which has to our knowledge not been anticipated in hydrodynamic simulations or observations of other types of AGN, and deserves a more detailed discussion.

Fig. 20 shows the presence of sources dominated by kinetic energy in unordered motion at all jet power. At a jet power above $10^{47} \text{ erg s}^{-1}$, however, the number of sources dominated by their bulk outflow energy becomes significant. It is possible that this discontinuity marks a threshold at which the momentum injection into the ambient gas becomes so strong that the disk no longer remains globally stable. In the most powerful sources, the disk gas would become overall unbound. At energies below this threshold, more localized outflows may exist in an overall turbulent disk, which may closely co-exist with the jet cocoon as previously discussed by Nesvadba et al. (2010, 2011a), and Collet et al. (2015b). This could also explain why outflows in low-redshift radio galaxies, which do not reach such high jet power, appear typically to be more localized, very different from the extended bubbles in the most powerful high-redshift galaxies.

We are not aware of a hydrodynamic simulation that would show such an effect for powerful AGN hosts, but we can build upon a very recent analytical approach to study in a more quantitative way how turbulence and outflows may depend on each other in these HzRGs. Based upon the notion by Thompson & Krumholz (2016) that turbulence might cause super-Eddington winds in sub-Eddington starbursts, Hayward & Hopkins (2015) presented an analytic model of feedback which includes outflows as well as turbulence. Turbulence creates a multi-phase environment, where cells of gas with different velocity, density, temperature, and phase co-exist. A given momentum injection rate might already be sufficient to remove gas from comparably low-density cells, even though the momentum injection rate is not sufficient to remove average-density gas.

Source	age [10^7 yrs]	$\log E_{\text{gas,FWHM},1}$	$\log E_{\text{gas,FWHM},2}$	$\log E_{\text{gas},\Delta v,1}$	$E_{\text{gas},\Delta v,2}$
BRL 0128-264	1.5	44.6 ± 0.2	45.2 ± 0.2	45.3 ± 0.2	45.7 ± 0.2
MRC 0156-252	12.0	44.9 ± 0.2	45.6 ± 0.2	46.6 ± 0.2	46.6 ± 0.2
MRC 0251-273	4.1	44.0 ± 0.2	44.7 ± 0.2	44.7 ± 0.2	45.1 ± 0.2
MP J0340-6507	3.0	44.4 ± 0.3	45.1 ± 0.2	43.1 ± 0.2	44.3 ± 0.2
PKS 0529-549	3.3	43.6 ± 0.2	44.3 ± 0.2	43.4 ± 0.2	44.2 ± 0.2
TXS 1113-178	1.3	43.4 ± 0.2	44.1 ± 0.2	42.9 ± 0.2	43.8 ± 0.2
3C 257	2.0	44.2 ± 0.2	44.9 ± 0.2	42.6 ± 0.2	43.9 ± 0.2
USS 1243+036	4.9	44.7 ± 0.5	45.4 ± 0.2	46.8 ± 0.2	46.7 ± 0.2
USS 1410-001	6.0	44.7 ± 0.2	45.4 ± 0.2	44.8 ± 0.2	45.4 ± 0.2
MRC 1558-003	6.1	44.6 ± 0.2	45.3 ± 0.2	44.9 ± 0.2	45.5 ± 0.2
USS 1707+105	3.1	44.4 ± 0.2	45.1 ± 0.2	44.1 ± 0.2	45.0 ± 0.2
3C 362	3.4	44.8 ± 0.3	$45. \pm 0.2$	44.4 ± 0.2	45.2 ± 0.2
MP 1758-6738	5.1	44.3 ± 0.2	45.0 ± 0.2	44.5 ± 0.2	45.1 ± 0.2
MRC 2025-218	1.2	44.0 ± 0.2	44.6 ± 0.2	43.1 ± 0.2	44.2 ± 0.2
MG 2037-0011	<1.0	43.8 ± 0.3	44.5 ± 0.2	41.8 ± 0.3	43.3 ± 0.2
MRC 2104-242	10.4	44.8 ± 0.2	45.5 ± 0.2	45.9 ± 0.2	46.1 ± 0.2
4C 23.56	8.9	44.6 ± 0.2	46.3 ± 0.2	45.9 ± 0.2	46.1 ± 0.2
MG 2144+1928	6.2	44.5 ± 0.2	44.1 ± 0.2	45.1 ± 0.2	45.5 ± 0.2
TN J2254+1857	2.9	44.2 ± 0.2	44.9 ± 0.2	44.4 ± 0.2	45.0 ± 0.2
MG 2308+0336	4.1	44.5 ± 0.2	45.2 ± 0.2	45.6 ± 0.2	45.9 ± 0.2
NVSS J0024	2.5	44.3 ± 0.2	45.0 ± 0.2	43.1 ± 0.2	44.3 ± 0.2
NVSS J0040	3.6	43.8 ± 0.2	44.5 ± 0.2	42.7 ± 0.2	43.8 ± 0.2
NVSS J0129	2.4	43.9 ± 0.2	44.5 ± 0.2	41.6 ± 0.2	43.2 ± 0.2
NVSS J0304	3.6	43.1 ± 0.2	43.9 ± 0.2	42.1 ± 0.2	43.2 ± 0.2
NVSS J1449	11.8	43.6 ± 0.2	44.3 ± 0.2	45.7 ± 0.2	45.5 ± 0.2
NVSS J2342	4.6	43.0 ± 0.2	43.6 ± 0.2	42.8 ± 0.2	43.5 ± 0.2
CEN J949	2.8	43.2 ± 0.2	43.9 ± 0.2	42.3 ± 0.2	43.4 ± 0.2
CEN J952	4.9	43.6 ± 0.2	44.2 ± 0.2	43.2 ± 0.2	44.0 ± 0.2
CEN J949	8.7	43.2 ± 0.2	43.9 ± 0.2	42.0 ± 0.2	43.2 ± 0.2

Table 5. Jet ages and kinetic energy of the gas. See text for details.

Hayward & Hopkins (2015) developed their algorithm for self-regulated star formation, however, their basic equations are appropriate for blastwave scenarios generally, and can therefore easily be adapted to our present needs. We will in the following use some of their equations together with our measurements to investigate whether the increased importance of gas outflows compared to turbulence with increasing radio power is consistent with such a scenario.

The most important relationship for our purposes is equation (9) of Hayward & Hopkins (2015), which parametrizes the mass outflow fraction, f_{out} , as

$$f_{\text{out}} = \frac{1}{2} \left[1 - \text{erf} \left(\frac{-2x_{\text{out}} + \sigma_{\ln \Sigma_g}^2}{2\sqrt{2}\sigma_{\ln \Sigma_g}} \right) \right] \quad (7)$$

through the ratio x_{out} between the maximal surface density of gas that can reach escape velocity, Σ_g^{max} , and the average gas mass surface density, $\langle \Sigma_g \rangle$. Σ_g^{max} is set by the momentum injection rate density into the gas, $\dot{\Sigma}_p$, which we take to be in the range observed from the momentum of the warm ionized gas in our galaxies, 10^{35-38} dyn, divided by the surface area of the emission line nebulae (Table 4), the orbital frequency, Ω , and circular velocity, v_c of the galaxy. We adopt $v_c = 350$ km s $^{-1}$ (Nesvadba et al. 2011c), corresponding to the velocity dispersion expected for a galaxy with stellar mass of few $\times 10^{11}$ M_\odot (as measured for HzRGs by Seymour et al. 2007; De Breuck et al. 2010). We calculate the orbital frequency at a radius of 10 kpc, corresponding to the fiducial size of the emission-line nebulae we adopt in these calculations. $\sigma_{\ln \Sigma_g}$ is the width of the density distribution of the gas mass surface density set by the turbulence, $\sigma_{\ln \Sigma_g}^2 \approx 1 + R M^2/4$. Here, M is the Mach number

of the turbulent gas, given by the turbulent velocity dispersion, σ_T , and the sound speed, c_s , $M = \sigma_T/c_s$. R depends on the Mach number and power-law index of the turbulence, α (Hayward & Hopkins 2015). See Hayward & Hopkins (2015) for the detailed derivation of these relationships.

In Fig. 21 we show how the mass outflow fraction depends on the momentum injection rate into the gas, for ranges of characteristic values of velocity dispersion (FWHM=500 km s $^{-1}$, 800 km s $^{-1}$, and 1000 km s $^{-1}$), and sound speed, c_s (11.4 km s $^{-1}$ and 3.7 km s $^{-1}$ for $T = 10^4$ K and $T = 10^3$ K, respectively). $\langle \Sigma_g \rangle$ is the average gas mass surface density over the total column, which we assume to be $D = 10$ kpc, corresponding to the minor axis sizes of the emission-line nebulae. We measured the gas mass surface densities of warm ionized gas in our galaxies, typically few to few times $10 M_\odot \text{ pc}^{-2}$, from the ionized gas mass estimates in §4.4 (see also Table 6) and the projected sizes of [OIII] λ 5007 line emission given in Table 4.

Fig. 21 shows that for galaxies with characteristics that are similar to those in our HzRGs, the fractions of outflowing gas increase rapidly with increasing momentum injection rate in the range that we observe in our galaxies. The black, light blue, and red areas represent gas densities of 1, 10, and $100 M_\odot \text{ pc}^{-2}$, and are each given for three turbulent velocities (which correspond to observed FWHMs of 500 km s $^{-1}$, 800 km s $^{-1}$, and 1000 km s $^{-1}$, respectively). We assume $T = 10^4$ K for all surface mass densities. The solid red histogram in Fig. 21 shows the observed momentum of the warm ionized gas in our galaxies, corresponding to about 1 – 10% of the momentum provided by the radio jet, for a jet expansion speed of $0.1c$ (see also Fig. 19).

The dark blue histogram in Fig. 21 accounts for the additional gas phases that we are likely missing. In turbulent multiphase gas, we would expect that this gas has broadly similar

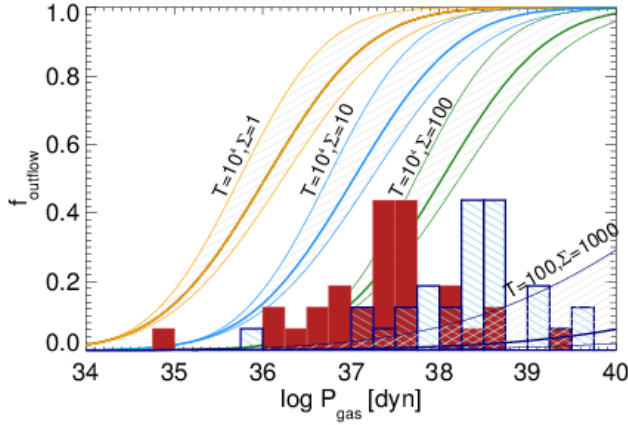


Fig. 21. Fraction of gas with densities below the critical value for outflows as a function of the momentum injection, following Hayward & Hopkins (2015). We show three ranges of mass surface density (orange, light blue, and green hatched regions, respectively) with $\Sigma = 1 \text{ M}_{\odot} \text{ pc}^{-2}$, $10 \text{ M}_{\odot} \text{ pc}^{-2}$, and $100 \text{ M}_{\odot} \text{ pc}^{-2}$, respectively. For each region, the left, central, and right lines represent turbulent velocities that correspond to FWHM=500, 800, and 1000 km s^{-1} , respectively. All are given for temperatures of 10^4 K , corresponding to typical electron temperatures in the warm ionized gas in HzRGs. The red histogram shows the distribution of total gas momentum measured in the galaxies in our sample (Fig. 19). The dark blue region and light blue hatched histogram assume that the total gas content is dominated by molecular and cold neutral gas, with a total gas mass about $10\times$ greater than that of warm ionized gas, $T=1000 \text{ K}$ and $\Sigma = 1000 \text{ M}_{\odot} \text{ pc}^{-2}$.

kinematic properties to the warm ionized gas, as observed in nearby radio galaxies (Nesvadba et al. 2011a), and consistent with the broad line widths of [CI] and even CO observed in HzRGs of about 500-1000 km s^{-1} . From the ratios of ionized to molecular gas mass in Table 6 and other initial estimates of gas masses in other phases in high- z radio galaxies (e.g., warm molecular gas measured from the $\text{H}_2 \text{ 0-0 S(3)}$ line or cold neutral gas measured from atomic carbon, Gullberg et al. 2015, A&A submitted, Ogle et al. 2012), we expect to find that the total gas mass surface density will probably be higher by about an order of magnitude, if taking these gas phases into account. Hence, gas mass surface densities would be in the range $10^2 - 10^3 \text{ M}_{\odot} \text{ pc}^{-2}$, and the momentum about an order of magnitude greater than that of the warm ionized gas alone.

For lower gas temperatures the required momentum injection rates to drive outflows with high mass-loading factors increase rapidly, as seen from the dark-blue rimmed area, which uses $T = 10^3 \text{ K}$, a gas mass surface density of $\Sigma \sim 10^3 \text{ M}_{\odot} \text{ pc}^{-2}$, and otherwise similar parameters to the previous cases. This could imply that molecular outflows in HzRGs are indeed less efficient compared to outflows of warm ionized gas, unless the gas is being heated to temperatures above about 100 K (e.g., through the AGN radiation, cosmic rays, or shocks).

We note that these outflow rates are given relative to the total density distribution of the gas, and concern only gas that can be accelerated during one turbulent crossing time, $t \sim l_{\text{Eddy}}/\sigma_T$. Assuming that turbulence is injected on kpc scales, this corresponds to about $1 \times 10^6 \text{ yrs}$, leaving time for repeated cycles, if the AGN lifetime is long enough. Even outflow rates of few 10%

of the total gas mass could therefore effectively drain the ISM of our HzRGs during an AGN life time.

Of course, all these estimates are highly simplified, and detailed hydrodynamic simulations would be necessary to obtain firm quantitative estimates of how turbulence may boost the efficiency of AGN-driven winds. Nonetheless, our simple calculations show that such a scenario could plausibly explain the increasing importance of galaxy-wide outflows at the highest jet energies. We emphasize that in the scenario adopted here, the molecular and warm ionized gas do not represent two strictly isolated entities, but are part of a multiphase medium, where the local density and temperature fluctuations are large enough that gas might change its phase. This might almost be a prerequisite in our case, and help explain the large numbers of recombining photons we see from the warm ionized gas. With a recombination cross section of few 10^{-14} s^{-1} (Osterbrock 1989), and electron densities between 10^2 and 10^3 , the recombination time of $\text{H}\alpha$, $\tau_{\text{rec}} = 1/n \alpha$, is very short compared to the lifetime of the radio jet, about 10^{3-4} yrs . Here, n is the electron density, and α the recombination cross section. This would imply implausibly large reservoirs of gas that is cooling down, of-order 10^{2-3} times greater than the observed HII masses, or about $10^{12-13} \text{ M}_{\odot}$ in the most extreme cases, exceeding the dynamical masses we measure in some of our galaxies by at least an order of magnitude (e.g., Nesvadba et al. 2007; Collet et al. 2015b). The alternative explanation would be that each hydrogen atom undergoes multiple cycles of heating and cooling during the jet lifetime, cycling (at least) through the neutral and ionized phase, as would be naturally expected in a turbulent multiphase medium (e.g., Guillard et al. 2009; Nesvadba et al. 2010; Scannapieco & Brügger 2015). As an outcome of this, fairly cold, fairly dense molecular gas as probed by mid-level rotational CO line emission may indeed not be a major tracer of outflows in HzRGs, because the more tenuous gas is preferentially accelerated. This is also the gas that cannot self-shield, and therefore is most susceptible to photoionization by AGN photons (see our discussion of large ionized gas masses in §4.4 and Hopkins & Elvis 2010).

These results add further to the growing evidence that turbulence plays a major role for our understanding of AGN feedback. Galaxies with kinetic jet power $> 10^{47} \text{ erg s}^{-1}$ are exceedingly rare, however, galaxies with few $10^{46} \text{ erg s}^{-1}$ of radio power, which we discuss in more detail in Collet et al. (2015b), are abundant enough to represent a general phase in the formation and early evolution of massive galaxies at high redshift.

8.2. ISM metal enrichment

Gas-phase metal abundances in the interstellar gas are important probes of the integrated past growth history of galaxies. The relationship between the current ISM or stellar metal content and total stellar mass formed in galaxies, the mass-metallicity relationship therefore depends sensitively not only on the total mass of stars formed, but contains also the fingerprints of the growth history of these galaxies. Gas infall through accretion or outflows from AGN and star formation should lower the total metal budget in galaxies. We will now discuss how the metallicities implied by the line ratios discussed in §4.2 may further our understanding of the evolutionary state of HzRGs.

In §4.2 we showed the diagnostic “BPT” diagrams constructed from $[\text{NII}]\lambda 6583$, $\text{H}\alpha$, $[\text{OIII}]\lambda 5007$, and $\text{H}\beta$, and that our galaxies fall within the range expected for galaxies at $z \sim 2.5$, which is significantly offset from the AGN branch of galaxies in the low-redshift Universe. Groves et al. (2006), Kewley et al.

(2013a), and Kewley et al. (2013b) argued, that this offset is mainly an effect of low metallicities in high-redshift gas photoionized by AGN compared to local AGN narrow-line regions, which often have metallicities of few times the solar value of $12 + [\text{O}/\text{H}] = 8.96$ (Allende Prieto et al. 2001). They argue that this offset comes in particular from a lowering in the $[\text{NII}]/\text{H}\alpha$ ratio, which is dominated by the lower metallicities at high redshift. Compared with the diagrams of Groves et al. (2006) we find that our galaxies fall mainly within a metallicity range between $1\text{--}4\times$ the solar value (Fig. 22).

Metallicities of about solar have previously been derived for HzRGs in a similar redshift range by Vernet et al. (2001) and Humphrey et al. (2008), based on rest-frame UV lines, in particular $[\text{NV}]$ and HeII . These lines have high ionization potentials, requiring a hard, intense radiation field, which suggests they are most sensitive to the very inner regions of the galaxy near the AGN. It is therefore interesting that also the optical lines, probing less extreme environments more representative of the global ISM of our galaxies, suggest solar to supersolar metallicity, including galaxies which have very extended emission-line regions that reach far beyond the effective radii of massive galaxies of few kpc. Villar-Martín et al. (2002) also suggested based on a rest-UV longslit spectrum of the $z=2.6$ HzRG TXS 0828+193 that metals of at least $1/3 Z_{\odot}$ are likely to be present within the high surface-brightness gas out to few 10s of kpc from the galaxy's nucleus. This suggests that the gas in the extended emission-line regions has already been strongly processed by stars, as expected in the outflow scenario.

Several arguments have been put forward in recent years that HzRGs must be in the last stages of their assembly, including their high stellar and dynamical masses (Seymour et al. 2007; De Breuck et al. 2010; Nesvadba et al. 2007), the proximity of their black hole and bulge masses to the relationship found in local galaxies (Nesvadba et al. 2011b), and their black hole and bulge growth rates (Drouart et al. 2014). If these galaxies have indeed not significantly increased their stellar mass between $z\sim 2$ and today, then this implies that the metal enrichment in their interstellar gas must already be at least as high as that found in the photospheres of stars in massive galaxies today.

Gallazzi et al. (2005) used the SDSS DR2 to estimate stellar metallicities of 175128 nearby galaxies, finding a typical metallicity range of one to two times the solar value for galaxies with stellar masses of $M_{\text{stellar}} = 10^{11.5} M_{\odot}$ and above. Finding gas-phase metallicities that are as high or even higher in our sources supports the view that the active phase of star formation in HzRGs must be very near its end. Finding somewhat higher gas-phase than stellar metallicities is in fact expected, because stars continue to expel metals as they evolve, even if no new stars are formed. Gallazzi et al. (2005) find an offset of about 0.5 dex between the stellar and gas-phase metallicities in low-redshift galaxies at a given stellar mass. If we take our results at face value, then we find a gas-phase metallicity enhancement of a factor of 2 at $z=2$ compared to a factor 3 at $z=0$. This underlines again the absence of subsequent star formation in massive galaxies between $z=2$ and $z=0$.

9. Summary

We presented an analysis of 33 powerful radio galaxies at $z\sim 2$ with previously unpublished SINFONI imaging spectroscopy of the bright rest-frame optical emission lines from warm ionized gas. Including already published sources with similar data sets, our total sample size is 49, corresponding to about $1/3$ of the total number of such galaxies currently known in this redshift range.

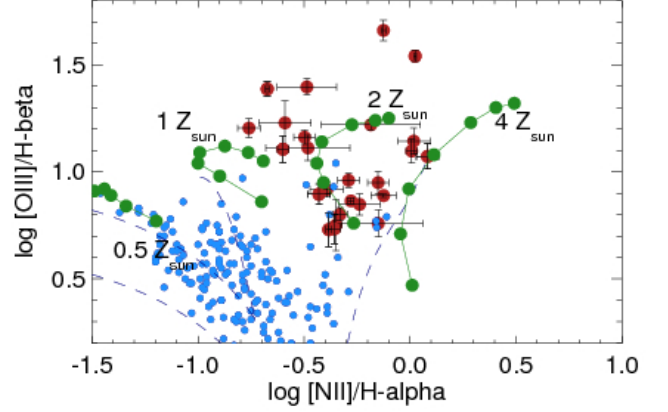


Fig. 22. $[\text{NII}]/\text{H}\alpha$ vs. $[\text{OIII}]/\text{H}\beta$ diagnostic diagram with our sources as already shown in Fig. 2, but now also with the tracks for different metallicities overplotted that Groves et al. (2006) modeled for galaxies with narrow-line regions of different metallicity (green dots and lines) and a range of ionization parameter (see Tab. 2 in Groves et al. 2006, for details). The range of our sources corresponds well to metallicities between 1 and $4\times$ the solar value. Dashed dark blue lines indicate the star-forming and AGN sequence from Kewley et al. (2013a). Light blue dots show the sample of Steidel et al. (2014) of UV/optically selected star-forming galaxies at similar redshifts, and with detections of all four lines.

We studied the gas surface brightness in $[\text{OIII}]\lambda\lambda 4959, 5007$ and $\text{H}\alpha$, diagnostic line ratios, extinction, and the spatially resolved and integrated kinematic properties of the gas. Our main results are as follows:

- HzRGs are commonly surrounded by extended emission line regions with complex, irregular gas kinematics. FWHM line widths are typically between 500 and 1000 km s^{-1} , velocity fields consist either of two bubbles with a bipolar velocity field or are irregular, potentially with multiple bubbles. This qualitatively corresponds to the flood and channel phase predicted by the hydrodynamic models of Sutherland & Bicknell (2007); Wagner & Bicknell (2011); Wagner et al. (2012).
- The ratio of bulk velocity to velocity dispersion in our sample does not scale with ellipticity in the way expected for rotationally or dispersion-dominated early-type galaxies. This disfavors gravitational motion as the main cause of the emission-line kinematics in our sources. The same is suggested by the higher line widths compared to mass-selected galaxies in the same mass range with SINFONI data, and without obvious (radio-loud or radio-quiet) AGN.
- We find a number of empirical trends and correlations between the gas and jet properties. These include (1) good alignment between the gas and radio jet axis to within less than about 20° for most sources. (2) The size of the emission line regions, which is always less than the size of the radio jets, except in a few sources where the jet size is smaller than the typical size of high-redshift galaxies. (3) Aspect ratios of the emission-line regions and jet size scale broadly as expected from hydrodynamic models of light jets with high density contrast. (4) $\text{H}\alpha$ and $[\text{OIII}]$ morphologies and line profiles are very similar. (5) Kinetic energy of the gas and the radio source are strongly correlated, where the gas ki-

netic energy corresponds to about 10^{-2} to 10^{-3} of that of the radio jet.

- At all jet kinetic energies we find sources where the kinetic energy derived from the line widths (unordered motion) exceeds that from global, ordered, bulk flow (ordered motion). While it is not clear whether the unordered motion corresponds to turbulence in the strict physical sense, or is dominated by unresolved, local outflows, we do see a discontinuity at jet kinetic energies of around 1×10^{47} erg s $^{-1}$, where the number of galaxies with higher kinetic energy in bulk flow than unordered motion starts to dominate. We suggest that this could be a transition between galaxies where the ISM is being stirred up by the radio jet, but where interactions are only local, and galaxies, where the energy injection from the radio jet is so strong that the global ISM in the host is being disrupted.
- Using the recent redshift-dependent diagnostic diagrams of Kewley et al. (2013a), we find that the ratios of bright optical emission lines, [NII] λ 6583, H α , [OIII] λ 5007, and H β , are consistent with expectations of cosmological models regarding the global metallicity evolution of galaxies. Gas-phase metallicities in our sources are about $1 - 2 \times Z_{\odot}$, similar to the luminosity-weighted metallicities of the stellar populations in massive galaxies at low redshift. This is expected if the outflowing gas in our sample galaxies represented the same ISM from which these stars formed.
- Overall, we find a good global correspondence between the observed velocities and velocities predicted by recent hydrodynamic models. The axis ratios of the emission-line regions correspond roughly to the density contrast between jet plasma and ambient medium expected for light jets at high redshift.

Generally speaking, our observations are in agreement with expectations from hydrodynamic models, however, we also find that the efficiencies of the kinetic energy transfer from the jets to the gas, and the velocities do differ. The discontinuity in the ratio between the kinetic energy from global bulk flow and localized unordered (perhaps turbulent) motion has so far not been observed, and deserves further scrutiny. Our current results suggest that it is the outcome of the very high energy injection rates from the most powerful radio jets, which might be sufficient to disrupt the global interstellar medium of the most massive high-redshift galaxies. This means also that the interplay between bulk flow and turbulence is an important, so far rather neglected, aspect of AGN feedback at high redshift. Taken together, all of this suggests that AGN feedback is a rich, complex phenomenon, that we are only starting to understand.

Acknowledgments

We would like to thank the staff at Paranal observatory for having carried out the observations, and the ESO OPC for the extraordinary allocation of observing time. We thank the referee for insightful comments, which helped improve the paper. We also thank I. Tanaka for interesting discussions and sharing some of his results on 3C 23.56, and Zelenkova and Parijskij for sharing their radio map of RC 0311+0507 with us. NPHN wishes to thank C. Carilli for interesting discussions and for sharing his VLA data of parts of our sample. She would also like to thank G. Bicknell, A. Wagner, M. Krause and V. Gaibler for enlightening discussions about radio jets, and L. Kewley for equally interesting discussions about metallicities. CC wishes to acknowledge

support from the Ecole Doctorale Astronomie & Astrophysique de l'Île de France.

References

- Alatalo, K., Blitz, L., Young, L. M., et al. 2011, *ApJ*, 735, 88
 Alexander, P. & Leahy, J. P. 1987, *MNRAS*, 225, 1
 Allende Prieto, C., Lambert, D. L., & Asplund, M. 2001, *ApJ*, 556, L63
 Archibald, E. N., Dunlop, J. S., Hughes, D. H., et al. 2001, *MNRAS*, 323, 417
 Barger, A. J., Cowie, L. L., Chen, C.-C., et al. 2014, *ApJ*, 784, 9
 Baum, S. A., Heckman, T. M., & van Breugel, W. 1992, *ApJ*, 389, 208
 Best, P. N., Bailer, D. M., Longair, M. S., & Riley, J. M. 1995, *MNRAS*, 275, 1171
 Blundell, K. M. & Fabian, A. C. 2011, *MNRAS*, 412, 705
 Broderick, J. W., Bryant, J. J., Hunstead, R. W., Sadler, E. M., & Murphy, T. 2007a, *MNRAS*, 381, 341
 Broderick, J. W., De Breuck, C., Hunstead, R. W., & Seymour, N. 2007b, *MNRAS*, 375, 1059
 Broderick, J. W., De Breuck, C., Hunstead, R. W., & Seymour, N. 2007c, *MNRAS*, 375, 1059
 Bryant, J. J., Johnston, H. M., Broderick, J. W., et al. 2009, *MNRAS*, 395, 1099
 Buitrago, F., Conselice, C. J., Epinat, B., et al. 2014, *MNRAS*, 439, 1494
 Cano-Díaz, M., Maiolino, R., Marconi, A., et al. 2012, *A&A*, 537, L8
 Carilli, C. L., Harris, D. E., Pentericci, L., et al. 2002, *ApJ*, 567, 781
 Carilli, C. L., Röttgering, H. J. A., van Ojik, R., Miley, G. K., & van Breugel, W. J. M. 1997, *ApJS*, 109, 1
 Cattaneo, A., Faber, S. M., Binney, J., et al. 2009, *Nature*, 460, 213
 Cavagnolo, K. W., McNamara, B. R., Nulsen, P. E. J., et al. 2010, *ApJ*, 720, 1066
 Chambers, K. C., Miley, G. K., van Breugel, W. J. M., et al. 1996, *ApJS*, 106, 247
 Christensen, L., Jahnke, K., Wisotzki, L., & Sánchez, S. F. 2006, *A&A*, 459, 717
 Cimatti, A., Dey, A., Breugel, W. v., Hurt, T., & Antonucci, R. 1997, *ApJ*, 476, 677
 Collet, C. 2014, PhD thesis
 Collet, C., Nesvadba, N. P. H., De Breuck, C., et al. 2015a, *A&A*, 579, A89
 Collet, C., Nesvadba, N. P. H., De Breuck, C., et al. 2015b, *ArXiv e-prints*
 Cooke, E. A., Hatch, N. A., Muldrew, S. I., Rigby, E. E., & Kurk, J. D. 2014, *MNRAS*, 440, 3262
 Cooper, J. L., Bicknell, G. V., Sutherland, R. S., & Bland-Hawthorn, J. 2008, *ApJ*, 674, 157
 Davé, R., Oppenheimer, B. D., Katz, N., Kollmeier, J. A., & Weinberg, D. H. 2010, *MNRAS*, 408, 2051
 De Breuck, C., Neri, R., & Omont, A. 2003, *New Astronomy Review*, 47, 285
 De Breuck, C., Seymour, N., Stern, D., et al. 2010, *ApJ*, 725, 36
 De Breuck, C., van Breugel, W., Röttgering, H. J. A., & Miley, G. 2000, *A&AS*, 143, 303
 de Ruiter, H. R., Parma, P., Capetti, A., Fanti, R., & Morganti, R. 2002, *A&A*, 396, 857
 Dopita, M. A. & Sutherland, R. S. 2003, *Astrophysics of the diffuse universe*
 Douglas, J. N., Bash, F. N., Bozayan, F. A., Torrence, G. W., & Wolfe, C. 1996, *AJ*, 111, 1945
 Drouart, G., De Breuck, C., Vernet, J., et al. 2014, *A&A*, 566, A53
 Dyson, J. E. & Williams, D. A. 1980, *Physics of the interstellar medium* (New York, Halsted Press, 1980. 204 p.)
 Emonts, B. H. C., De Breuck, C., Lehnert, M. D., et al. 2015, *ArXiv e-prints*
 Emonts, B. H. C., Morganti, R., Tadhunter, C. N., et al. 2005, *MNRAS*, 362, 931
 Emonts, B. H. C., Norris, R. P., Feain, I., et al. 2014, *MNRAS*, 438, 2898
 Emsellem, E., Cappellari, M., Krajnović, D., et al. 2011, *MNRAS*, 414, 888
 Erb, D. K., Shapley, A. E., Pettini, M., et al. 2006, *ApJ*, 644, 813
 Ferland, G. J. 2003, *ARA&A*, 41, 517
 Förster Schreiber, N. M., Genzel, R., Bouché, N., et al. 2009a, *ApJ*, 706, 1364
 Förster Schreiber, N. M., Genzel, R., Bouché, N., et al. 2009b, *ApJ*, 706, 1364
 Gaibler, V., Camenzind, M., & Krause, M. 2007, *ArXiv e-prints*, 710
 Gaibler, V., Khochfar, S., & Krause, M. 2011, *MNRAS*, 411, 155
 Gaibler, V., Krause, M., & Camenzind, M. 2009, *MNRAS*, 400, 1785
 Gallazzi, A., Charlot, S., Brinchmann, J., White, S. D. M., & Tremonti, C. A. 2005, *MNRAS*, 362, 41
 Griffith, M. R. & Wright, A. E. 1993, *AJ*, 105, 1666
 Groves, B. A., Heckman, T. M., & Kauffmann, G. 2006, *MNRAS*, 371, 1559
 Guillard, P., Boulanger, F., Pineau Des Forêts, G., & Appleton, P. N. 2009, *A&A*, 502, 515
 Harwood, J. J., Croston, J. H., Intema, H. T., et al. 2016, *ArXiv e-prints*
 Hatch, N. A., Kurk, J. D., Pentericci, L., et al. 2011, *MNRAS*, 415, 2993
 Hatch, N. A., Overzier, R. A., Röttgering, H. J. A., Kurk, J. D., & Miley, G. K. 2008, *MNRAS*, 383, 931
 Hayashi, M., Kodama, T., Tadaki, K.-i., Koyama, Y., & Tanaka, I. 2012, *ApJ*, 757, 15

- Hayward, C. C. & Hopkins, P. F. 2015, ArXiv e-prints
- Heckman, T. M. & Best, P. N. 2014, ARA&A, 52, 589
- Hopkins, P. F., Bundy, K., Hernquist, L., & Ellis, R. S. 2007, ApJ, 659, 976
- Hopkins, P. F. & Elvis, M. 2010, MNRAS, 401, 7
- Humphrey, A., Iwamuro, F., Villar-Martín, M., Binette, L., & Sung, E. C. 2009, MNRAS, 399, L34
- Humphrey, A., Villar-Martín, M., Vernet, J., et al. 2008, MNRAS, 383, 11
- Humphrey, A., Zeballos, M., Aretxaga, I., et al. 2011, MNRAS, 418, 74
- Ivison, R. J., Morrison, G. E., Biggs, A. D., et al. 2008, MNRAS, 390, 1117
- Kauffmann, G., Heckman, T. M., White, S. D. M., et al. 2003, MNRAS, 341, 54
- Kewley, L. J., Dopita, M. A., Leitherer, C., et al. 2013a, ApJ, 774, 100
- Kewley, L. J., Dopita, M. A., Sutherland, R. S., Heisler, C. A., & Trevena, J. 2001, ApJ, 556, 121
- Kewley, L. J., Groves, B., Kauffmann, G., & Heckman, T. 2006, MNRAS, 372, 961
- Kewley, L. J., Maier, C., Yabe, K., et al. 2013b, ApJ, 774, L10
- Knopp, G. P. & Chambers, K. C. 1997, ApJS, 109, 367
- Koyama, Y., Kodama, T., Tadaki, K.-i., et al. 2013, MNRAS, 428, 1551
- Krause, M. 2003, A&A, 398, 113
- Kuiper, E., Hatch, N. A., Miley, G. K., et al. 2011, MNRAS, 415, 2245
- Kurk, J. D., Pentericci, L., Overzier, R. A., Röttgering, H. J. A., & Miley, G. K. 2004, A&A, 428, 817
- Laing, R. A., Riley, J. M., & Longair, M. S. 1983, MNRAS, 204, 151
- Large, M. I., Mills, B. Y., Little, A. G., Crawford, D. F., & Sutton, J. M. 1981, MNRAS, 194, 693
- Le Fevre, O., Deltorn, J. M., Crampton, D., & Dickinson, M. 1996, ApJ, 471, L11+
- Lehnert, M. D., Nesvadba, N. P. H., Tiran, L. L., et al. 2009, ApJ, 699, 1660
- Mantovani, F., Junor, W., Fanti, R., Padrielli, L., & Saikia, D. J. 1994, A&A, 292, 59
- Martig, M., Bournaud, F., Teyssier, R., & Dekel, A. 2009, ApJ, 707, 250
- Mauch, T., Murphy, T., Buttery, H. J., et al. 2003, MNRAS, 342, 1117
- McCarthy, P. J., van Breughel, W., Kapahi, V. K., & Subrahmanya, C. R. 1991, AJ, 102, 522
- McConnell, D., Sadler, E. M., Murphy, T., & Ekers, R. D. 2012, VizieR Online Data Catalog, 742, 21527
- Miley, G. & De Breuck, C. 2008, A&A Rev., 1
- Morganti, R., Tadhunter, C. N., & Oosterloo, T. A. 2005, A&A, 444, L9
- Murgia, M., Fanti, C., Fanti, R., et al. 1999, A&A, 345, 769
- Nawaz, M. A., Wagner, A. Y., Bicknell, G. V., Sutherland, R. S., & McNamara, B. R. 2014, MNRAS, 444, 1600
- Nesvadba, N., Boulanger, F., Lehnert, M., Guillard, P., & Salome, P. 2011a, ArXiv e-prints
- Nesvadba, N., Boulanger, F., Salome, P., et al. 2010, A&A, accepted
- Nesvadba, N. P. H., De Breuck, C., Lehnert, M. D., et al. 2011b, A&A, 525, A43
- Nesvadba, N. P. H., Lehnert, M. D., Davies, R. I., Verma, A., & Eisenhauer, F. 2008a, A&A, 479, 67
- Nesvadba, N. P. H., Lehnert, M. D., De Breuck, C., Gilbert, A., & van Breugel, W. 2007, A&A, 475, 145
- Nesvadba, N. P. H., Lehnert, M. D., De Breuck, C., Gilbert, A. M., & van Breugel, W. 2008b, A&A, 491, 407
- Nesvadba, N. P. H., Lehnert, M. D., Eisenhauer, F., et al. 2006a, ApJ, 650, 661
- Nesvadba, N. P. H., Lehnert, M. D., Eisenhauer, F., et al. 2006b, ApJ, 650, 693
- Nesvadba, N. P. H., Neri, R., De Breuck, C., et al. 2009, MNRAS, 395, L16
- Nesvadba, N. P. H., Polletta, M., Lehnert, M. D., et al. 2011c, MNRAS, 415, 2359
- Ogle, P., Boulanger, F., Guillard, P., et al. 2010, ApJ, 724, 1193
- Ogle, P., Davies, J. E., Appleton, P. N., et al. 2012, ApJ, 751, 13
- Osterbrock, D. E. 1989, Astrophysics of gaseous nebulae and active galactic nuclei
- Overzier, R. A., Harris, D. E., Carilli, C. L., et al. 2005, A&A, 433, 87
- Owsianik, I. & Conway, J. E. 1998, A&A, 337, 69
- Pariiskii, Y. N., Goss, V. M., Kopylov, A. I., et al. 1998, Astronomy Reports, 42, 425
- Pariiskij, Y. N., Thomasson, P., Kopylov, A. I., et al. 2014, MNRAS, 439, 2314
- Pearson, T. J. 1975, MNRAS, 171, 475
- Pentericci, L., McCarthy, P. J., Röttgering, H. J. A., et al. 2001, ApJS, 135, 63
- Pentericci, L., Van Reeve, W., Carilli, C. L., Röttgering, H. J. A., & Miley, G. K. 2000, A&AS, 145, 121
- Pilkington, J. D. H. & Scott, J. F. 1965, MNRAS, 69, 183
- Reuland, M., Röttgering, H., van Breugel, W., & De Breuck, C. 2004, MNRAS, 353, 377
- Rocca-Volmerange, B., Drouart, G., De Breuck, C., et al. 2013, MNRAS, 429, 2780
- Scannapieco, E. 2013, ApJ, 763, L31
- Scannapieco, E. & Brüggén, M. 2015, ArXiv e-prints
- Seymour, N., Stern, D., De Breuck, C., et al. 2007, ApJS, 171, 353
- Silk, J. & Rees, M. J. 1998, A&A, 331, L1
- Slee, O. B. 1995, Australian Journal of Physics, 48, 143
- Steidel, C. C., Rudie, G. C., Strom, A. L., et al. 2014, ApJ, 795, 165
- Sutherland, R. S. & Bicknell, G. V. 2007, ApJS, 173, 37
- Tacconi, L. J., Genzel, R., Neri, R., et al. 2010, Nature, 463, 781
- Tadhunter, C. N., Morganti, R., di Serego-Alighieri, S., Fosbury, R. A. E., & Danziger, I. J. 1993, MNRAS, 263, 999
- Tanaka, I., Breuck, C. D., Kurk, J. D., et al. 2011, PASJ, 63, 415
- Targett, T. A., Dunlop, J. S., McLure, R. J., et al. 2011, MNRAS, 412, 295
- Thompson, T. A. & Krumholz, M. R. 2016, MNRAS, 455, 334
- van Breugel, W. J. M., Stanford, S. A., Spinrad, H., Stern, D., & Graham, J. R. 1998, ApJ, 502, 614
- van de Sande, J., Kriek, M., Franx, M., Bezanson, R., & van Dokkum, P. G. 2014, ApJ, 793, L31
- van Ojik, R., Roettgering, H. J. A., Carilli, C. L., et al. 1996, A&A, 313, 25
- Veilleux, S. & Osterbrock, D. E. 1987, ApJS, 63, 295
- Venemans, B. P., Kurk, J. D., Miley, G. K., et al. 2002, ApJ, 569, L11
- Venemans, B. P., Röttgering, H. J. A., Miley, G. K., et al. 2007, A&A, 461, 823
- Vernet, J., Fosbury, R. A. E., Villar-Martín, M., et al. 2001, A&A, 366, 7
- Villar-Martín, M., Sánchez, S. F., De Breuck, C., et al. 2006, MNRAS, 366, L1
- Villar-Martín, M., Tadhunter, C., & Clark, N. 1997, A&A, 323, 21
- Villar-Martín, M., Vernet, J., di Serego Alighieri, S., et al. 2003, MNRAS, 346, 273
- Villar-Martín, M., Vernet, J., di Serego Alighieri, S., et al. 2002, MNRAS, 336, 436
- Wagner, A. Y. & Bicknell, G. V. 2011, ApJ, 728, 29
- Wagner, A. Y., Bicknell, G. V., & Umemura, M. 2012, ApJ, 757, 136
- Wall, J. V. & Peacock, J. A. 1985, MNRAS, 216, 173
- Willott, C. J., Rawlings, S., Blundell, K. M., & Lacy, M. 1999, MNRAS, 309, 1017
- Willott, C. J., Rawlings, S., Blundell, K. M., Lacy, M., & Eales, S. A. 2001, MNRAS, 322, 536
- Wright, A. & Otrupcek, R. 1990, in PKS Catalog (1990), 0
- Wylezalek, D., Galametz, A., Stern, D., et al. 2013, ApJ, 769, 79
- Zahid, H. J., Damjanov, I., Geller, M. J., & Chilingarian, I. 2015, ApJ, 806, 122
- Zirm, A. W., Overzier, R. A., Miley, G. K., et al. 2005, ApJ, 630, 68

Source	L([OIII]) [$10^9 L_\odot$]	L(H α) [$10^9 L_\odot$]	L(H β) [$10^9 L_\odot$]	A_V [mag]	L(H α ,c) [$10^9 L_\odot$]	L(H β ,c) [$10^9 L_\odot$]	M_{WIM} [$10^9 M_\odot$]	M_{CO} [$10^{10} M_\odot$]	M_{WIM}/M_{CO} [M_\odot]	Reference
MRC 0114–211	7.3 \pm 0.1	15.2 \pm 0.2	0.9 \pm 0.1	4.65 \pm 0.22	197.1 \pm 21.7	68.4 \pm 8	4.9 \pm 0.5	3.6 \pm 0.7	0.14 \pm 0.03	E14
BRL 0128–264	38 \pm 1.2	13.4 \pm 0.8	5.4 \pm 2.2	0.0	13.4 \pm 0.8	5.4 \pm 2.2	0.3 \pm 0.02
MRC 0156–252	161 \pm 4	36.6 \pm 1.1	9.7 \pm 5.2	0.73 \pm 0.06	54.8 \pm 12.6	19.0 \pm 4.4	1.4 \pm 0.3	7.4 \pm 1.5	0.02 \pm 0.006	E14
USS 0211–122	67 \pm 0.4	21.9 \pm 0.2	6.2 \pm 0.8	0.55 \pm 0.13	29.7 \pm 0.3	10.3 \pm 0.6	0.8 \pm 0.05	3.7	0.02	E14
MRC 0251–273	91 \pm 2.1	...	6.0 \pm 2.3	> 0.4
MP J0340–6507	98 \pm 1.1	35.3 \pm 1.0	15.5 \pm 1.2	0.0	0.9 \pm 0.02	...	2.2	E14
PKS 0529–549	101.3 \pm 0.4	56.5 \pm 1.7	13.8 \pm 0.2	0.94 \pm 0.013	95.3 \pm 1.4	33.1	2.4 \pm 2.4
5C 7.267	1.6 \pm 0.5	3.0 \pm 0.4	>0.1
TN J1112–2948	35.5 \pm 0.9	...	3.2 \pm 0.9	< 0.3
TXS 1113–178	24.6 \pm 0.3	8.23 \pm 0.4	2.4 \pm 0.3	0.5 \pm 0.06	10.8 \pm 0.6	3.8 \pm 0.2	0.3 \pm 0.02
3C 257	111 \pm 1.3	44.8 \pm 0.1	12.5 \pm 1.4	0.6 \pm 0.03	62.0 \pm 8.3	21.5 \pm 2.9	1.5 \pm 0.2
USS 1243+036	87.4 \pm 1.5	...	8.53 \pm 2.1	< 0.6
MG 1251+1104	118 \pm 7.6	62.8 \pm 9.7	1.6 \pm 0.2
MRC 1324–262	40.2 \pm 2.2	15.6 \pm 1.8	5.2 \pm 2.5	0.1 \pm 0.2	16.6 \pm 8	5.8 \pm 2.8	0.4 \pm 0.2
USS 1410–001	163 \pm 1.4	52.0 \pm 0.9	10.2 \pm 1.2	1.5 \pm 0.05	121.5 \pm 12	42.2 \pm 4.2	3. \pm 0.3
MRC 1558–003	104 \pm 1.6	46.6 \pm 1.6	11.4 \pm 1.3	0.9 \pm 0.05	78.4 \pm 9	27.2 \pm 3	2. \pm 0.2
USS 1707+105	26.4 \pm 0.6	7.8 \pm 0.6	1.6 \pm 0.4	1.4 \pm 0.16	17.1 \pm 2	5.9 \pm 0.7	0.4 \pm 0.05
3C 362	80.4 \pm 0.9	34.2 \pm 0.9	3.2 \pm 1.0	3.5 \pm 0.3	239.8 \pm 150	83.2 \pm 53	6.0 \pm 4.0
MP 1758–6738	28.6 \pm 0.6	9.5 \pm 1.1	0.2 \pm 0.02
TN J2007–1316	105 \pm 1.8	...	20.0 \pm 1.8	1.5 \pm 0.2
MRC 2025–218	116 \pm 1.5	25.1 \pm 3.2	0.6 \pm 0.08	3.8 \pm 1.0	0.015 \pm 0.002	E14
MG 2037–0011	1.9 \pm 0.2	2.0 \pm 0.2	0.05 \pm 0.005
MRC 2104–242	48.5 \pm 0.5	28.3 \pm 0.6	3.3 \pm 0.4	2.9 \pm 0.05	140.5 \pm 16.9	48.8 \pm 6	3.5 \pm 0.06	<2	\geq 0.2	E11
4C 23.56	133 \pm 4.7	36.7 \pm 2.7	10.3 \pm 4.7	0.6 \pm 0.2	50.4 \pm 22.7	17.5 \pm 7.9	1.3 \pm 0.4
NVSS J2135–3337	...	4.2 \pm 0.2	0.1 \pm 0.005
MG 2144+1928	96.2 \pm 3.1	...	5.4 \pm 0.8	0.4 \pm 0.06
MRC 2224–273	...	31.4 \pm 0.8	0.4 \pm 0.01	<2	\geq 0.2	E14
TN J2254+1857	5.0 \pm 0.4	5.8 \pm 0.5	0.15 \pm 0.01
MG 2308+0336	62.6 \pm 1.4	28.2 \pm 0.9	7.57 \pm 1.2	0.7 \pm 0.07	41.3 \pm 6.6	14.4 \pm 2.3	1.0 \pm 0.2

Table 6. Line luminosities and warm ionized gas masses for fiducial electron densities of $n=500 \text{ cm}^{-3}$. Error bars include measurement errors only.

Appendix A: Individual Objects

A.1. MRC 0114-211

MRC0114–211 at $z=1.4$ is the lowest-redshift target in our sample. De Breuck et al. (2010, see also Seymour et al. 2007) find a stellar mass of $M_{\text{stellar}} = 2.5 \times 10^{11} M_{\odot}$ and mid-IR emission dominated by a stellar continuum. It has a compact steep radio spectrum in the GHz regime, with two hotspots offset by $<0.5''$ (Mantovani et al. 1994) and with a high rotation measure of $RM=646 \text{ rad m}^{-2}$ in the rest-frame, probably a signature of dense gas surrounding the radio source. De Breuck et al. (2010) found a faint radio core, which is resolved only in their 8.46 GHz VLA A-array imaging. The radio map shown in the right panel of Fig. A.4 was smoothed to $0.5''$ to be more comparable with the SINFONI data, and therefore shows only a single radio source.

At $z=1.4$, we cover all bright rest-frame optical lines from $H\beta$ to the rest-frame near-infrared lines of $[\text{SiII}]\lambda\lambda 9069, 9513$. Line emission extends over $1.6'' \times 1.1''$, not much larger than the seeing disk of a size of $1.0'' \times 1.1''$. The deconvolved size along the major axis, which is roughly aligned east-west, is $1.2''$, corresponding to 9.7 kpc. We consider this size an upper limit.

All emission lines are adequately fit with single Gaussian components. We find $\text{FWHM}=673 \pm 6 \text{ km s}^{-1}$ for $[\text{OIII}]\lambda 5007$, and use the same width for the other lines as well. This enables us in particular to decompose $H\alpha$ and $[\text{NII}]\lambda\lambda 6548, 6583$, which are strongly blended. This approach does not produce significant fit residuals. The results of our fits to the integrated spectrum are summarized in Table A.5.

The line-free continuum image of MRC 0114–211 shows two peaks at a relative projected distance of $1.3''$ (corresponding to 11 kpc at $z=1.41$). The fainter peak is centered on the emission-line region, the brighter peak falls outside. If not an interloper, then this may be a nearby, perhaps interacting galaxy. We do not detect line emission associated with the bright continuum emitter in any of our bands.

A.2. BLR 0128-264

BLR 0128–264 at $z=2.35$ has very extended radio jets with a projected size of $35.8''$, corresponding to 294 kpc at $z=2.35$, and is one of our most powerful radio galaxies, with $P_{500} = 29.1 \text{ W Hz}^{-1}$ at 500 MHz in the rest-frame. With SINFONI we detect $[\text{OIII}]\lambda\lambda 4959, 5007$, $H\beta$ and $H\alpha$, as well as $[\text{SiII}]\lambda\lambda 6716, 6731$, and $[\text{NII}]\lambda 6583$ (Fig. A.1). The lines are well fit with a single component of $\text{FWHM}=1136 \pm 20 \text{ km s}^{-1}$ (the error is that measured for $[\text{OIII}]\lambda 5007$). The fitting parameters for all lines are given in Table A.5.

Line emission in BLR 0128-264 is spatially resolved but not very extended with a size of $3.2'' \times 1.5''$ along the major and minor axis, respectively. Compact continuum emission is detected roughly in the center of the emission line region. The emission line morphology is fairly regular, albeit with higher $[\text{OIII}]\lambda 5007$ surface brightness towards the north (Fig. A.4). The velocity field of BLR 0128–264 has a remarkably large gradient of $\Delta v \sim 1500 \text{ km s}^{-1}$. Resolved FWHM line widths are between 700 and 2200 km s^{-1} . The largest widths coincide with the continuum position, and may be partially broadened by the steep and large velocity gradient. The right panel of Fig. A.4 shows that the direction towards the radio hotspot is roughly aligned with the major axis of the emission-line region and the velocity gradient, in particular for the north-western jet.

A.3. MRC 0156-252

MRC 0156–252 at $z=2.02$ is one of our galaxies with very extended emission-line gas. Line emission is bright, but given the somewhat difficult redshift, we only detect $[\text{OIII}]\lambda\lambda 4959, 5007$, $H\beta$, $H\alpha$, and $[\text{NII}]\lambda 6583$ in the integrated spectrum (Fig. A.1). Line properties are listed in Table A.5. We probe $[\text{OIII}]\lambda 5007$ over an area of $69 \text{ kpc} \times 23 \text{ kpc}$ along the major and minor axis, respectively. The emission-line region corresponds to a bright inner region, which extends over $1.5''$ (13 kpc), and two extended emission-line plumes, with the larger plume to the south. The continuum is compact and roughly centered on the central part of the emission-line region. MRC 0156-252 offers a direct line of sight into the AGN, as seen through nuclear $H\alpha$ broad-line emission (Nesvadba et al. 2011b). It is therefore possible that parts of the emission-line morphology in the central region are influenced by the wings of the unresolved nuclear point source, although we removed this component from the data cube before fitting the residual line emission (§3.2). We suspect this is the case in particular for the asymmetric $[\text{OIII}]\lambda 5007$ surface-brightness distribution. Although forbidden lines like $[\text{OIII}]\lambda 5007$ do not probe the broad-line region itself, they may still show a near-nuclear component from the inner narrow-line region, where we expect a boost of bright high-ionization lines like $[\text{OIII}]\lambda 5007$. The extended lobes are too far away from the nucleus to be possibly affected by residuals of a nuclear point source.

MRC 0156–252 has a regular velocity gradient throughout the central regions and the extended lobes with a total velocity offset of 1600 km s^{-1} , one of the largests in our sample. The line widths are broadest near the center, with up to $\text{FWHM} \sim 900 \text{ km s}^{-1}$, and are between 600 and 800 km s^{-1} in the two lobes. Pentericci et al. (2001) found that the brightest $\text{Ly}\alpha$ emission in MRC 0156–252 is associated with the north-western radio lobe, and suggested that the jet may be deflected off a dense gas cloud at that position. Emonts et al. (2014) detected CO(1-0) emission at the same position.

Other examples, like MRC 1138–262, where the brightest $\text{Ly}\alpha$ emission is also found associated with a gas cloud that is offset from the radio galaxy itself (Kurk et al. 2004), also show large velocity offsets relative to the ambient gas (Nesvadba et al. 2006b; Kuiper et al. 2011). This is not the case here, where the gas near the north-western lobe appears very extended, with a smooth velocity gradient of 800 km s^{-1} , which is similar to that in the south-west of the galaxy. This is not what would be expected from a gas cloud within the surrounding dark-matter environment of MRC 0156–252, but rather ambient gas that has been swept up by the radio jet cocoon.

The radio morphology shown in the right panels of Fig. A.4 shows that the northern rim of the emission-line region aligns very well with the extended radio structure. The south-western radio hotspot is unresolved, fainter, and falls outside the emission-line gas. The line widths are high in the south-western emission-line region, about 650 km s^{-1} , although less so than in the north-eastern region, where they reach $\geq 800 \text{ km s}^{-1}$.

A.4. USS 0211-122

USS 0211–122 at $z=2.34$ has a moderately extended radio source with a size of $16''$ (133 kpc at $z=2.34$) and a moderate radio power (for our sample) of 28.5 W Hz^{-1} at 500 MHz in the rest-frame. Its line emission is however unusual compared to the other sources in our sample. All identified emission lines ($[\text{OIII}]\lambda\lambda 4959, 5007$, $H\beta$, $H\alpha$, $[\text{NII}]\lambda 6583$, $[\text{SiII}]\lambda\lambda 6716, 6731$)

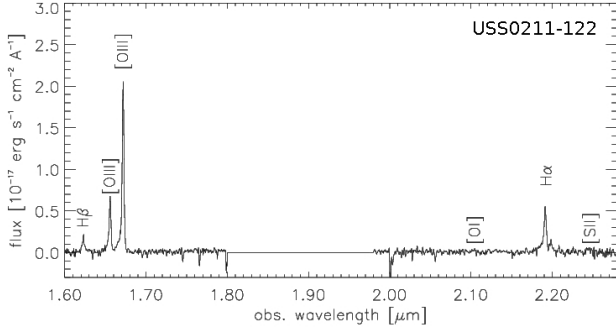


Fig. A.2. Integrated spectrum of USS0211–122.

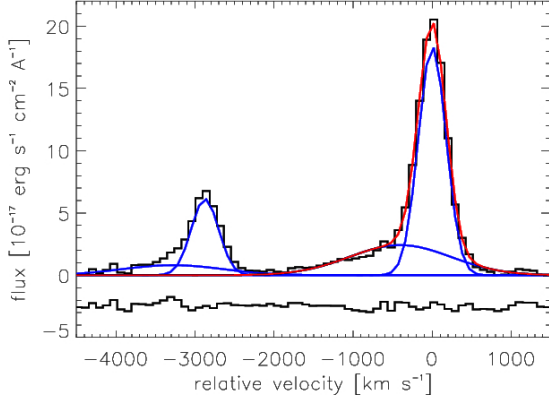


Fig. A.3. Line profile of [OIII] $\lambda\lambda$ 4959,5007 in USS 0211–122 and best fit. The lower spectrum shows the fit residuals.

are very narrow with $\text{FWHM}=275 \text{ km s}^{-1}$. We do see broad blue wings, as shown in Fig. A.3 for the integrated spectrum. When fitting the data cube with two Gaussian components, we find that the broader component is not spatially resolved. The wing is well fit with a Gaussian profile with $\text{FWHM}=1400 \text{ km s}^{-1}$ and a blueshift of -418 km s^{-1} from the narrow line component, consistent with a wind originating from the central regions of this galaxy. The redshift and width of the broad component are fixed to the best-fit parameters of the integrated spectrum.

The maps of the narrow component show gas extended over $2.3'' \times 1.1''$ (corresponding to a deconvolved size of $19 \text{ kpc} \times 9 \text{ kpc}$) and elongated along an axis that goes from south-east to north-west, roughly aligned with the radio jet axis. The velocity field shows a fairly regular gradient of 120 km s^{-1} , although the lowest velocities are found in the northern part of the western bubble, and velocities in the outermost parts of the western bubble are comparable to the highest velocities in the eastern emission-line regions. Line widths are very different on the two sides of the nucleus. Towards the east, they have $\text{FWHM} \sim 300 \text{ km s}^{-1}$, compared to $\text{FWHM}=400-500 \text{ km s}^{-1}$ on the western side, with the largest values reached in the most peripheral gas.

A.5. MRC 0251-273

MRC 0251–273 at $z=3.17$ has a fairly compact radio source with an upper limit of $\text{LAS} < 3.9''$ (De Breuck et al. 2010) and a FIR luminosity $< 1 \times 10^{13} L_{\odot}$ measured with SCUBA (Reuland et al. 2004). It is undetected with SPIRE with an upper limit of $L_{\text{tot}}^{\text{IR}} = 7.6 \times 10^{12} L_{\odot}$ of infrared luminosity (Drouart et al. 2014).

It is a bright, marginally spatially resolved line emitter at a seeing of $0.9'' \times 0.8''$, associated with a fairly bright continuum (Fig. A.4). Velocities and line widths are uniform, with $\text{FWHM}=681 \pm 9 \text{ km s}^{-1}$ (the error refers to [OIII] λ 5007). At the redshift of MRC 0251–273 we detect H β and [OIII] $\lambda\lambda$ 4959,5007 in the K and [OII] λ 3727 in the H-band. The integrated spectrum is shown in Fig. A.1. The two components of the [OII] doublet are blended due to the fairly large intrinsic width of the lines.

The line emission extends over an area of $3.5'' \times 2.5''$ on the sky, corresponding to $26 \text{ kpc} \times 18 \text{ kpc}$ at $z=3.17$, and after deconvolving with the size of the seeing disk. The gas is overall well centered on the unresolved continuum source. The velocity offsets are relatively small, with a total offset of 500 km s^{-1} . There is no single, monotonic gradient, but a blueshift near the center, with more redshifted gas (by $250-500 \text{ km s}^{-1}$) on either side. The FWHM line widths are between 600 and 900 km s^{-1} , with faint regions of more narrow widths at the very periphery of the emission line region ($\text{FWHM} \sim 300 \text{ km s}^{-1}$). The radio map in the right panels of Fig. A.4 shows a small double-peaked structure that is embedded within the emission-line gas and well aligned with the region of blueshifted gas around the center of the emission-line region. The areas of broadest line width are mostly found adjacent to the radio contours.

A.6. RC J0311+0507

RC J0311+0507 (4C+04.11) had previously a spectroscopic redshift of $z=4.514$ measured only from Ly α (Pariiskii et al. 1998). It has recently been described in more detail by Parijskij et al. (2014), who find a very asymmetric radio source extending nearly north-south, with a size of $2.8''$ (18.5 kpc). We identify [OII] $\lambda\lambda$ 3726,3729, and [NeIII] $\lambda\lambda$ 3869,3968 in the K and H-band (Fig. A.9). This is consistent with the previously published redshift, which was based only on Ly α . [OII] $\lambda\lambda$ 3726,3729 is found at good S/N in the integrated spectrum (Fig. A.9). RC J0311+0507 has a complex line profile, with a broad component of $\text{FWHM}=1400 \text{ km s}^{-1}$, superimposed on a component which is narrow enough ($\text{FWHM}=112 \text{ km s}^{-1}$) for the doublet to be spectrally resolved. Our three-component Gaussian fit (modeling the broad component with only one line, and each of the narrow components of the doublet individually).

[OII] $\lambda\lambda$ 3726,3729 is density sensitive, and the flux ratio $F(3727)/F(3729)=0.96 \pm 0.18$ suggests electron densities between 200 and 1000 cm^{-3} , within the range found previously from [SII] $\lambda\lambda$ 6716,6731 measurements (Nesvadba et al. 2006b, 2008a; Collet et al. 2015a). To our knowledge, this is the first estimate of the electron density in an AGN host galaxy at $z \geq 4$.

The line emission in RC J0311+0507 appears fairly compact at the spatial resolution of our data ($\text{FWHM}=1.0'' \times 0.9''$) along right ascension and declination, respectively, corresponding to $6 \times 5.5 \text{ kpc}$ at $z=4.51$). We marginally detect continuum emission at the center of the line emission. The emission-line maps are shown in Fig. A.4. Although nominally, the source appears spatially unresolved, the velocity map (measured from [OII]) does show a gradient of $\sim 220 \text{ km s}^{-1}$. The gas is more blueshifted in roughly the eastern half of the source, where Parijskij et al. (2014) detect the radio continuum in high-resolution observations with MERLIN. The presence of a velocity gradient suggests that the source is marginally spatially resolved with an intrinsic size that is very near the size of the seeing disk.

Collet et al. (2015a) used Monte-Carlo simulations to investigate how low spatial resolution affects measurements of ve-

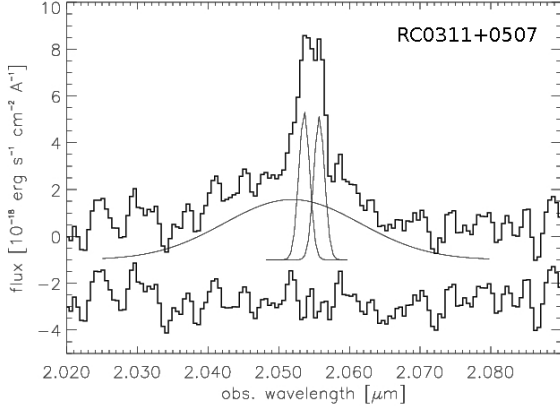


Fig. A.9. Line profile of [OIII] $\lambda\lambda$ 3726,3729 in the integrated spectrum of RC J0311+0507.

locity gradients in marginally spatially resolved SINFONI maps akin to our data. Their analysis suggests that the intrinsic velocity gradient projected onto the line of sight could be about a factor 2 greater. A velocity offset of 400–500 km s⁻¹ would however not strongly affect the FWHM line widths, which are above 900–1000 km s⁻¹ on average, and up to 1300 km s⁻¹ in the western part of the emission-line region.

A.7. MP J0340–6507

MP J0340–6507 at $z=2.28$ shows extended ($3.8'' \times 1.8''$, corrected for the size of the seeing disk), line emission along an axis going from north to south. The [OIII] $\lambda\lambda$ 4959,5007 emission-line region is asymmetry, and shifted by $0.5''$ towards south-west. The continuum is fairly bright and peaks at the same position as the line emission. We note a small velocity gradient of ≈ 200 km s⁻¹. Line widths are FWHM=800–1000 km s⁻¹. Unfortunately, we do not have a radio map of this galaxy with a beam comparable to the resolution of the SINFONI data.

A.8. PKS 0529-549

PKS 0529–549 at $z=2.57$ has extended [OIII] $\lambda\lambda$ 4959,5007 and H α morphologies and a regular velocity gradient of 460 km s⁻¹ (Fig. A.5). Line widths are of-order FWHM \sim 700 km s⁻¹ (Table A.5).

In order to extract a maximal set of constraints from our data cubes of PKS 0529-549, we constructed two cubes. One cube of 45 min exposure time at good seeing ($0.7'' \times 0.6''$), which we used to produce the maps of the gas kinematics of the bright [OIII] $\lambda\lambda$ 4959,5007 lines. In addition we constructed a cube of the full data set of 5.3 hrs to produce an integrated spectrum (where the spatial resolution is of minor importance) to measure the fluxes of fainter lines (Fig. A.1). In total we detect H γ , H β , H α , [OIII] $\lambda\lambda$ 4959,5007, [OI] $\lambda\lambda$ 6300,6363, [NII] λ 6583, and [SII] λ 6724. The lines of the [SII] doublet are blended owing to the intrinsically broad lines. For H α and [NII] λ 6583 the blending is not very strong.

We detect the continuum in the ‘deep’ cube which is unresolved at a spatial resolution of $1.2'' \times 1.2''$ and well centered relative to the emission-line region and velocity gradient.

Broderick et al. (2007c) found a very high rotation measure of -9600 rad m⁻², the largest found so far in a radio galaxy at $z \sim 2$, suggesting a particularly strong magnetic field, dense

environment, or both, and a radio source with largest angular size of $1.2''$. Humphrey et al. (2011) found bright 1.1 m emission from cold dust with AzTEC.

The radio morphology shows a small double source, which has a very similar size to the emission-line region and is well aligned with it. The velocity jump seen in the gas appears to occur between the two radio lobes, consistent with expectations from a back-to-back outflow. The broadest line widths are found inbetween the two radio lobes, which are each associated with gas with FWHM \sim 700–800 km s⁻¹.

A.9. 5C 07.269

5C 07.269 at $z=2.22$ is one of our fainter sources in the radio, with $\log P_{500} = 27.8$ W Hz⁻¹ at 500 MHz in the rest-frame, and a largest angular size of $7.6''$ in the radio (De Breuck et al. 2010). The integrated spectrum shows [OIII] $\lambda\lambda$ 4959,5007 in the H band, and H α , [NII] $\lambda\lambda$ 6548,6583, and [SII] $\lambda\lambda$ 6716,6731 in the K-band. We also detect the faint continuum near the geometric center of the emission-line region.

The emission-line maps in Fig. A.5 show a source that is extended along an axis that goes from the south-east to the north-west. The velocity distribution is irregular, with a total velocity range of ± 350 km s⁻¹ around an average redshift $z=2.22505$, but much of that scatter might be due to the low signal-to-noise ratio of this source. The distribution of line widths appears more regular, with a maximum of 1100 km s⁻¹ near the center, and more moderate velocities of 200–300 km s⁻¹ in the periphery. The broadest gas near the center seems to be associated with the small, unresolved radio core (right panels of Fig. A.5).

A.10. MRC 1017-220

In MRC1017–220 at $z=1.7$, H α falls very near the red end of the H-band at $\lambda = 1.8203 \mu\text{m}$, and [OIII] λ 5007 just outside of the J-band, so that the emission lines are heavily affected by telluric effects. This makes it impossible to measure the emission-line kinematics, line morphologies, or line ratios for this galaxy. Nesvadba et al. (2011b) found and discussed a broad H α line in MRC 1017–220, which extends into cleaner parts of the spectrum. Given these observational complications, we did not include this source in our overall analysis.

A.11. TN J1112-2948

Line emission in TN J1112–2948 at $z=3.1$ is very extended with a size of $6.7'' \times 2.2''$ (52.3 kpc \times 17.3 kpc at $z=3.1$, Fig. A.5). We detect [OIII] $\lambda\lambda$ 4959,5007, H β , and [OII] λ 3727. The emission-line maps shown in Fig. A.5 show high surface-brightness line emission in a resolved area around the nucleus, extending over $2.3'' \times 2.0''$ (18 kpc \times 16 kpc at $z=3.1$) with a small velocity gradient of 180 km s⁻¹ and line widths between FWHM \sim 600 and 800 km s⁻¹. Towards south-east, we see an extended gas plume extending out to a distance of 38 kpc from the nucleus, with velocities of up to 400 km s⁻¹ and FWHM line widths of 300–500 km s⁻¹. The extended line emission in TN J1112–2948 is asymmetric about the radio core, which is associated with the northern cloud. We do not detect another plume towards the north-west, although we obtained a second SINFONI pointing to cover this area specifically. The southern cloud is directly adjacent to the southern radio hotspot, although not perfectly aligned. The overall velocities in TN J1112–2948 are monotonically increasing from the north-west to the south-

east with a total gradient of 700 km s^{-1} . Reuland et al. (2004) detected TN J1112–2948 with SCUBA, Herschel photometry has unfortunately not been obtained for this galaxy.

A.12. TXS 1113–178

TXS 1113–178 at $z=2.24$ shows a broad $\text{H}\alpha$ emission line coming from the nucleus (Nesvadba et al. 2011b), which made it necessary to remove the nuclear point source before analyzing the extended line emission in this source (§3.2). We do detect residual line emission associated with the continuum emission from the nucleus, although it is fairly compact, extending over $1.3'' \times 1.1''$. This corresponds to $9.2 \text{ kpc} \times 8.3 \text{ kpc}$ after deconvolution with the size of the seeing disk, which was exceptionally small for this data set, $0.6'' \times 0.5''$. We identify $[\text{OIII}]\lambda\lambda 4959, 5007$, $\text{H}\beta$, $\text{H}\alpha$, and $[\text{NII}]\lambda 6583$ in the integrated spectrum shown in Fig. A.1. The line properties are also listed in Table A.5.

In spite of the low spatial resolution of the data, we do detect a velocity gradient of 700 km s^{-1} from north-west to south-east, and potentially a gradient in FWHM line width of 1200 km s^{-1} to 500 km s^{-1} from the center to the periphery of the emission-line region. The low spatial resolution implies that we may be underestimating the intrinsic velocity gradient by about a factor 2 (C. Collet, 2014, PhD thesis). The velocity gradient is well aligned with the direction of the radio jets in TXS 1113–178 (Fig. A.5), although we do not see extended gas. This could be the consequence of the short exposure time for this source.

A.13. 3C 257

3C 257 at $z=2.48$ has extended line emission along an axis going from the north-west to the south-east, extending over $3.4'' \times 2.0''$ ($27.5 \text{ kpc} \times 15.1 \text{ kpc}$ after deconvolving with the size of the seeing disk of $0.8'' \times 0.7''$). The continuum emission is extended with a peak towards south and an extended fainter area towards north-west, roughly aligned with the emission-line gas (contours in Fig. A.4). The line emission is much brighter in the south-east, and is clearly spatially offset from the continuum.

The integrated spectrum shows $[\text{OIII}]\lambda\lambda 4959, 5007$, $\text{H}\beta$, and $\text{H}\alpha$, $[\text{NII}]\lambda 6583$, and $[\text{SII}]\lambda\lambda 6716, 6731$, where the two lines of the $[\text{SII}]$ doublet are blended. A single Gaussian component per line with $\text{FWHM} = 1049 \pm 7 \text{ km s}^{-1}$ is sufficient to fit the line profiles (the error is that of $[\text{OIII}]\lambda 5007$). The spectrum is shown in Fig. A.1 and all line properties are summarized in Table A.5.

The velocity field of 3C 257 is irregular (Fig. A.4), with a velocity maximum south-west from the center, and declining velocities towards either end of the emission-line region. The total velocity offset is 400 km s^{-1} . FWHMs are between 500 and 1300 km s^{-1} . The highest FWHMs are reached in the eastern part of the region, partially coinciding with the most strongly redshifted gas, but extending over a larger region. The region of highest velocities and FWHMs is almost, but not quite, associated with the relatively compact, double-lobed radio source (Fig. A.5), that is embedded in the gas. The highest velocities are reached just south of the two jets.

A.14. USS 1243+036

USS 1243+036 at $z=2.36$ is one of the galaxies with very extended line emission in our sample. Overall, we detect $\text{H}\beta$ and $[\text{OIII}]\lambda\lambda 4959, 5007$, as well as $\text{H}\alpha$, $[\text{NII}]\lambda 6583$, and

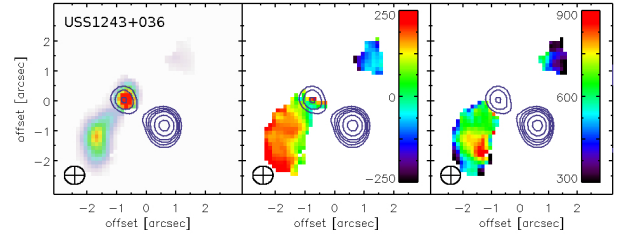


Fig. A.10. Maps of USS1243+036 highlighting the kinematics within the extended emission-line gas. Contours show the rest-frame optical continuum morphology. The very high-velocity gas in the central galaxy is not shown (see Fig. A.4 for a figure showing the full dynamic range in USS1243+036).

$[\text{SII}]\lambda\lambda 6716, 6731$. The integrated spectrum is shown in Fig. A.1 and the line properties are listed in Table A.5.

The projected size of the emission-line region is $5.3'' \times 0.9''$ (corresponding to $38 \text{ kpc} \times 4 \text{ kpc}$ after deconvolution with the seeing disk), and the emission-line morphology is very irregular. The nucleus as probed by the continuum emission is roughly centered within a resolved inner emission line region, but surrounded by two more extended emission-line blobs towards the north-west and south-east, which are very different from each other. An extended plume is found in the south-east, whereas in the north-west we only find a small, nearly unresolved region of bright line emission. The region where the jet is escaping from the emission-line region (first noted by van Ojik et al. 1996) shows particularly large velocity dispersions and a strong blueshift, as expected for regions of strong interactions between jet and gas.

To ensure that we are not missing flux in this region owing to the small field of view of SINFONI of only $8'' \times 8''$, we produced a mosaic from two pointings used for this galaxy and obtained in two different runs (Table 1), finding that our first observation did not miss any of the emission-line gas.

Velocities and FWHM line widths in USS1243+036 have an exceptionally large dynamic range, which is why we present two sets of $[\text{OIII}]\lambda 5007$ line maps in Fig. A.5, which only differ in their dynamic range for the line widths and velocity gradients. The maps show the mosaic from both pointings. The velocity gradient in the extended gas (lower panel of Fig. A.5) is $\sim 500 \text{ km s}^{-1}$ between the south-eastern and north-western lobe, with a monotonic velocity increase from the north-west to the south-east. The south-eastern lobe has broader lines, $\text{FWHM} = 700\text{--}900 \text{ km s}^{-1}$ than the north-western lobe, which has $\text{FWHM} \sim 300 \text{ km s}^{-1}$. Near the continuum location, velocities are up to 2500 km s^{-1} , and line widths are up to $\text{FWHM} = 900 \text{ km s}^{-1}$.

The right panel of Fig. A.5 shows that the southern radio hotspot is associated with the most strongly blueshifted gas in the southern emission-line region, and the region of broadest line widths. The radio plasma extends further outside the emission-line region. van Ojik et al. (1996) already identified this area as the site where the jet is being deflected. The northern radio lobe falls right next to the northern emission-line region.

The bright continuum emitter west-south-west from the galaxy has a featureless continuum consistent with a black body. We suspect it is a foreground star.

A.15. MG 1251+1104

MG 1251+1104 at $z=2.32$ is a rather compact line emitter, for which we have only shallow data with 2400 s of on-source exposure time with an average seeing of $\text{FWHM}=0.8'' \times 0.8''$. The FWHM size of the line image is $0.9''$, observed at a seeing of $\text{FWHM}=0.8''$. This corresponds to an upper limit on the size of 7.4 kpc. In the integrated spectrum we detect $[\text{OIII}]\lambda 5007$, $\text{H}\alpha$, and $[\text{NII}]\lambda 6583$. The latter two lines are blended owing to the broad line widths of $\text{FWHM}=914 \pm 32 \text{ km s}^{-1}$.

Fig. A.4 shows the morphology, velocity offsets and FWHMs. We caution that the range in velocity and FWHMs that we can detect in this source are likely very small compared to the intrinsic values because of the compactness of the source. While we do not detect a large velocity offset, to the north-west and south-east from the nucleus there appears to be a zone of more redshifted line emission, with a total velocity offset of 200 km s^{-1} relative to the most blueshifted gas. Line widths are up to 1300 km s^{-1} near the center and decrease to 500 km s^{-1} at the periphery. We cannot exclude that deeper observations would have revealed fainter extended line emission. For MG 1251+1104, we do not have a high-resolution radio image available. De Breuck et al. (2000) list it as a compact source with $\text{LAS} < 1.2''$, which corresponds roughly to the size of the emission-line region.

A.16. MRC 1324–262

MRC 1324–262 at $z=2.28$ is another source for which we only have shallow data with an on-source exposure time of 2400 s and seeing of $1.1'' \times 1.1''$. The $[\text{OIII}]\lambda 5007$ line is bright, well detected, and fairly broad, with $\text{FWHM}=1253 \pm 36 \text{ km s}^{-1}$. We also detect $\text{H}\alpha$, $\text{H}\beta$, and $[\text{SII}]\lambda\lambda 6716, 6731$. The lines of the $[\text{SII}]$ doublet are blended due to their large intrinsic line widths and low signal-to-noise ratio of the data. The integrated spectrum is shown in Fig. A.1 and individual line properties are listed in Table A.5.

The source appears almost compact in this data set, perhaps with a slight extension in east-western direction. The continuum is not detected (Fig. A.4). We do not detect any distinctive features in the velocity map, and given the large seeing and shallow data set, irregularities in the map of FWHM line widths could be dominated by noise. The radio maps shown in Fig. A.5 show a small double source, where each radio hotspot is near the outer edge of the emission line region.

A.17. TN J1338-1942

The second-highest redshift galaxy in our sample at $z=4.1$. Unfortunately, TN J1338–1942 falls at a somewhat difficult redshift for NIR observations, where the bright $[\text{OIII}]\lambda\lambda 4959, 5007$ and $\text{H}\alpha$ lines are at wavelengths redward of the K-band. $[\text{OII}]\lambda 3737$ falls into the spectral region of low atmospheric transmission between the H and K band and $[\text{NeIII}]\lambda 3869$ falls into the blue part of the K-band at $\lambda \sim 2 \mu\text{m}$.

We caution that due to the faintness of the lines, the uncertainties of relative velocities and line widths are high. We therefore extracted two spectra centered on the relative bright emission towards the north and south of the emission-line image in Fig. A.6. These spectra are shown in Fig. A.11. We identify $[\text{OII}]\lambda 3869$ in both regions, and $[\text{NeIII}]\lambda 3938$ in the northern spectrum.

In spite of these challenges we detect TN J1338–1942 in $[\text{NeIII}]\lambda\lambda 3869, 3968$ and in $[\text{OII}]\lambda 3727$. The brightest line is

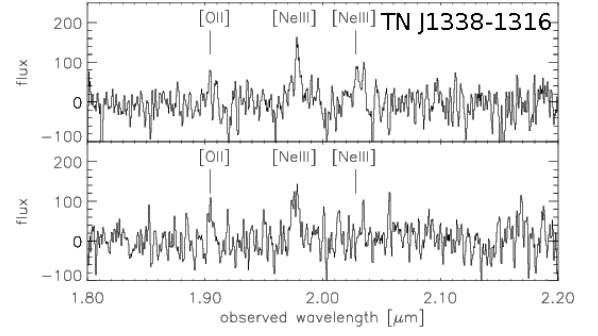


Fig. A.11. Integrated spectrum of TN J1338-1942 showing $[\text{OII}]\lambda 3869$, and $[\text{NeIII}]\lambda\lambda 3869, 3968$.

$[\text{NeIII}]\lambda 3869$, which we also resolve spatially (Fig. A.5). Line emission extends over $\sim 1.5''$ and matches the size and orientation of the $\text{Ly}\alpha$ and continuum emission of Zirm et al. (2005), which is embedded in a $>100 \text{ kpc}$, highly asymmetric $\text{Ly}\alpha$ halo (Venemans et al. 2002). The S/N of the line emission is very low, but suggests a velocity gradient of order 500 km s^{-1} , and very faint line emission with a velocity offset of 500 km s^{-1} towards west. At this position, Zirm et al. (2005) previously found a wedge-shaped feature in their *HST* narrow-band $\text{Ly}\alpha$ image. The radio morphology of TN J1338–1942 is compact. The nucleus is found just east of this wedge, and coincides with the area of highest FWHMs.

A.18. USS 1410–001

USS 1410–011 at $z=2.36$ is another source with a particularly large emission-line region (Fig. A.4) extending over an area of $5.6'' \times 2''$ along the major and minor axis, respectively (corresponding to $41 \text{ kpc} \times 14 \text{ kpc}$ after deconvolving with the size of the seeing disk). $[\text{OIII}]\lambda\lambda 4959, 5007$ and $\text{H}\alpha$ line emission extends nearly along an axis going from south to north with a monotonically increasing velocity gradient of $\Delta v = 685 \text{ km s}^{-1}$. Line widths are $\text{FWHM} = 400 - 900 \text{ km s}^{-1}$, except in a small region to the north-east of the nucleus where FWHMs up to 1300 km s^{-1} are reached. All lines are well fit with single Gaussian components. The continuum is compact and approximately centered on the line-emitting clouds.

The $[\text{NII}]\lambda 6583/\text{H}\alpha$ ratio is fairly low, $[\text{NII}]\lambda 6583/\text{H}\alpha = 0.17 \pm 0.02$. We also detect the $[\text{SII}]\lambda\lambda 6716, 6731$ doublet at good S/N and identify each line of the doublet individually, but no $[\text{OI}]\lambda 6300$. The 3σ upper limit on the $[\text{OI}]\lambda 6300$ flux is $2.4 \times 10^{-16} \text{ erg s}^{-1} \text{ cm}^{-2}$ assuming a line width of $\text{FWHM}=500 \text{ km s}^{-1}$. $[\text{OI}]\lambda 6300$ coincides with a bright night sky line residual. The $[\text{OIII}]\lambda 5007$ line in the integrated spectrum shows a faint blue wing.

USS 1410–011 has a very large radio source with $\text{LAS}=25.2''$ significantly more extended than the emission-line gas (Fig. A.12). Apart from the compact radio core, we do not detect radio continuum associated with the emission-line gas. The northern radio source shows extended faint emission along an axis that is associated with the region of the most redshifted line emission in the northern emission-line region of USS 1410–011.

A.19. MRC 1558–003

MRC 1558–003 at $z=2.53$ is one of the 6 galaxies of Nesvadba et al. (2011b) which have broad nuclear $\text{H}\alpha$ line emission

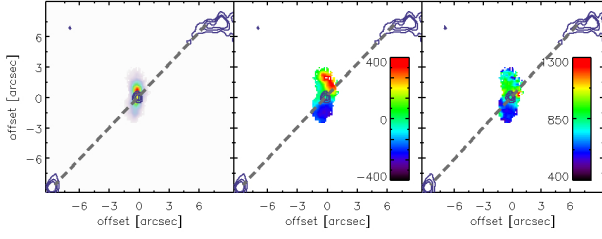


Fig. A.12. *left to right:* [OIII] morphologies, velocity offsets and FWHM line widths in USS1410–011 in comparison with the radio morphology. The northern radio source shows a narrow, faint morphology along an axis that is roughly an extension with the most redshifted gas in the northern emission-line region, before turning towards east at the hotspot.

heralding a direct sight line into the AGN. We removed the nuclear point source before fitting the extended line emission (§3.2). We find that the extended emission-line nebula is roughly centered on the nucleus with a size of $5.1'' \times 2.8''$ ($41 \text{ kpc} \times 22 \text{ kpc}$ at $z=2.53$ and after deconvolving with the seeing disk) along the major and minor axis with complex kinematics. Relative velocities peak in a region south from the nucleus with 500 km s^{-1} , blueshifts with up to -500 km s^{-1} are found in the periphery of the emission-line gas. The largest widths are found along a ridge south of the nucleus with $\text{FWHM}=1200 \text{ km s}^{-1}$. Most line emission has widths of about $\text{FWHM}=700\text{--}900 \text{ km s}^{-1}$.

MRC 1558–003 is also extended in the radio, with $\text{LAS}=7.7''$. The right panel of Fig. A.6 shows a faint extension from the radio core towards the western lobe, which is associated with the most strongly redshifted gas, although this does not stand out through particularly broad FWHMs in this case. We caution that this could also be a consequence of the removal of broad-line emission from the AGN.

A.20. USS 1707+105 (4C+10.48)

USS 1707+105 at $z=2.35$ is another source with very asymmetric line emission. We detected well extended line emission ($3.5'' \times 1.6''$), corresponding to a deconvolved size of $25 \text{ kpc} \times 5 \text{ kpc}$, extending from the nucleus to the north-east. We did not detect continuum emission in our data, but the size of the emission-line region is sufficiently large that we can safely place the nucleus near the southern edge of the extended emission-line region. No line emission is detected in the south-west, although this area is well covered by our data cube, with the same depth as the northern emission-line region. The northern region is nearly straight out to a distance of 20 kpc from the nuclear region, and then makes a sudden bent towards the south-east.

The velocity field is irregular with several velocity maxima and minima. The largest velocity gradient of 800 km s^{-1} is found in a small region 1.5 kpc from the nucleus. FWHMs are greatest in the near-nuclear region (1900 km s^{-1}), and are $800\text{--}1200 \text{ km s}^{-1}$ in the region associated with the large velocity gradient, and about $400\text{--}500 \text{ km s}^{-1}$ in the emission-line region beyond the bent.

On larger scales, the velocity offset is 490 km s^{-1} . We only detect [OIII] $\lambda 4959, 5007$, H α , [NII] $\lambda 6583$, and H β . [OI] $\lambda 6300$ and [SII] $\lambda \lambda 6716, 6731$ are too faint and in bad regions of the night sky.

A.21. 3C 362 (MG 1747+182)

The warm ionized gas in MG 1747+182 at $z=2.29$ extends over $4.0'' \times 2.2''$ along the major and minor axis, respectively (corresponding to a deconvolved size of $31 \times 15 \text{ kpc}$ at $z=2.29$). The emission-line gas extends along a north-east to south-west axis. The integrated spectrum (Fig. A.1) shows [OIII] $\lambda \lambda 4959, 5007$, H β , H α , [NII] $\lambda 6583$, and [SII] $\lambda \lambda 6716, 6731$. The two components of the [SII] doublet are blended because of the large line width of 980 km s^{-1} in the integrated spectrum. H α and [NII] $\lambda \lambda 6548, 6583$ are also strongly blended. Table A.5 gives the line properties derived from a single-Gaussian fit (which is adequate for the lines that are not blended) and by assuming that all lines have the same FWHM measured from [OIII] $\lambda 5007$.

The total velocity gradient of [OIII] $\lambda 5007$ in MG 1747+182 is about 600 km s^{-1} , and the velocity field is not very regular. We find a redshifted peak at about 8 kpc from the center of the emission-line region, and velocity minima are found near the north-eastern and south-western edge of line emission with velocities of about -300 km s^{-1} each. The line widths are highest in the south-west ($\text{FWHM} \sim 1500 \text{ km s}^{-1}$), and about 1000 km s^{-1} in other parts of the gas, with two dips ($\text{FWHM} \sim 500 \text{ km s}^{-1}$) north and south from the center. We do not detect the continuum from this source. The source has two radio lobes that are detected outside of the emission-line gas, delineating a jet axis that is well aligned with the major axis of the emission-line gas (Fig. A.6).

A.22. MP J1758–6738

The emission-line morphology of MP J1758-6738 at $z=2.03$ is dominated by a resolved, nearly circular, high-surface brightness region with a diameter of $2.4''$ centered on the nucleus (which we associated with the continuum source), and a fainter extension towards east (Fig. A.6). The velocity offset between these two regions is about 800 km s^{-1} , and velocities are fairly uniform (with offsets $\leq 100 \text{ km s}^{-1}$) within each region. FWHM line widths are of-order $700\text{--}800 \text{ km s}^{-1}$ throughout the central regions of the source, and narrower ($500\text{--}600 \text{ km s}^{-1}$) near the very periphery of the faint emission-line region.

At $z=2.03$, H β and [OIII] $\lambda 4959$ fall outside the H-band, and we only detect [OIII] $\lambda 5007$, H α , [NII] $\lambda 6583$, and [SII] $\lambda \lambda 6716, 6731$ (Fig. A.6). With $\text{FWHM} \sim 600 \text{ km s}^{-1}$, the H α and [NII] $\lambda 6583$ lines and the two lines of the [SII] doublet are blended, but can nonetheless be individually identified.

We only have a low-resolution radio map of this source with a $24''$ beam (Table 2), which shows two hotspots well outside the emission-line gas, and roughly aligned with the major axis of the gas.

A.23. TN J2007–1316

TN J2007–1316 at $z=3.8$ is amongst our highest-redshift sources. Our integrated spectrum covers [OII] $\lambda 3727$, [OIII] $\lambda \lambda 4363, 4959, 5007$, and H β (Fig. A.1). The results of individual line fits are given in Table A.5.

Line emission is compact at a spatial resolution of $0.9'' \times 0.8''$. We find a small velocity gradient of 100 km s^{-1} , which may underestimate the intrinsic velocity gradient by about a factor 2 due to beam-smearing effects (C. Collet, 2014, PhD thesis.) The line width in the integrated spectrum, $\text{FWHM}=950 \text{ km s}^{-1}$ corresponds to the FWHM found also in the map of Fig. A.4. The radio source shows two extended lobes with a relative distance of $3.3''$. The northern side shows a faint,

linear, narrow extension between the periphery of the emission-line gas and the radio hotspot. The axis of the radio source is well aligned with the major axis of the emission-line gas, and nearly perpendicular to the small velocity gradient seen in the gas. TN J2007–1316 is one of the galaxies discussed in Drouart et al. (2014) and Rocca-Volmerange et al. (2013) with a high star formation rate.

A.24. MRC 2025-218

MRC 2025-218 at $z=2.63$ has a bright nuclear point source and broad $H\alpha$ line emission originating from the AGN. Humphrey et al. (2008) found a deep neutral absorber on top of the $Ly\alpha$ line emission, which appears to be kinematically detached from the extended emission-line region, and probably probes a massive reservoir of either infalling or outflowing gas. We used the approach described in §3.2 to remove the nuclear component before fitting the extended line emission. The remaining emission-line region is extended with a size of $4.75'' \times 2.25''$, corresponding to a deconvolved size of $37 \text{ kpc} \times 16 \text{ kpc}$. The source has two bright radio hotspots just outside the emission-line gas, and an axis between them which aligns well with the major axis of the emission line gas. The radio core is not detected. The nucleus traced by the bright point source associated with the broad $H\alpha$ line is slightly south from the center of the emission-line region. The gas kinematics are irregular, with a total velocity offset of 900 km s^{-1} . The highest redshifts are found about $0.5''$ north from the nucleus. The lowest redshifts extend from the nucleus towards south. The FWHM line widths are between 700 and 1600 km s^{-1} , and the highest velocities are found in two regions, one centered on the nucleus, the other near the periphery of the northern emission-line gas. These widths are greater than those of the $H\alpha$ broad-line region, 8024 km s^{-1} (Nesvadba et al. 2011b), so that we do not think that they are residuals from the nuclear broad-line subtraction.

The integrated spectrum of MRC 2025-218 is shown in Fig. A.1. We identify $[\text{OIII}]\lambda\lambda 4959, 5007$, $H\alpha$, $[\text{NII}]\lambda 6583$, and $[\text{OI}]\lambda 6300$ with widths between 500 km s^{-1} (for $[\text{OI}]\lambda 6300$) and 1100 km s^{-1} (for $[\text{OIII}]\lambda\lambda 4959, 5007$ and $[\text{NII}]\lambda 6583$). The low width of the $[\text{OI}]$ line could be due to the faintness of the line, which is detected only at 4σ . The $[\text{SII}]\lambda\lambda 6716, 6731$ doublet falls beyond $2.4 \mu\text{m}$ at $z=2.63$, and is therefore not covered by our data set.

A.25. MG 2037–0011

MG 2037–0011 is a compact radio source at $z=1.51$ ($\text{LAS} < 0.2''$), which we observed with the J and H-band gratings at $R=2000$ and $R=3000$, respectively. The integrated spectrum (Fig. A.1) is dominated by bright and broad $H\alpha$ and $[\text{OIII}]\lambda\lambda 4959, 5007$ line emission, and we also detect $H\beta$ and $[\text{SII}]\lambda\lambda 6716, 6731$. $H\alpha$ is heavily blended with $[\text{NII}]\lambda 6583$, and the two components of the $[\text{SII}]\lambda\lambda 6716, 6731$ doublet with each other. The line width derived from the $[\text{OIII}]\lambda\lambda 4959, 5007$ doublet in the integrated spectrum is $\text{FWHM} = 802 \pm 25 \text{ km s}^{-1}$, and we obtain adequate fits when imposing the same width on the blended lines.

The emission-line morphology of $[\text{OIII}]\lambda 5007$ is compact, but we do see a small velocity gradient of 300 km s^{-1} going from north-east to south-west. This gradient may be smaller by about a factor 2 than the intrinsic gradient because of beam-smearing effects (C. Collet, 2014, PhD thesis). The line widths measured in the map are between 1200 – 1500 km s^{-1} .

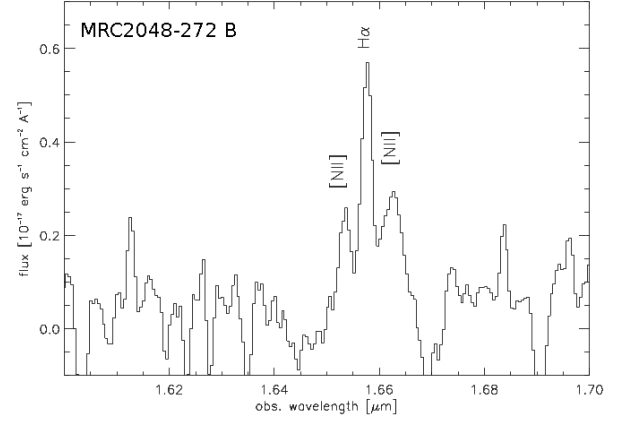


Fig. A.13. Integrated spectrum of the intervening $z=1.52$ galaxy found near MRC 2048-272.

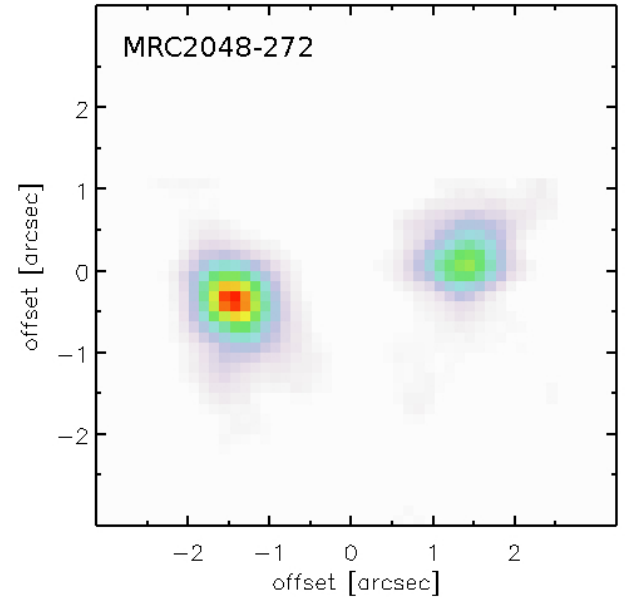


Fig. A.14. Continuum image of MRC 2048–272 and the intervening galaxy at $z=1.5$.

A.26. MRC 2048-272

MRC 2048–272 at $z=2.06$ has a relatively powerful ($\log P_{500} = 28.7 \text{ W Hz}^{-1}$) radio source with a size of $6.7''$. We did not detect any line emission, presumably because of deep telluric absorption features at the redshifted wavelength of $[\text{OIII}]\lambda 5007$ and $H\alpha$. $H\beta$ and $[\text{OIII}]\lambda 4959$ fall on top of bright night sky lines. We will therefore not discuss this galaxy any further.

Interesting however is that a second galaxy at redshift $z=1.52$ falls into the field of view (see the continuum image in Fig. A.14), for which we detect $H\alpha$ and $[\text{NII}]\lambda\lambda 6548, 6583$ in the H-band (Tab. A.5 and Fig. A.13). Obviously, the large redshift difference rules out that the two galaxies are physically related. This second galaxy appears to be the source of the bright far-infrared emission detected with Herschel (Drouart et al. 2014).

A.27. MRC 2104-242

MRC2104–242 at $z=2.49$ has one of the most extended radio sources in our sample, with a size of $21.8''$, corresponding to 176.6 kpc at $z=2.49$. We observed this galaxy during run 079.A-0617, in parts with adaptive optics, taking advantage of a nearby bright star, which we used for the tip-tilt correction. We obtained data cubes in the H and K-band individually, detecting [OIII] $\lambda\lambda 4959, 5007$, H β , H α , [NII] $\lambda\lambda 6548, 6583$, and the [SII] $\lambda\lambda 6716, 6731$ doublet. At a line width of FWHM=633 km s $^{-1}$, H α is partially blended with [NII] $\lambda\lambda 6548, 6583$, and the two lines of the [SII] $\lambda\lambda 6716, 6731$ doublet with each other. Single-component fits were sufficient to obtain adequate line fits (Fig. A.1). Fit results are listed in Table A.5.

The [OIII] $\lambda 5007$ line image in Fig. A.4 shows two gas blobs, and only the southern blob is associated with continuum emission. The northern blob has however a very high [OIII] $\lambda 5007$ /H α ratio, which is not consistent with gas heated by star formation and suggests that this source is a gas cloud that is illuminated by the AGN of MRC 2104-242. We find a regular velocity gradient in the southern cloud with a total velocity offset of 350 km s $^{-1}$, and little variation in velocity in the northern blob. The FWHM line widths are relatively narrow, about 500 km s $^{-1}$ in both clouds, with a broader region with FWHM up to 900 km s $^{-1}$ inbetween. The major axis of the overall emission-line region aligns well with the direction of the radio jets in the southern blob. The axis towards the northern hotspot intercepts the periphery of the northern cloud. The observed kinematics are consistent with those seen in Ly α with VIMOS by Villar-Martín et al. (2006), in particular the two bright components are also seen, and with a similar velocity offset.

A.28. 4C 23.56

4C 23.56 at $z=2.48$ is one of our most extended sources in the radio, with a size of $47''$, corresponding to 380 kpc. It is also one of the most powerful radio sources in our sample, with a radio power of $\log P_{500} = 28.9$ W Hz $^{-1}$ at 500 MHz in the rest-frame. The direction towards the radio hotspots is shown as a dashed line in the right panel of Fig. A.7. Comparing radio and X-ray observations, Blundell & Fabian (2011) argued that there has been a previous episode of radio activity in this source.

With SINFONI we detect [OIII] $\lambda\lambda 4959, 5007$, H α , H β , and [NII] $\lambda 6583$ in this source. Line widths in the integrated spectrum are between FWHM=500 and 600 km s $^{-1}$, and all lines are adequately fit with a single Gaussian component.

4C 23.56 was one of the first HzRGs where a biconal emission-line nebula was detected (Knopp & Chambers 1997). Line emission in our SINFONI cube is very extended in 4C 23.56, mostly along, but also perpendicular to the axis of the radio jet, and roughly centered on the continuum source, which we use as tracer of the nuclear regions. We find a velocity gradient of 1200 km s $^{-1}$ with the velocity monotonically increasing from the south-west to the north-east. The line widths are FWHM=700–1000 km s $^{-1}$ through most of the source, with lower widths of FWHM=400–500 km s $^{-1}$ in the periphery, including a faint extension towards north-east.

A.29. NVSS J2135–3337

NVSS J2135–3337 at $z=2.52$ was taken from the catalog of Broderick et al. (2007a) and Bryant et al. (2009) and is one of our galaxies with fairly moderate radio luminosity, $\log P_{500} = 27.9$ W Hz $^{-1}$ (Miley & De Breuck 2008). It has a bright,

$R=14.5$ mag star at a distance of only $16.9''$ which allows observations with adaptive optics. At a $250 \text{ mas} \times 125 \text{ mas}$ pixel scale this enabled us to reach a spatial resolution of FWHM= $0.4'' \times 0.4''$. Ionized line emission in NVSS2135–3337 is extended over $2.5'' \times 1.4''$, corresponding to 16.3 kpc \times 10.4 kpc after deconvolution with the size of the point spread function. We observed NVSS J2135–3337 individually in the H and K band at $R=3000$ and $R=4000$, respectively. The deep AO data were obtained in the K-band through program 381.A-0541.

Fig. A.7 shows the gas morphology and kinematics of NVSS J2135–3337, which was derived from H α in this case. The line emission is dominated by a centrally peaked component with a small extension towards the north-west. The total velocity offset is 600 km s $^{-1}$ along an axis that is going from the south-east to the north-west of the nucleus. The line widths peak near the nucleus with FWHM=1200 km s $^{-1}$, and with much lower widths of FWHM= 200 – 300 km s $^{-1}$ in the far periphery and in particular the faint northern extension. The radio source is compact and falls inbetween the regions with the most strongly blueshifted and redshifted gas, near the peak in FWHM line width.

A.30. MG J2144+1928

The gas morphology in MG 2144+1928 at $z=3.59$ is very unusual compared to the rest of the sample. [OIII] $\lambda 5007$ line emission extends over $9.1''$ along the major axis, with a very small minor axis of only $2.2''$. This corresponds to a size of 66 kpc \times 16 kpc. Fig. A.7 shows a relatively compact, but elongated central emission-line region, centered roughly on the continuum peak. Towards north and south, but offset from the central nebulousity, we find two gas plumes that are both not directly connected to the central nebulousity, but have very similar velocities. The line widths are also fairly uniform throughout the source, with FWHM ~ 800 km s $^{-1}$. Two unresolved radio hotspots are found right at the far end of each emission-line gas plume (Fig. A.7).

A.31. MRC 2224–273

MRC 2224–273 is a relatively small source at $z=1.7$, for which we only have shallow data. We detect line emission centered on the continuum peak with a size of $1.6'' \times 1.4''$, corresponding to a deconvolved size of 11 kpc \times 8 kpc. The integrated spectrum shows H α and [NII] $\lambda 6583$ (which are heavily blended at an integrated FWHM=1343 km s $^{-1}$), the [SII] $\lambda\lambda 6716, 6731$ doublet (the two components of the doublet are also strongly blended), and [OI] $\lambda 6300$. The radio source is compact with $\text{LAS} < 0.4''$.

A.32. TN J2254+1857

TN J2254+1857 at $z=2.15$ is one of our lower-power radio sources, with $\log P_{500} = 27.8$ W Hz $^{-1}$. [OIII] $\lambda 5007$ line emission is extended over $2.1'' \times 1.3''$, corresponding to a deconvolved size of 16.0 kpc \times 9.6 kpc. Relative velocities decrease monotonically from the south-west to the north-east with a total velocity offset of 500 km s $^{-1}$. FWHM line widths are very broad near the continuum peak, with FWHM= 1500 – 2000 km s $^{-1}$, and around 600 – 800 km s $^{-1}$ in the periphery. We show the emission-line maps in Fig. A.4. The integrated spectrum shown in Fig. A.1 shows broad (FWHM= 863 km s $^{-1}$) lines of [OIII] $\lambda\lambda 4959, 5007$, [SII] $\lambda\lambda 6716, 6731$,

and [OI] λ 6300. Properties of individual lines are listed in Table A.5.

The radio map shown in the right panel of Fig. A.8 shows a small double. The axis between the two radio hotspots is well aligned with the major axis of the emission-line region and with the velocity gradient. The two radio hotspots are right at the far end of the emission line regions.

A.33. MG 2308+0336

MG 2308+0336 at $z=2.46$ has a resolved, but relatively small radio source with a size of $3.6''$ (29 kpc at $z=2.46$). Line emission shown in Fig. A.8 fills the area between the two radio lobes (right panel of Fig. A.8). We did not detect the optical continuum in this source, but the emission-line surface brightness profile is very regular with a peak in the middle between the two radio lobes. We assume that this is approximately the position of the nucleus in MG 2308+0336.

The integrated spectrum of MG J2308+0336 shows $H\beta$, [OIII] $\lambda\lambda$ 4959,5007, [OI], $H\alpha$, [NII] λ 6583, and the [SII] $\lambda\lambda$ 6716,6731 doublet (Fig. A.1). Line properties are listed in Table A.5. All lines were adequately fit with a single Gaussian component of a common width $\text{FWHM}=750 \text{ km s}^{-1}$.

The kinematic maps show a monotonic velocity gradient of 800 km s^{-1} increasing from the south-south-east to the north-north-west. The FWHMs show that the lowest line widths are near the center, with $\text{FWHM}\sim 500\text{--}600 \text{ km s}^{-1}$, and a broadening at either end of the emission line region, near the radio lobes. In the north, FWHMs are up to 1000 km s^{-1} , and 1200 km s^{-1} in the south.

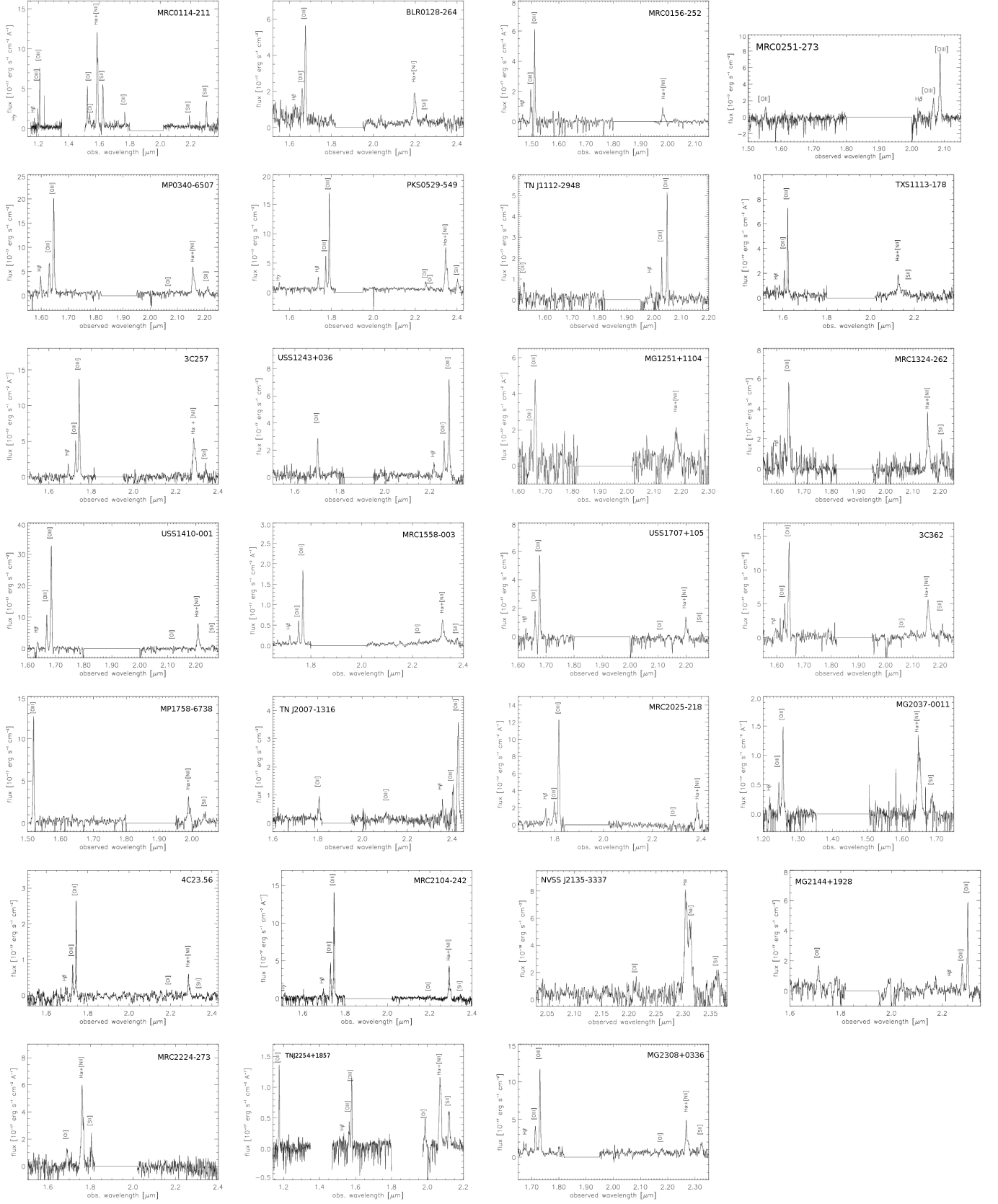


Fig. A.1. Integrated spectra of our galaxies.

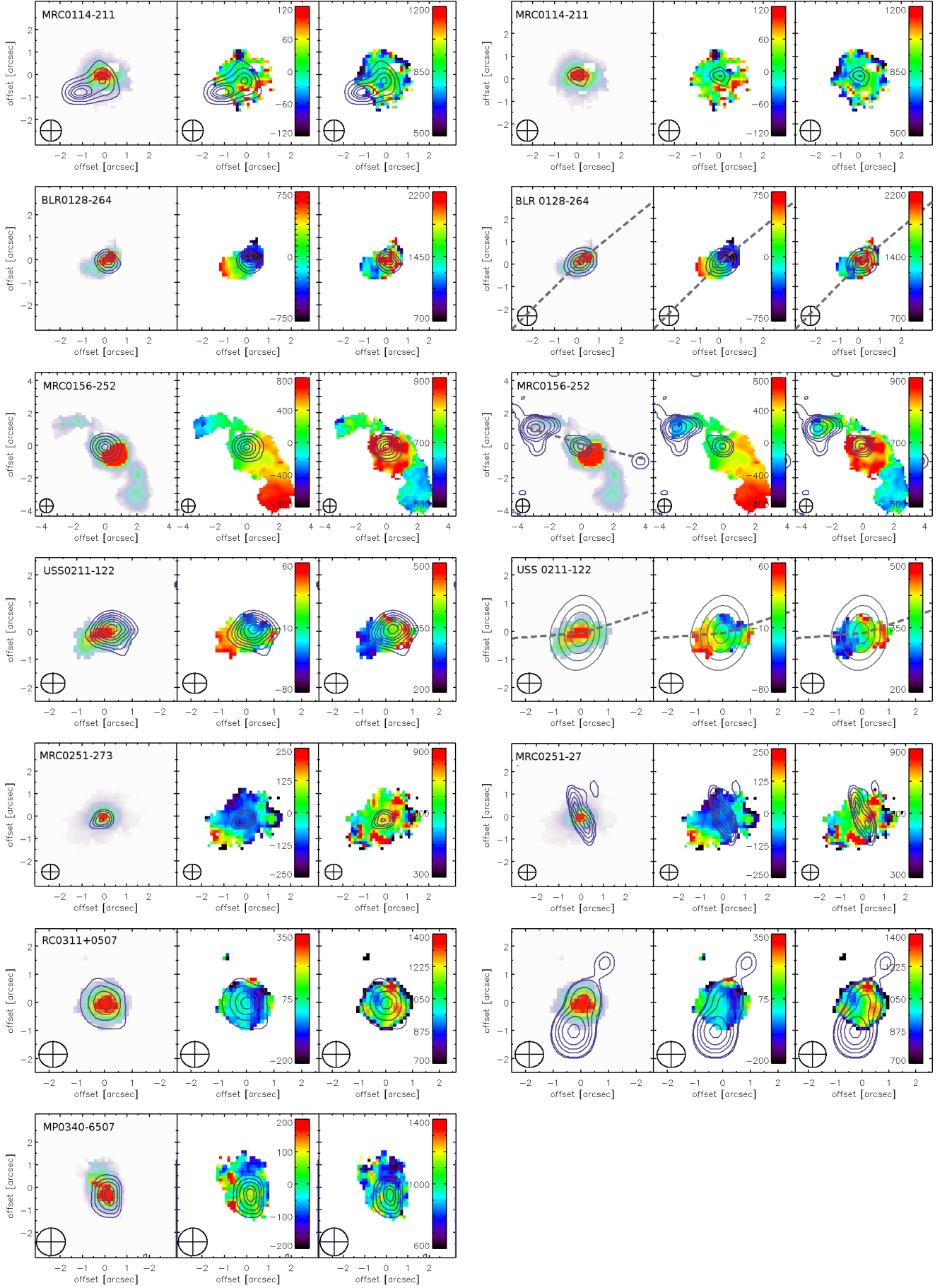


Fig. A.4. Maps of our galaxies in order of RA, with the rest-frame optical continuum shown as contours in the left, and the GHz radio continuum in the right panel. In each panel, maps show (from left to right) Emission-line morphology, velocities relative to the average redshift of all pixels covered by the emission-line region, and FWHM line width. Relative velocities and line widths are given in km s^{-1} . In galaxies where we did not detect the rest-frame optical continuum, we show the emission-line morphology instead of the optical continuum (with red contours, the continuum is shown as blue contours). Coordinates are given relative to the position listed in Table 1. Contour levels are arbitrary, their main purpose is to guide the eye.

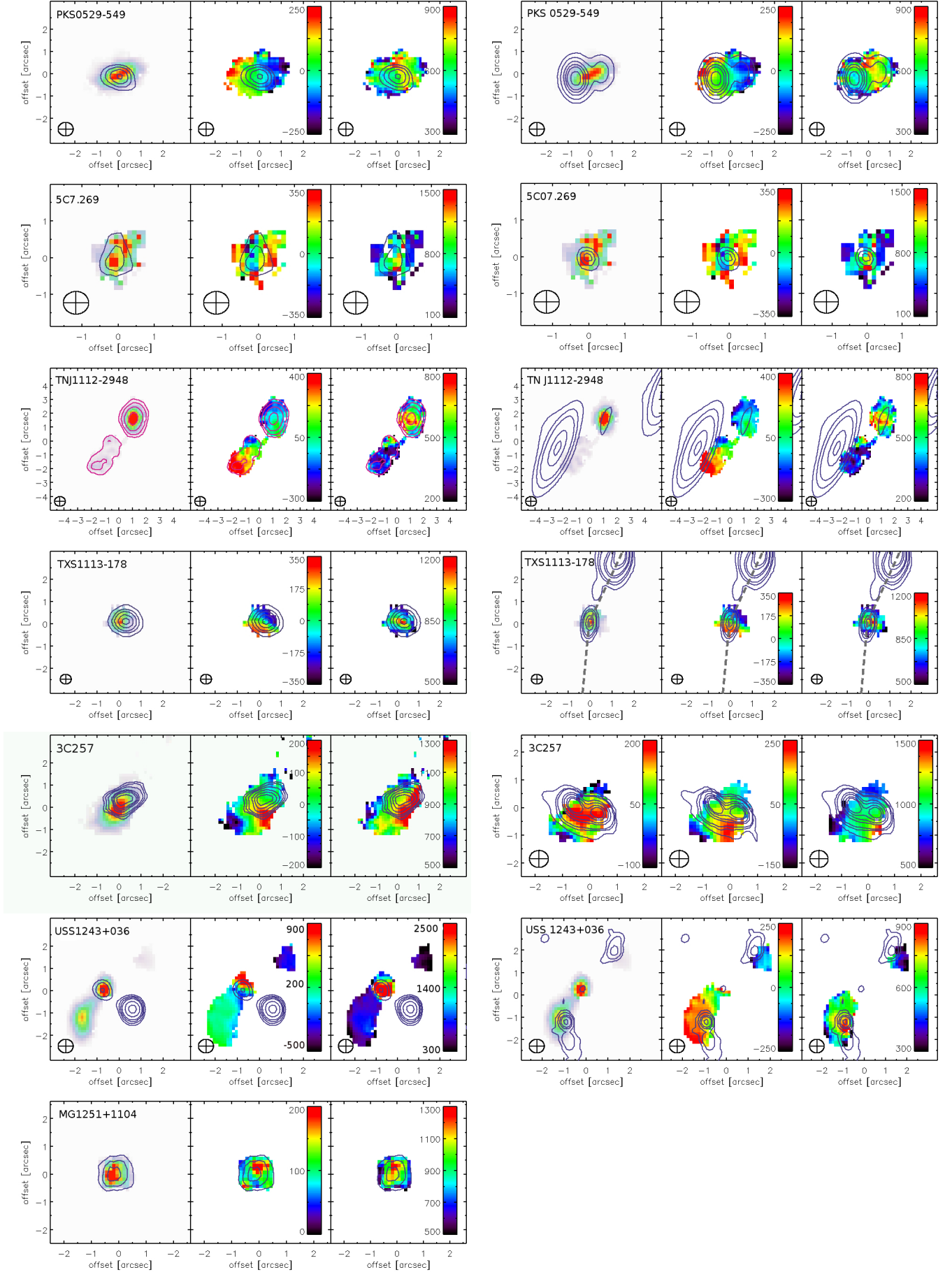


Fig. A.5. Maps of our galaxies in order of RA, with the rest-frame optical continuum shown as contours in the left, and the GHz radio continuum in the right panel. In each panel, maps show (from left to right) Emission-line morphology, velocities relative to the average redshift of all pixels covered by the emission-line region, and FWHM line width. Relative velocities and line widths are given in km s^{-1} . In galaxies where we did not detect the rest-frame optical continuum, we show the emission-line morphology instead of the optical continuum (with red contours, the continuum is shown as blue contours). Coordinates are given relative to the position listed in Table 1. Contour levels are arbitrary, their main purpose is to guide the eye. For MG1251+1104 we do not have a radio image available. It is listed as a point source with an upper limit to the source size of $1.2''$ in De Breuck et al. (2000).

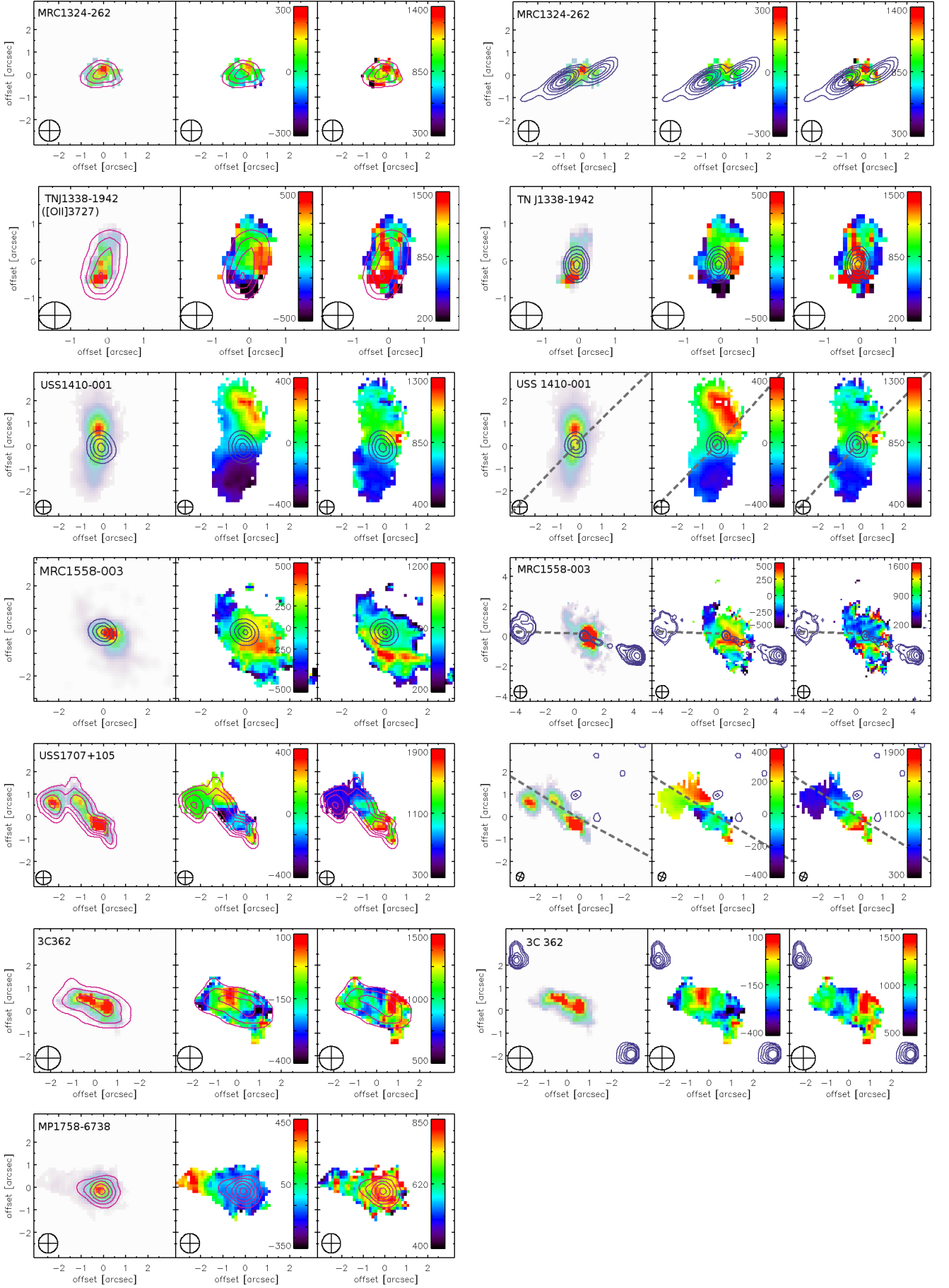


Fig. A.6. Maps of our galaxies in order of RA, with the rest-frame optical continuum shown as contours in the left, and the GHz radio continuum in the right panel. In each panel, maps show (from left to right) Emission-line morphology, velocities relative to the average redshift of all pixels covered by the emission-line region, and FWHM line width. Relative velocities and line widths are given in km s^{-1} . In galaxies where we did not detect the rest-frame optical continuum, we show the emission-line morphology instead of the optical continuum (with red contours, the continuum is shown as blue contours). Coordinates are given relative to the position listed in Table 1. Contour levels are arbitrary, their main purpose is to guide the eye. The radio map of MP 1758–6738 has a very large beam of $24.4''$ and is not shown.

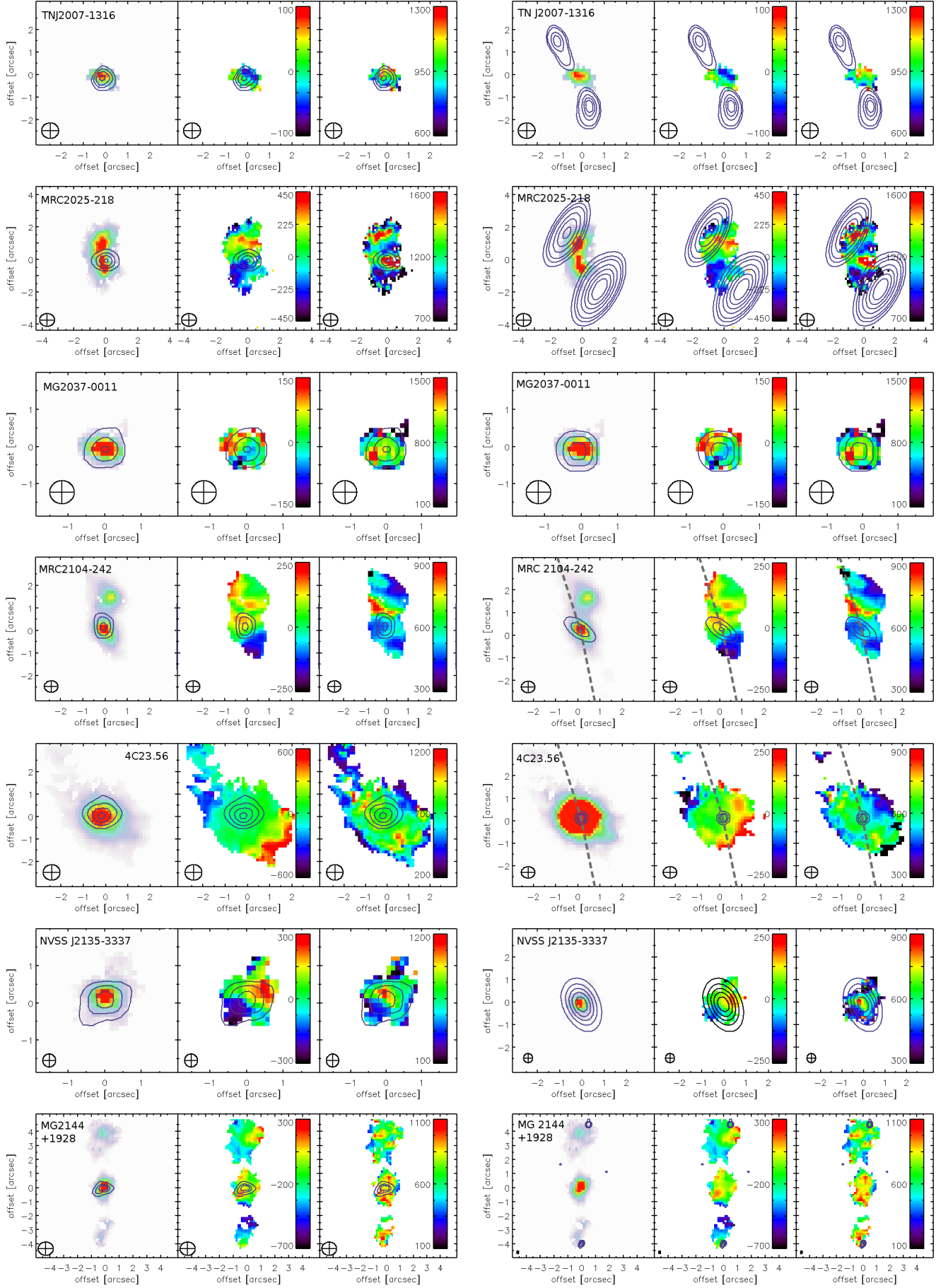


Fig. A.7. Maps of our galaxies in order of RA, with the rest-frame optical continuum shown as contours in the left, and the GHz radio continuum in the right panel. In each panel, maps show (from left to right) Emission-line morphology, velocities relative to the average redshift of all pixels covered by the emission-line region, and FWHM line width. Relative velocities and line widths are given in km s^{-1} . In galaxies where we did not detect the rest-frame optical continuum, we show the emission-line morphology instead of the optical continuum (with red contours, the continuum is shown as blue contours). Coordinates are given relative to the position listed in Table 1. Contour levels are arbitrary, their main purpose is to guide the eye. We have no good radio map of MRC 2224–273, but the source has been listed as compact by De Breuck et al. (2000) with an upper size limit of $0.4''$.

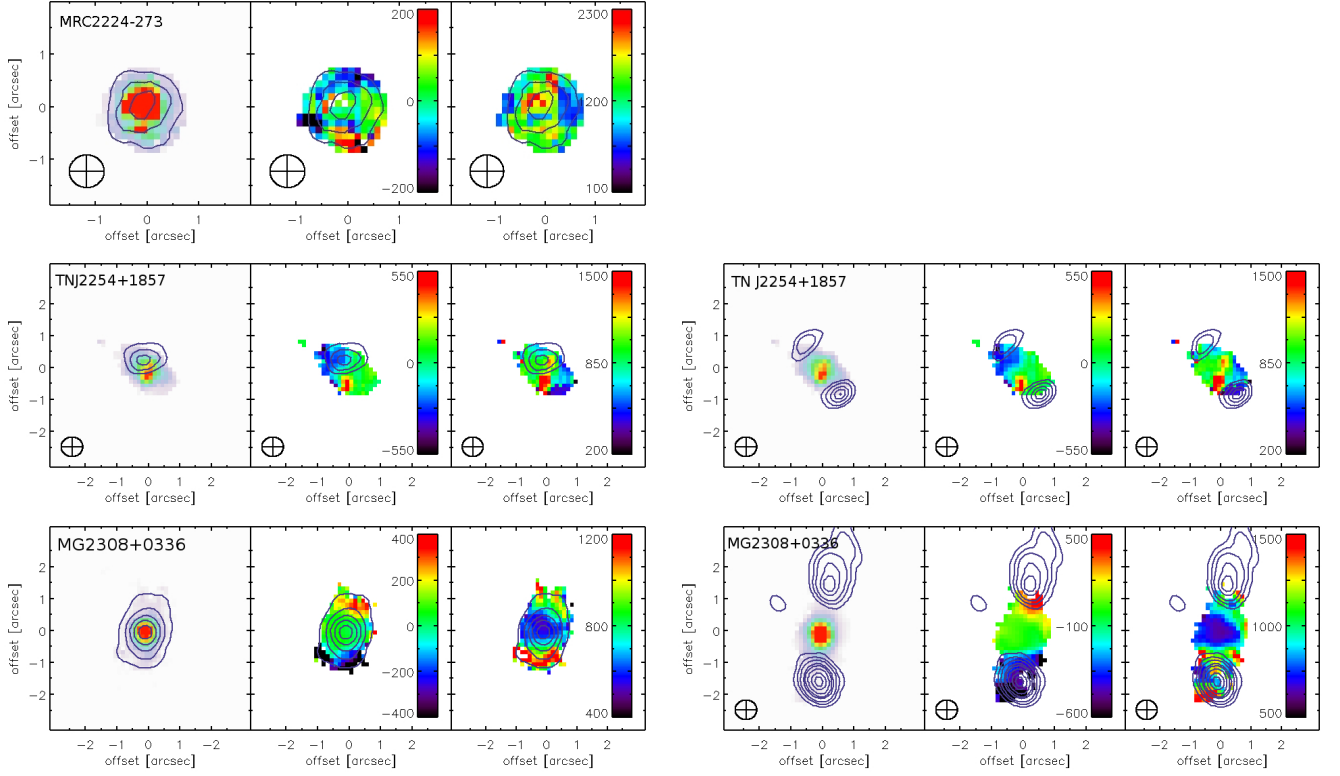


Fig. A.8. Maps of our galaxies in order of RA, with the rest-frame optical continuum shown as contours in the left, and the GHz radio continuum in the right panel. In each panel, maps show (from *left to right*) Emission-line morphology, velocities relative to the average redshift of all pixels covered by the emission-line region, and FWHM line width. Relative velocities and line widths are given in km s^{-1} . In galaxies where we did not detect the rest-frame optical continuum, we show the emission-line morphology instead of the optical continuum (with red contours, the continuum is shown as blue contours). Coordinates are given relative to the position listed in Table 1. Contour levels are arbitrary, their main purpose is to guide the eye.

Table A.5. Integrated spectral properties

Source	Line ID	λ_0 [Å]	λ_{obs} [Å]	redshift	FWHM [km s ⁻¹]	flux [10 ⁻¹⁶ erg s ⁻¹ cm ⁻²]
MRC 0114–211	[OIII]	5007	12093.3±0.1	1.41528±0.00002	673±6	22.6±0.4
	Hβ	4861	11741.6±0.8	1.41548±0.00015	673±46	2.92±0.4
	Hα	6563	15851.3±0.1	1.41526±0.00001	673±4	47.4±0.5
	[NII]	6583	15900.1±0.1	1.41533±0.00002	673±5	35.6±0.5
	[SII]	6716	16221.3±0.2	1.41533±0.00002	673±7	20.2±0.4
	[SII]	6731	16257.6±0.2	1.41533±0.00003	673±8	16.2±0.3
	[OI]	6300	15216.6±0.1	1.41533±0.00002	673±6	19.0±0.2
BLR 0128–264	[OIII]	5007	16756.3±0.5	2.34658±0.00009	1136±20	34.5±1.1
	Hβ	4861	16269.1±3.1	2.34686±0.00064	1136±140	4.9±1.1
	Hα	6563	21963.4±1.0	2.34655±0.00016	1136±33	12.1±0.7
	[NII]	6583	22031.0±1.8	2.34665±0.00027	1136±58	7.0±0.7
	[SII]	6716	22476.1±13.7	2.34665±0.00204	1136±90	1.0±0.8
	[SII]	6731	22526.3±5.0	2.34665±0.00074	1136±177	2.1±0.6
MRC 0156–252	[OIII]	5007	15112.3±0.2	2.01823±0.00004	621±9	208.9±5.7
	Hβ	4861	14672.8±3.9	2.01848±0.00080	621±207	12.6±6.8
	Hα	6563	19808.4±0.3	2.01820±0.00004	621±10	47.6±1.4
	[NII]	6583	19869.4±0.4	2.01829±0.0000	621±15	31.1±1.4
USS 0211–122	[OIII] _s	5007	16717.2±0.1	2.3387±0.0001	434±2	61.0±0.4
	[OIII] _n	5007	16694.5±0.1	2.3342±0.0001	275±1	45.1±0.4
	[OIII] _b	5007	16717.8±0.7	2.3388±0.0001	1380±29	16.0±0.7
	Hβ	4861	16231.1±0.6	2.3390±0.0001	434±20	5.6±0.4
	Hα	6563	21912.1±0.2	2.3387±0.0001	434±6	19.9±0.5
	[NII]	6583	21979.5±0.8	2.3388±0.0001	434±21	5.5±0.5
	[SII]	6716	22423.6±2.5	2.3388±0.0004	434±67	1.6±0.5
	[SII]	6731	22473.7±3.3	2.3388±0.0005	434±86	1.3±0.5
MRC 0251–273	[OIII]	5007	20859.2±0.3	3.16600±0.00005	681±9	39.9±0.9
	Hβ	4861	20252.6±4	3.16634±0.00084	681±145	2.6±1.0
	[OII]	3727	15522.8±63	3.16497±0.00150	681±287	3.2±3.1
	[OII]	3729	15534.5±6	3.16586±0.00150	681±287	3.2±3.1
RC J0311+0507	[OII] _n	3727	20536.0±0.5	4.5100±	112±19	12.2±1.6
	[OII] _n	3729	20557.2±0.6	4.5040±	112±20	11.7±1.6
	[OII] _b	3728	20518.9±5	4.5128±	1407±195	62.1±6.5
MP J0340–6507	[OIII]	5007	16456.4±0.1	2.28667±0.00002	829±5	94.3±1.1
	Hβ	4861	15977.8±0.8	2.28694±0.00016	829±36	14.9±1.2
	Hα	6563	21570.2±0.4	2.28664±0.00006	829±14	33.8±1.0
	[NII]	6583	21636.6±0.9	2.28674±0.00013	829±29	15.8±1.0
	[SII]	6716	22073.7±6.0	2.28674±0.00089	829±226	3.5±1.6
	[SII]	6731	22123.0±3.0	2.28674±0.00044	829±103	6.6±1.5
PKS 0529–549	[OIII]	5007	17896.46±0.04	2.57429±0.00001	693±2	72.4±0.3
	Hβ	4861	17376.0±0.3	2.57458±0.00007	693±13	9.9±0.3
	Hα	6563	23457.8±0.2	2.57425±0.00003	693±5	40.6±0.6
	[NII]	6583	23530.0±0.3	2.57436±0.00005	693±9	21.4±0.6
	[OI]	6300	22518.5±0.9	2.57436±0.00014	693±27	8.0±0.6
	[OI]	6363	22756.9±3	2.57644±0.00048	683±94	2.4±0.6
	Hγ	4340	15508.0±0.3	2.57327±0.00007	763±14	5.2±0.2
5C 07.269	[OIII]	5007	16148±5	2.22505±0.0010	1224±245	1.7±0.6
	Hα	6563	21157±4	2.22374±0.0007	2067±160	3.1±0.4
	[NII]	6583	21212±18	2.22219±0.0027	2475±754	1.15±0.6
	[SII]	6724	21676±22	2.22394±0.0033	2425±928	1.3±0.6
TN J1112–2948	[OIII]	5007	20480.7±0.2	3.09042±0.00004	393±6	16.4±0.4
	Hβ	4861	19885.2±1.9	3.09075±0.00039	393±64	1.5±0.4
	[OII]	3727	15241.2±1.9	3.08940±0.00052	393±85	1.4±0.5
	[OII]	3729	15252.7±3.5	3.09028±0.00093	393±157	0.8±1.0
TXS 1113–178	[OIII]	5007	16222.1±0.2	2.23989±0.00002	632±5	24.8±0.3
	Hβ	4861	15750.4±1.2	2.24015±0.00024	632±48	2.4±0.3
	Hα	6563	21263.2±0.5	2.23985±0.00008	632±16	8.3±0.4
	[NII]	6583	21328.6±1.0	2.23995±0.00015	632±29	4.5±0.4
3C 257	[OIII]	5007	17432.1±0.2	2.48154±0.00003	1049±7	87.2±1.0
	Hβ	4861	16925.1±1.5	2.48182±0.00032	1049±64	9.8±1.1

Table A.5. Integrated spectral properties (continued).

Source	Line ID	λ_0 [Å]	λ_{obs} [Å]	redshift	FWHM [km s ⁻¹]	flux [10 ⁻¹⁶ erg s ⁻¹ cm ⁻²]
USS 1243+036	H α	6563	22849.1±1.2	2.48150±0.00019	1049±38	35.2±2.4
	[NII]	6583	22919.4±1.8	2.48161±0.00027	1049±54	24.9±2.4
	[SII]	6716	23382.5±6.7	2.48161±0.00100	1049±223	6.7±2.5
	[SII]	6731	23434.7±9.3	2.48161±0.00138	1049±329	5.1±2.7
	[OIII]	5007	22860.6±0.2	3.56573±0.00005	670±7	28.7±0.5
MG 1251+1104	H β	4861	22195.8±2.9	3.56610±0.00060	670±87	2.8±0.7
	[OII]	3727	17012.3±1.6	3.56460±0.00042	670±62	5.6±0.9
	[OII]	3729	17025.0±1.6	3.56558±0.00042	670±62	5.6±0.9
	[OIII]	5007	16631.9±0.7	2.3217±0.0002	914±32	109±7
MRC 1324–262	H α	6563	21800.3±2.4	2.3217±0.0004	914±80	58±9
	[NII]	6583	21867.4±5.8	2.3218±0.0009	914±208	26±10
	[OIII]	5007	16438.1±0.9	2.2830±0.0002	1253±36	38.7±2.1
TN J1338–1942	H β	4861	15970.0±6.0	2.2853±0.0012	1022±283	5.034±2.4
	H α	6563	21540.5±1.1	2.2821±0.0002	594±37	15.0559±1.7
	[NII]	6583	21604.5±2.5	2.2819±0.0004	815±80	10.6862±1.9
	[NeIII]	3967.5	20293.3±4.9	4.115±0.001	842±118	6.2±1.0
USS 1410–001	[NeIII]	3868.8	19768.5±5.2	4.110±0.001	842±118	11.2±1.6
	[OII]	3727	19047.0±5.1	4.111±0.001	725±141	4.7±1.1
	[OIII]	5007	16843.2±0.1	2.36394±0.00002	710±3	144±1.2
	H β	4861	16356.5±1.1	2.36486±0.00023	678±46	9±1.1
MRC 1558–003	H α	6563	22075.8±0.2	2.36369±0.00003	711±6	46±0.8
	[NII]	6583	22147.0±1.3	2.36428±0.00019	748±40	8±0.8
	[SII]	6724	22588.5±2.5	2.36340±0.00038	824±84	7±1.0
	[OIII]	5007	17683.4±0.1	2.53173±0.00003	695±6	77.6±1.2
	H β	4861	17169.1±1.2	2.53202±0.00024	695±47	8.5±1.0
USS 1707+105	H α	6563	23178.5±0.4	2.53169±0.00007	695±13	34.9±1.2
	[NII]	6583	23249.8±0.9	2.53180±0.00013	695±25	17.9±1.2
	[SII]	6716	23719.6±5.2	2.53180±0.00077	695±164	3.5±1.4
	[SII]	6731	23772.5±2.6	2.53180±0.00039	695±77	6.5±1.3
	[OI]	6300	22250.3±2.4	2.53180±0.00038	695±76	4.7±0.9
	[OIII]	5007.00	16771.7±0.2	2.3497±0.00004	698±8	23.7±0.5
3C 362	H β	4861.00	16280.±1.3	2.3491±0.00026	297±46	1.4±0.4
	H α	6563.00	21991.7±0.8	2.3509±0.00012	641±23	7.0±0.5
	[NII]	6583.00	22062.±2.2	2.3513±0.00033	494±65	1.8±0.4
	[OIII]	5007	16449.5±0.2	2.28531±0.00003	982±6	77.2±0.9
MP 1758–6738	H β	4861	15971.2±4.2	2.28557±0.0009	982±200	3.1±1.0
	H α	6563	21561.2±0.4	2.28527±0.00007	982±15	32.8±0.9
	[NII]	6583	21627.6±1.4	2.28537±0.0002	982±47	10.7±0.9
	[SII]	6716	22064.6±3.0	2.28537±0.0005	982±100	7.0±1.3
	[OIII]	5007	15178.5±0.2	2.03145±0.00003	573±7	36.6±0.8
TN J2007–1316	H α	6563	19893.0±0.8	2.0311±0.0001	508±24	12±1.
	[NII]	6583	19949.3±1.3	2.0304±0.0002	601±41	9±1.
	[SII]	6716	20359.6±1.5	2.0315±0.0002	572±49	4.5±0.7
	[SII]	6731	20405.1±1.6	2.0315±0.0003	572±53	4.2±0.7
MRC 2025–218	[OIII]	5007	24260.6±0.3	3.84534±0.0006	950±10	28.9±0.5
	H β	4861	23555.1±1.6	3.84573±0.0009	950±50	5.5±0.5
	[OII]	3727	18067.6±0.9	3.84523±0.0003	950±35	4.3±0.3
MG 2037–0011	[OIII]	5007	18169.8±0.2	2.62889±0.00004	1037±7	79.25±1.0
	H α	6563	23817.4±1.4	2.62904±0.00022	819±43	17.15±1.6
	[NII]	6583	23885.0±2.5	2.62829±0.00038	1096±77	14.77±1.9
	[OI]	6300	22860.6±2.3	2.62867±0.00037	479±71	2.44±0.6
MRC 2048–272	[OIII]	5007	12571.5±0.5	1.51078±0.00009	802±25	5.0±0.3
	H α	6563	16478.1±0.9	1.51076±0.00014	802±39	5.4±0.5
	[NII]	6583	16528.8±0.9	1.51083±0.00014	802±38	5.5±0.5
	[SII]	6716	16862.8±2.4	1.51083±0.00036	802±99	1.8±0.4
	[SII]	6731	16900.4±2.5	1.51083±0.00037	802±102	1.8±0.4
MRC 2048–272	H α	6563	16576.7±1.0	1.52579±0.0002	468±40	1.5±2
	[NII]	6583	16626.1±1.7	1.52561±0.0003	466±70	0.9±2
	[NII]	6548	16534.2±2.9	1.52507±0.0004	470±119	0.6±3

Table A.5. Integrated spectral properties (continued).

Source	Line ID	λ_0 [Å]	λ_{obs} [Å]	redshift	FWHM [km s ⁻¹]	flux [10 ⁻¹⁶ erg s ⁻¹ cm ⁻²]
MRC 2104–242	[OIII]	5007	17482.5± 0.1	2.4916± 0.00002	633± 4	37.7± 0.4
	Hβ	4861	16975.2± 0.8	2.4921± 0.00017	491± 32	2.6± 0.3
	Hα	6563	22915.3± 0.3	2.4916± 0.00004	633± 8	22.0± 0.5
	[NII]	6583	22985.8± 0.9	2.4917± 0.00013	633± 25	7.0± 0.5
	[SII]	6716	23450.2± 3.4	2.4917± 0.00051	633± 105	2.2± 0.5
	[SII]	6731	23502.6±360	2.4917± 0.05359	633±2211	1.6±0.5
NVSS J2135-3337	Hα	6563	23052.6±0.5	2.51251±0.0001	637±15	3.2±0.13
	[NII]	6583	23123.5±0.5	2.51261±0.0001	637±16	2.9±0.13
	[SII]	6716	23590.7±2	2.51261±0.0003	637±52	0.9±0.13
	[SII]	6731	23643.4±2	2.51261±0.0003	637±62	0.8±0.13
	[OI]	6300	22129.5±3	2.51261±0.0006	1307±120	1.3±0.2
	[OIII]	5007	17440.6±0.3	2.48325±0.00006	629± 12	104.7±3.7
4C 23.56	Hβ	4861	16928.5±3.4	2.48251±0.00069	517±139	8.1±3.7
	Hα	6563	22862.6±0.8	2.48356±0.00012	575± 22	28.8±2.1
	[NII]	6583	22933.2±2.4	2.48369±0.00037	560± 67	9.5±2.1
	[OIII]	5007	23000.3± 0.4	3.59362±0.00008	651± 12	31±1
MG J2144+1928	Hβ	4861	22331.4± 21.	3.59400±0.00428	651± 842	1.7±2.5
	[OII]	3727	17116.2± 2.8	3.59248±0.00075	651± 118	4.2±1.4
	[OII]	3729	17129.0± 2.5	3.59347±0.00066	651± 102	4.9±1.3
	[OIII]	5007	23000.3± 0.4	3.59362±0.00008	651± 12	31±1
MRC 2224–273	Hα	6563	17605.6±0.9	1.68255±0.00014	1343± 36	34.0±1.7
	[NII]	6583	17659.8±1.7	1.68263±0.00025	1343± 68	18.4±1.7
	[SII]	6716	18016.7±6.4	1.68263±0.00095	1343±275	5.2±1.9
	[SII]	6731	18056.8±3.2	1.68263±0.00048	1343±132	9.8±1.7
	[OI]	6300	16900.6±2.7	1.68263±0.00043	1343±119	10.0±1.7
	[OIII]	5007	15787.8±0.8	2.1531±0.0002	863±36	5.4±0.4
TN J2254+1857	Hα	6563	20693.9±0.9	2.1531±0.0001	863±32	6.3±0.4
	[NII]	6583	20757.6±1.1	2.1532±0.0002	863±39	5.2±0.4
	[SII]	6716	21176.9±1.7	2.1532±0.0003	863±58	2.6±0.3
	[SII]	6731	21224.2±1.8	2.1532±0.0003	863±59	2.5±0.3
	[OI]	6300	19865.2±2.3	2.1532±0.0004	863±83	2.1±0.4
	[OI]	3727	11751.8±0.2	2.1532±0.0001	1042±11	2.5±0.3
	[OIII]	5007	17306.1±0.2	2.45638±0.00004	747±9	50.4± 1.1
MG 2308+0336	Hβ	4861	16802.8±1.5	2.45666±0.0003	747±66	6.1± 1.0
	Hα	6563	22684.0±0.3	2.45634±0.00006	747±13	22.7± 0.7
	[NII]	6583	22753.8±1.0	2.45645±0.0002	747±32	9.2± 0.7
	[SII]	6716	23213.5±2.4	2.45645±0.0004	747±79	6.0± 1.2
	[SII]	6731	23265.3±2.1	2.45645±0.0003	747±67	7.0± 1.2
	[OI]	6300	21775.6±2.2	2.45645±0.0004	747±79	4.0± 0.8
	[OIII]	5007	17306.1±0.2	2.45638±0.00004	747±9	50.4± 1.1
	[OIII]	5007	17306.1±0.2	2.45638±0.00004	747±9	50.4± 1.1